Lappeenranta
University of Technology

Emil Kurvinen

DESIGN AND SIMULATION OF HIGH-SPEED ROTATING ELECTRICAL MACHINERY

Thesis for the degree of Doctor of Science (Technology) to be presented with due permission for public examination and criticism in the Auditorium 1383 at Lappeenranta University of Technology, Lappeenranta, Finland on the 22nd of January, 2016, at noon.

Acta Universitatis
Lappeenrantaensis 687

Supervisors Professor Aki Mikkola
Department of Mechanical Engineering
Lappeenranta University of Technology
Finland

Professor Jussi Sopanen
Department of Mechanical Engineering
Lappeenranta University of Technology
Finland

Reviewers Associate Professor Kari Tammi
Department of Engineering Design and Production
Aalto University
Finland

Associate Professor Karuna Kalita
Department of Mechanical Engineering
Indian Institute of Technology Guwahati
India

Opponents D.Sc. (Tech.) Timo Holopainen
Motors and Generators
ABB Oy
Finland

Associate Professor Karuna Kalita
Department of Mechanical Engineering
Indian Institute of Technology Guwahati
India

ISBN 978-952-265-917-0
ISBN 978-952-265-918-7 (PDF)
ISSN-L 1456-4491
ISSN 1456-4491

Lappeenranta University of Technology
Yliopistopaino 2016

Abstract

Emil Kurvinen
Design and Simulation of High-Speed Rotating Electrical Machinery
Lappeenranta, 2016
68 pages

Acta Universitatis Lappeenrantaensis 687
Dissertation. Lappeenranta University of Technology

ISBN 978-952-265-917-0
ISBN 978-952-265-918-7 (PDF)
ISSN-L 1456-4491
ISSN 1456-4491

Global energy consumption has been increasing yearly and a big portion of it is used in rotating electrical machineries. It is clear that in these machines energy should be used efficiently. In this dissertation the aim is to improve the design process of high-speed electrical machines especially from the mechanical engineering perspective in order to achieve more reliable and efficient machines. The design process of high-speed machines is challenging due to high demands and several interactions between different engineering disciplines such as mechanical, electrical and energy engineering. A multidisciplinary design flow chart for a specific type of high-speed machine in which computer simulation is utilized is proposed. In addition to utilizing simulation parallel with the design process, two simulation studies are presented. The first is used to find the limits of two ball bearing models. The second is used to study the improvement of machine load capacity in a compressor application to exceed the limits of current machinery. The proposed flow chart and simulation studies show clearly that improvements in the high-speed machinery design process can be achieved. Engineers designing in high-speed machines can utilize the flow chart and simulation results as a guideline during the design phase to achieve more reliable and efficient machines that use energy efficiently in required different operation conditions.

Keywords: active magnetic bearing, design process, electrical machine, high-speed, modeling, rolling element bearing, simulation

Tiivistelmä

Emil Kurvinen
Suurnopeussähkökoneiden suunnittelu ja simulointi
Lappeenranta, 2016
68 sivua

Acta Universitatis Lappeenrantaensis 687
Väitöskirja. Lappeenrannan teknillinen yliopisto

ISBN 978-952-265-917-0
ISBN 978-952-265-918-7 (PDF)
ISSN-L 1456-4491
ISSN 1456-4491

Maailmanlaajuinen energiankulutus on kasvanut vuosittain ja iso osa energiasta käytetään pyörivissä sähkökoneissa. On selvä, että näissä laitteissa kulutettava energia on käytettävä mahdollisimman hyödyllisesti. Tämän väitöskirjatyön tavoitteena on parantaa suurnopeussähkökoneiden suunnitteluprosessia erityisesti koneenrakennuksen näkökulmasta, jotta saavutetaan kestäviä ja energiatehokkaita sähkökoneita. Suurnopeussähkökoneiden suunnitteluprosessi on haastavaa, koska useat vuorovaikutustekijät eri insinööritieteiden, kuten kone-, sähkö- ja energiatekniikan osa-alueilla vaikuttavat samanaikaisesti. Työssä esitetään monitieteinen suunnitteluprosessikaavio tietyntyyppiselle suurnopeussähkökoneelle, jossa hyödynnetään tietokonesimulaatiota. Lisäksi esitetään kaksi tutkimusta, jossa käytetään simulointia suunnitteluprosessin yhteydessä. Ensimmäinen näistä pyrkii selvittämään kahden kuulalaakerimallin soveltuvuusrajat. Toinen pyrkii parantamaan koneen kuormitettavuutta kompressorisovelluksessa, jotta nykyisten laitteiden käyttöaluetta voidaan laajentaa. Suurnopeussähkökoneiden suunnittelijat teollisuudessa voivat hyödyntää suunnitteluprosessikaaviota ja simulointituloksia jo varhaisessa suunnitteluvaiheessa. Näiden avulla saavutetaan luotettavampia ja energiatehokkaampia sähkökoneita, jotka käyttävät energiaa tehokkaasti eri käyttötiloissa.

Hakusanat: aktiivimagneettilaakeri, mallintaminen, simulointi, suunnitteluprosessi, suurnopeus, sähkökone, vierintälaakeri

Preface

The research work of this thesis was carried out during the years 2012–2015 in the laboratories of Machine Design and Machine Dynamics (since 2013) at Lappeenranta University of Technology and the academic year 2014–2015 in the Rotating Machinery and Controls Laboratory (ROMAC) at the University of Virginia, Virginia, Charlottesville, USA. The research was funded by several Tekes projects, Lappeenranta University of Technology and a Fulbright-Technology Industries of Finland Grant.

I would like to thank my supervisor Professor Aki Mikkola for providing me an opportunity to join the international research group and to pursue my doctoral degree. I respect your ways to motivate your students to aim for even higher standards, and your ways of promoting Finland, Lappeenranta University of Technology and our laboratory. I would also like to thank Professor Jussi Sopanen for his wide knowledge in the field of rotating machinery and the support and guidance towards this project.

The comments from the preliminary examiners Associate Professor Kari Tammi from Aalto University and Associate Professor Karuna Kalita from Indian Institute of Technology Guwahati are appreciated. The opponents of the public examination, D.Sc. (Tech.) Timo Holopainen from ABB Oy and Associate Professor Karuna Kalita from Indian Institute of Technology are also appreciated.

I want to thank Professor Houston Wood for hosting the visiting year in Virginia and express my gratuity to Professor Eric Maslen from James Madison University and Dr. Roger Fittro from the University of Virginia for the interesting research project they provided and their valuable supervising during the exchange period.

Thanks to all laboratory members of the laboratories of Machine Design and Machine Dynamics over the years for the valuable support and relaxing coffee breaks and sauna evenings. It has been truely an honor to be a part of both research groups. Also, I would like to thank the members of the Laboratory of Electrical Drives Technology and Fluid Dynamics for the valuable collaboration projects towards this dissertation.

The financial support of The Research Foundation of Lappeenranta University of Technology, Lauri ja Lahja Hotisen rahasto, Walter Ahlström Foundation, The American-Scandinavian Foundation (ASF) and the Fulbright Center is highly acknowledged.

Finally, I want to thank my lovely wife Tiia-Mari for loving and supporting me over the years. Also thanks to my parents, brothers and sister for all the life-lessons we have experienced and their constant support and love.

Lappeenranta, January 2016

Emil Kurvinen

1 Introduction **19**
1.1 Motivation for the study 19
1.2 Electrical machines 21
1.3 Objective and scope of the dissertation 24
1.4 Scientific contribution 24

2 Design, modeling and simulation of electrical machines **27**
2.1 Design process 28
2.2 Finite element method 31
2.3 Rotordynamics 34
2.4 Ball bearing modeling 39
2.5 Active magnetic bearings 43

3 Summary of the findings **47**
3.1 Bearing simulation 47
3.2 Design process 52
3.3 Compressor machine load capacity at low frequencies 55

4 Conclusions **59**
4.1 Suggestions for the future work 60

Bibliography **63**

Symbols

$a_{0...3}$	Polynomial coefficients
A	Cross section area
A_g	Air gap area
$\boldsymbol{a}$	Vector of polynomial coefficients
$\mathbf{A}$	Transformation matrix
B	Magnetic flux density
B_{x1}, B_{x2}	Magnetic flux density in the electromagnet poles
$\mathbf{B}$	Strain-displacement (second partial derivate of the shape function matrix $\mathbf{N}$)
$\mathbf{C}$	Damping matrix
d	Interpolating polynomial
d_i	Displacement at location i
d_j	Displacement at location j
d_θ	Slope of dependent variable
$\mathbf{D}$	Steady state matrix
E	Material Young's modulus
$F_{x,\mathrm{tot}}$	Total magnetic force in x-axis
F_{x1}	Magnetic force to positive x-axis
F_{x2}	Magnetic force to negative x-axis
$\boldsymbol{F}$	Time dependent force vector
g	Nominal air gap length
$\mathbf{G}$	Gyroscopic matrix
i	Nodal location or current (magnetic bearings)
i_b	Bias current
i_c	Control current
i_{x1}, i_{x2}	Currents for the electromagnet poles
I	Moment of inertia
$\mathbf{I}$	Identity matrix
j	Nodal location
k_i	Force-current coefficient (current stiffness)
k_x	Force-displacement coefficient (position stiffness)
$\mathbf{k}_e$	Element stiffness matrix
$\mathbf{K}$	Stiffness matrix
L	Length
$\mathbf{m}_e$	Element mass matrix
$\mathbf{M}$	Mass matrix
N	Number of turns

$\mathbf{N}$	Element shape function matrix
t	Time
u	Displacement in x-direction
$\boldsymbol{u}_i$	i^{th} mode shape
$\bar{\boldsymbol{u}}_i$	i^{th} mode shape (complex)
v	Displacement in z-direction
w_1	Force applied at impeller location
x	Displacement field or rotor position (magnetic bearings)
X	x-direction
$\boldsymbol{x}$	Vector of generalized coordinates
$\dot{\boldsymbol{x}}$	First time derivative of generalized coordinates
$\ddot{\boldsymbol{x}}$	Second time derivative of generalized coordinates
$\boldsymbol{X}$	Interpolating polynomials
$\boldsymbol{y}$	Generalized coordinates (1^{st} order ODE system)
$\bar{z}_{1\ldots4}$	Performance limits
$\boldsymbol{z}$	Eigenvector
$\bar{\boldsymbol{z}}$	Eigenvector (complex)

Greek letters

α_i	Real part of i^{th} eigenvalue
$\beta_i, \omega_{\text{d}i}$	Damped natural frequency
θ	Slope angle
θ_i	Slope angle at nodal location i
θ_j	Slope angle at nodal location j
θ_X	Rotation around x-axis
θ_Y	Rotation around y-axis
θ_Z	Rotation around z-axis
λ	Eigenvalue
λ_i	i^{th} eigenvalue
$\bar{\lambda}$	Eigenvalue (complex)
$\bar{\lambda}_i$	i^{th} eigenvalue (complex)
μ_0	Vacuum permeability
ξ_i	Damping ratio (i^{th} mode)
ρ	Material density
ϕ	Angle between magnet poles
$\omega_i, \omega_{\text{n}i}$	Natural frequency
Ω	Rotation speed
$\mathcal{H}_\infty$	$\mathcal{H}_\infty$ controller

Abbreviations

A/C	Air conditioning
AMB	Active magnetic bearing
BW	Backward whirling mode
CAD	Computer aided design
CE	Concurrent engineering
DFMA	Design for manufacture and assembly
DOF	Degrees of freedom
DW	Distributed windings
EOM	Equation of motion
EMDS	Electric motor-driven systems
FEM	Finite element method
FW	Forward whirling mode
HS	High-speed
HSIM	High-speed induction machine
HSPMSM	High-speed permanent magnet synchronous machine
IEA	International energy agency
MIMO	Multiple-input multiple-output
NdFeB	Neodymium-iron-boron (magnet)
PID	Proportional integral derivative
PM	Permanent magnet
PWM	Pulse width modulation
rpm	Revolutions per minute
SmCo	Samarium-cobalt (magnet)
TCW	Tooth-coil winding
VDI	Verein Deutscher Ingenieure

This dissertation consists of an introduction and the following publications.

Publication I

Kurvinen Emil, Sopanen Jussi, Mikkola Aki. (2015). Ball Bearing Model Performance on Various Sized Rotors with and without Centrifugal and Gyroscopic Forces. *Mechanism and Machine Theory*, Vol. 90, pp. 240–260.

Publication II

Kurvinen Emil, Sopanen Jussi, Mikkola Aki. (2014). Comparison of Ball Bearing Model Performance with and without Centrifugal and Gyroscopic Forces. International Mechanical Engineering Congress & Exposition (IMECE), November 14–20, Montreal, Canada.

Publication III

Uzhegov Nikita, Kurvinen Emil, Nerg Janne, Pyrhönen Juha, Sopanen Jussi, Sergei Shirinskii. (2015). Multidisciplinary Design Process of a 6-Slot 2-Pole High-Speed Permanent Magnet Synchronous Machine. *Transactions on Industrial Electronics*, Vol. 99, pp. 1–12, Accepted.

Publication IV

Uzhegov Nikita, Kurvinen Emil, Pyrhönen Juha. (2014). Design Limitations of 6-Slot 2-Pole High-Speed Permanent Magnet Synchronous Machines with Tooth-Coil Windings. European Conference on Power Electronics and Applications (EPE'14-ECCE Europe), August 26–28, Lappeenranta, Finland.

Publication V (submitted)

Kurvinen Emil, Fittro Roger, Maslen Eric. (2015). Improving Compressor Surge Performance with Advanced Controller. *Journal of Dynamic Systems, Measurement and Control*, submitted.

The articles were written under the supervision of Professors Aki Mikkola, Jussi Sopanen and Juha Pyrhönen from Lappeenranta University of Technology, Doctor Roger Fittro from the University of Virginia and Professor Eric Maslen from James Madison University. This dissertation has been written under the supervision of Professors Aki Mikkola and Jussi Sopanen.

Publication I

The author is responsible for implementing the models and writing the manuscript. The work was a joint effort with Professors Jussi Sopanen and Aki Mikkola. The authors have finalized the paper together.

Publication II

The author is responsible for implementing the models and writing the manuscript. The work is a joint effort with Professors Jussi Sopanen and Aki Mikkola. The authors have finalized the paper together. The author presented the research in the conference.

Publication III

Nikita Uzhegov is the principal author for this publication which was a joint effort by research team members under Professors Juha Pyrhönen and Jussi Sopanen. The author is responsible for the mechanical aspects of the design process including rotordynamics and including them in the design process. Nikita Uzhegov is responsible for the electrical aspects in the design process. Dr. Janne Nerg is responsible for the thermal aspects in the design process. The article was finalized together with all authors.

Publication IV

Nikita Uzhegov is the principal author for this publication. The author is responsible for the mechanical aspects of the limitations including rotordynamics

and structural analyses. Nikita Uzhegov is responsible for the electrical aspects in the design process.

Publication V (submitted)

The author is responsible for developing the simulation model that was a joint effort with Dr. Roger Fittro and Professor Eric Maslen. The idea for the manuscript came from Professor Eric Maslen. The work was done mainly during the visiting researcher period in the University of Virginia. The authors have finalized the paper together.

Results of additional publications that author contributed, but are out from the main scope of this dissertation were published in the following conferences [26, 32, 33] and journals [27, 31, 40].

Chapter 1

Introduction

Rotating electrical machines are used extensively in industrial applications and daily life around the world. The design, simulation and modeling of these machines are active topics of research for example in mechanical, electrical and energy engineering. In this thesis, the simulation and design of electrical machines is focused on from the *mechanical engineering* point of view. Currently it is possible to embed more simulation parallel with design process. Through linking simulation into the design process product development can be improved. In this thesis "rotating electrical machines" are referred to as "electrical machines" which includes electrical motors and generators. One of the common arguments towards all the work done to improve electrical machines relates to the smart usage of energy.

1.1 Motivation for the study

Electrical machines are widely used in day-to-day life and in industry. For example these machines can be found in an electric toothbrush, a fan, a car starter motor, a hybrid car's traction motor, an air conditioning (A/C) unit and the way up to the propulsion motors in a cargo vessel [38]. Commonly the size varies from milliwatts (mW) to megawatts (MW). Figure 1.1 shows a cutaway of a traction motor, that can be used for example to drive a car. In the figure the rotating part is referred as the rotor and stationary part as the stator.

To understand the full extent of the usage of electrical machines, according to the international energy agency (IEA) 43–46% of globally produced electricity is consumed by electric motor-driven systems (EMDS) such as compressors, fans or pumps, where the majority of the electricity is used by the electric motor itself.

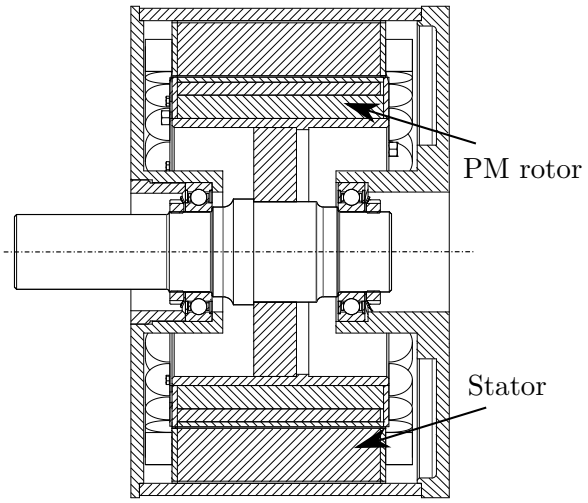

Figure 1.1. Cross section of an electric machine.

[55] On the otherhand, almost all global electrical generation is based on electric generators. [56]

Due to the high global electricity consumption in systems that are driven by electric motors, efficiency and reliability of each new electrical machine are the key aspects that are focused on during the design process. Efficiency is a measure that tells how well energy is transformed from electricity to mechanical energy, *i.e.*, how much energy is transformed to other forms such as heat or noise, which usually occur as well. Reliability is a measure that considers the required maintenance and life cycle of the electrical machine.

Developing new electrical machines is a challenging task for engineers. It has multidisciplinary interactions in the energy conversion phenomena which requires deep understanding of the system, including electrical and magnetic fields, as well the heat produced [40] by the energy conversion and the mechanical rigidity of the system [31]. In addition, the application and environment where the electrical machine is driven requires detailed understanding as even a small detail can make a huge change to the final design. For example, information about the nominal speed of an electrical machine where it is mostly operated is a valuable information. Having the information of approximated nominal speed in the beginning of the design process allows an electrical machine to be optimized to work according to best efficiency at that speed.

Modern electrical machine design commonly requires participants from several engineering fields in order to achieve a highly efficient and reliable electrical machine. Usually engineers from the electrical, mechanical, thermal, energy and

control engineering fields are involved.

As the design of electrical machines requires experts from several fields, it is challenging to have a common understanding of each member's tasks and inputs and outputs - or even a common technical language. Achieving good, high performance electrical machine design requires compromises from all the engineering fields. This means for example that designing a too massive of an electrical machine from a mechanical point of view leads to low performance from the electrical and thermal engineering points of view.

General design approaches are introduced in the literature and these give a good starting point for a design task. One of them is the systematic design process, where direct tasks for a responsible person can be set. In addition, certain simulation tools are available and can be used to benchmark the results before building the first prototype. For example, in a high-speed electrical machine the rotor dynamical performance have to be understood to avoid excessive vibrations in the prototype, which in the end enables a design that leads to a working electrical machine.

To build a simulation model the behavior of a physial system has to be understood in order to justify a simulation approach which predicts the behavior accurately and computationally efficiently. The results of simulation are only as good as the simulation model and if the simulation model is too far from the physical machine, the results do not predict the physical system well. However, a well built simulation model predicts the physical system accurately and that enables the designing of more reliable and safe electrical machines. This can be achieved for example by simulating the machine at over-speed or at faulty conditions. An example of this is the studies on active magnetic bearing (AMB) supported rotor touchdown bearing performance in a magnetic bearing failure situation [8, 44].

In the end, if an electrical machine is poorly designed or used inefficiently it can use excessive amounts of energy and that further requires globally the production of even more energy, which requires the building of new power plants to keep up with the electric power demand. This gives clear motivation to develop new improved electrical machines and systems that are driven by them.

1.2 Electrical machines

Almost 200 years ago it was discovered by a Dr. Øersted that the electric currents create magnetic fields. Around the same time the solenoid was invented by Andrè-Marie Ampère and in the 1821 Michael Faraday build the first type of device that was rotated by an electromagnetic field and this started the era of the electric motors. [13]

One of the most commonly used electrical machine types in the last century and still today are induction machines. Usually in induction machines power is transferred from the stationary part to the rotating part through electromagnetic induction. The early version of these rotated at constant speed, using a fraction of the electric frequency that was delivered to the end users. For example in a 50 Hz network a 4-pole induction motor shaft would rotate up to 1500 rpm. However, in practice there is a small difference (*i.e.* slip) in the actual speed of the rotor and synchronous speed that leads the rotor rotate slightly slower. Due to the slip, the actual torque is created in the induction machines.

As the electrical machines developed from the early versions, also power electronics that allow, for example, to control electrical machines were developed. In the 1960s variable speed drive motors with pulse width modulation (PWM) become available and that allowed adjusting the motor rotation speed. [48] This was possible by having an inverter between the electric motor and the network it was connected to.

The use of an inverter enables high-speed electrical machines which allow the rotor to rotate really high speeds, usually from 10000 to 200000 rpm. High speeds allow to design machines that are directly connected to the application or working tool without having a gearbox that in conventional machines increases the rotation speed. For example in a compressor application the impeller can be directly attached to the main rotor in a high speed electrical machine.

In the last century the development of permanent magnets (PM) was rapid and more powerful magnets were introduced. Since 1960s the development of rare-earth magnets started a new era due the discovery and mass production development of samarium-cobalt (SmCo) and neodymium-iron-boron (NdFeB) magnets, which are still the strongest types of the permanent magnets available. [39]

In electrical machines permanent magnets the enabled magnetization of the rotor without having brushes that created an electromagnetic path from the stationary part to the rotating part. Challenges and limiting factors in the utilization of PMs are that they are expensive, that pure materials are fragile, and that high temperatures together with certain magnetic fields will cause a PM to lose its magnetic properties.

As PMs were developed their use in electrical machines was increased. Nowadays PM machines are used in high-end applications such as traction motors in hybrid cars, elevators and wind generators. PM machines are usually applied where high power per volume, and high power to mass ratio together with high efficiency are required. [16]

Modern electrical machines consist of several different subsystems such as a mechanical rotor and stator, bearings, cooling, and control systems. These

subsystems are in close interaction with each other. The bearings are mounted on the rotor producing the support for the rotor. The rotor can be seen as a mechanical system that transfers torque. Electronics together with the control software defines the way the rotor system behaves. In order to control the dynamic responses of a rotating machine, the bearings, rotor and control system must be integrated already in the design phase.

In mechanical engineering, the support for the rotating part is one research field. Additionally, several other study fields in the mechanical engineering involve electrical machine design such as tribology, structural and rotordynamics analyses as well as modeling and simulation.

Tribology concentrates on the interaction between surfaces in a relative motion, which occur for example in bearings. Conventionally electrical machines use rolling element bearings to support the rotor. However, depending on the rotor size and rotation speed the conventional rolling element bearing solution might not be suitable at high rotating speeds and usually there is a need for journal bearings or AMBs. Journal bearings usually rely on a thin layer of liquid or gas to support the rotor. AMBs use magnetic force to levitate the rotor and the magnetic force is actively controlled by sensor information monitoring the rotor position. The sensor information is fed to the controller that sends a signal to the power amplifier that produces a current in electromagnets that keep the rotor in the desired position.

Structural analysis focuses on the physical limits that arise from the elasticity of the materials that are used in the electric machine. The materials used in the machine should not experience stresses that exceed the material's allowed strength. Especially, in the rotating part, where there might be connections between parts, such as laminations or a magnet, that are usually placed to the rotor by heating for example lamination which at room temperature will not fit top of the rotor. The heated lamination can be placed top of the rotor and stays connected due friction as it cools down and shrinks to the rotor and hold the in place.

In simulations the aim is to design an accurate model of an actual physical system in a computer. A simulation model can be used to study different scenarios or to try out various configurations. Simulation models do not have any limitations for example on the speed that they are operated and that enables to test an over speed situation. By creating simulation models the required number of physical prototypes can be reduced due to the fact that the manufactured prototypes are already more mature.

Responsibilities in the design process can be divided for example in a way that the electrical engineers are mainly responsible for the power and torque production and the thermal engineers for the feasible cooling solution. In this thesis design methodology and simulation methods are applied and developed in order to

approach the design process in a straightforward manner and to use sufficient simulation methods to predict the dynamical behavior of the system and to find performance related information on electrical machines during the design process.

1.3 Objective and scope of the dissertation

Due to the multidisciplinary application, the scope of this dissertation is to consider the electrical machine design process and simulation tools from a mechanical engineering perspective. However, the research work is done mostly in a multidisciplinary research team.

Due to the complexity of the problem, this thesis focuses mainly on the development of the electrical machine design process and simulation procedures that give accurate estimates, which in the end yields better electrical machine design. To achieve these specific goals, the design process requires the building of sufficient simulation models to benchmark performance measurements, which are for example rotor dynamical performance, bearing stiffness variation in different speeds and a specific load capacity.

The primary objective of this dissertation is to achieve better electrical machine designs. This can be achieved by utilizing simulation more closely parallel with the design process of electrical machines. In general, simulation can be used to find the limits, and in this work the aim is to utilize two different ball bearing models and determine the limits for these two different complexity models. Simulation can also be used to exceed the limits, and in this work a specific application performance was studied and improved significantly.

In addition, the design process for a high-speed electrical machine is proposed. High-speed machines are usually the most challenging to design due the interactions between several engineer fields. In high speeds several factors that affect electrical machine performance are amplified.

The hypotheses are that the standard tools that are used in electrical machine design and in the absence of simulation parallel to the design process prevent the development of better rotating electrical machines. Simulation tools enable *finding limits*, which is shown by an example of two ball bearing models used to find the limits for the simulation models, and second, *exceeding limits*, by an example of an AMB supported compressor to maximize the load capacity in the impeller location through a different control algorithm.

1.4 Scientific contribution

During the research related to this dissertation several electrical machines were developed as a part of the research and those led finally to the development of the

design process flow chart and the creating and applying of simulation models. The design process of an electrical machine involves many parameters that should be taken into consideration. Some of the variables would require a physical prototype to be build. For example, load rejection maximization at the impeller location in a compressor application. Building a simulation model parallel to the design process enables the study of performance parameters before the actual prototype is build. This saves time and energy both in the design and in the manufacturing process and most importantly enables designing a good electrical machine. A simulation based design process requires understanding of the physics of the designed system and creating an accurate enough mathematical prediction of the system. This model is used to find the boundaries and the best behaving design for the prototype of the developed machine. The examples of simulation tools to predict dynamical behavior are presented in *publications I, II* and *V*.

The main scientific contributions of this dissertation can be summarized by three main categories as:

First, this dissertation introduces a multidisciplinary systematic design process based on computer simulation for a 6-slot 2-pole high-speed electrical machine. The design process enables engineers to follow a direct procedure to develop of a high speed machine with the help of computer simulation.

Second, part of the design process is the analysis of bearings. In this study, guidelines for the appropriate selection of a suitable bearing model for three case studies are presented. Two different complexity ball bearing models were implemented. One considers high-speed forces, and the other neglects them. Both models were used to study three structures, and the simulation results were compared. The bearing behavior is studied at different shaft rotation speeds and the simulation results are used to determine when the model containing the centrifugal and gyroscopic forces should be used.

Third, simulations introduced in this study enable to push the limits of current designs and an example to improve AMB compressors by developing a simulation model of the machine and to find its limits. This study shows that extensively utilization of simulation can lead to a significant improvement in a specific application, which in this case is shown by defining machine load capacity in a compressor application.

The three main subjects in this dissertation further improve the design process of electrical machines and shows that the utilization of simulation parallel with the design process yields better results. By understanding the limits of simulation models and capabilities, further improved electrical machines can be designed.

Chapter 2

Design, modeling and simulation of electrical machines

This chapter gives a short introduction to the methods that are used in the publications. The work done in this dissertation is based mostly on research projects made in collaboration with a multidisciplinary team of researchers.

In motor applications the rotating electric machines converts electricity into mechanical energy and in a generator applications mechanical energy to electrical energy. Energy conversion is based on the principle that a current-carrying conductor is wound to coil shape, which creates a magnetic field. Placing these coils in a circular form and changing the current at certain frequency forces the rotating part of the motor to rotate. However, even if the principle is fairly straightforward detailed understanding of the energy conversion phenomena from a multidisciplinary perspective is required in order to design and simulate high efficiency machines. In the energy conversion part the energy converts to heat for example due the resistance in the materials. These are called losses which should be minimized.

The five most relevant topics of this dissertation are briefly introduced from a mechanical engineering aspect to give an overview of the topic which gives relevant background information to the research done. The first section describes the design process of a high-speed electric machine. The general design methodology is briefly explained and design approaches for high-speed electric machines that are available from literature are introduced. This section gives an overview of the design aspects that have to be considered in the rotating electric machine application.

The next section explains the finite element method (FEM) that is used to formulate a mathematical model of a physical system. FEM is a general method

that is applied widely in various engineering fields. This section gives an overview on how physical systems are converted to equivalent mathematical models and analyzed in computers.

The third section is rotordynamics, which is a branch of engineering that studies rotating machinery vibrations. In this section it is explained based on the FEM approach. Additionally the approach to predict the dynamical behavior of rotating structures is described. This section also gives an overview of a specific application of FEM and its principles.

The final two sections relate to rotordynamics and describe the support modeling that holds the rotating part in place. These support models are included in the rotordynamics model to predict the supported rotating structure accurately. Commonly used ones in the industry are rolling element bearings, journal bearings and AMBs. In section four, one type of rolling element bearing, ball bearing and its modeling are described. In the fifth section an AMB is presented. AMBs are usually used in highly demanding applications, where for example the rotation speed is very high or oil-free operation is required.

2.1 Design process

General design methods that are applied to various engineering fields are available in the literature. Commonly used ones are systematic design [37], concurrent engineering (CE) [45], collaborative design [35] and reverse engineering [34]. In this work the design process is based on the systematic design approach, which goes step by step from the requirements of the designed product to a ready to be manufactured product.

Figure 2.1 shows a flow chart of the systematic design process presented in Verein Deutscher Ingenieure (VDI) 2222 [43]. The systematic design approach can be divided into four main categories that are the clarification of the task, conceptual design, embodiment design and detail design. In the clarification of the task phase requirements and wishes are collected. During the second phase, conceptual design, a basic structure is defined according to the requirements. In the third, embodiment design, the conceptual design is analyzed in more detail. The last step is detail design, where a design that fulfills all the requirements is prepared to be manufactured. Each step is iterative and requires the successful finishing of the previous step before proceeding to the next step.

The design process of an electrical machine is a complex task which requires at least the understanding of electromagnetics, mechanics, thermal and material science, rotordynamics, electronics and control. The design process of an electrical machine can be divided into two approaches; component design and system design. Component design is the traditional approach, where each component is designed

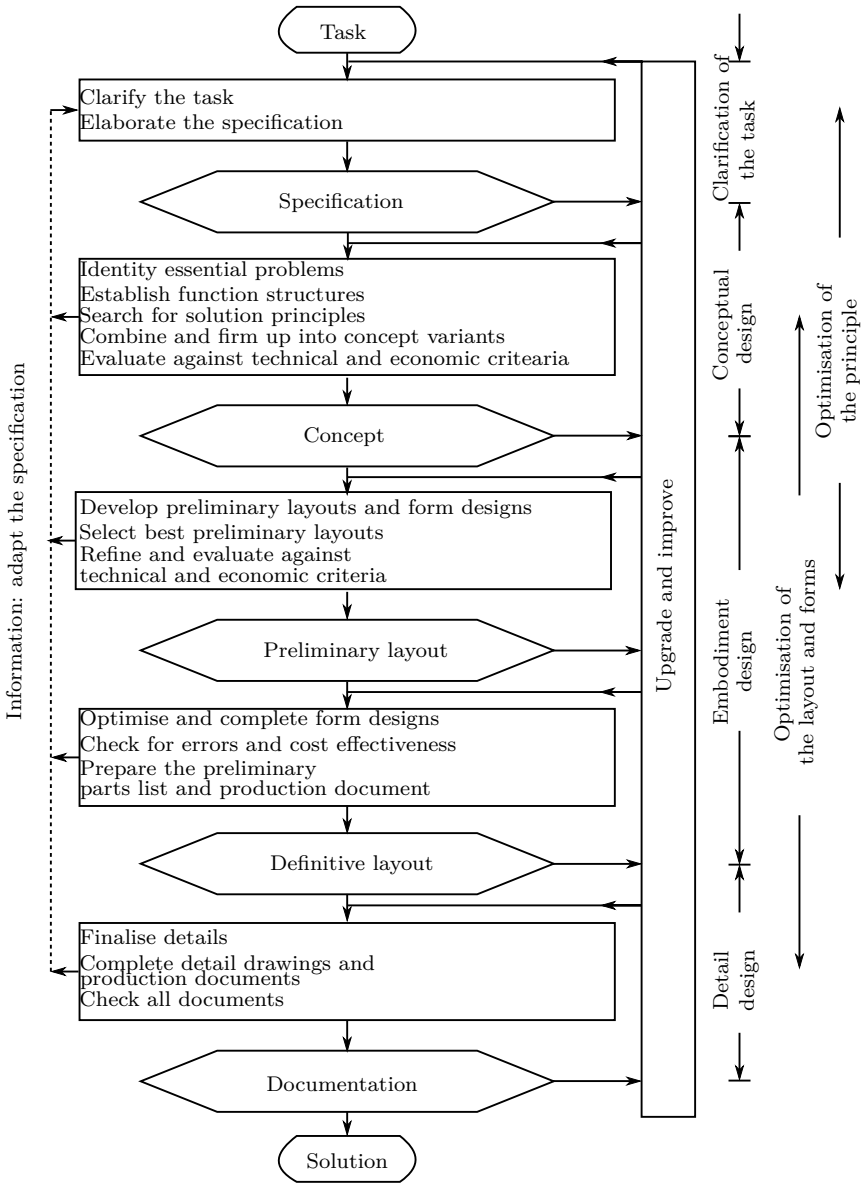

Figure 2.1. VDI 2222 systematic design flow chart [43].

separately. The components can be, for example, the rotor, stator or cooling system. These components are then assembled together to form a full system, which in this case is an electrical machine. The second approach, system design, consider the overall system performance. In this approach each component interaction is taken into account and the requirements for the machine are considered. [50] This approach has more iterations between different components,

however, it can lead to a machine with better performance.

In the beginning of the design process the requirements are defined. These requirements are the basis for the design process. These define for example performance such as power, torque and efficiency. In addition, the design requirements usually consider the machine's operating environment. For example, what is the temperature or how much vibration is present? Also the electrical machine type such as induction machine, or permanent magnet machine is usually defined. In the beginning of the design, especially without prior knowledge, a comprehensive list of requirements can be challenging to set, but is necessary, in order to have clear targets for the design. A questionnaire can be used in the beginning to set the requirements [27].

A trend to develop higher speed machines that enable in many applications direct driven systems, meaning that the application, *e.g.*, compressor impeller, can be directly attached to the main rotor without a gearbox, are increasing. The definition for high-speed (HS) machines is not fully fixed, but in general, they are categorized by the peripheral speed or a number that is produced from rotation speed and power. For the first definition, by peripheral speed, Jokinen and Luomi [23] define over 150 m/s and Binder and Schneider [7] from 100 m/s to 250 m/s as the demarcation of HS machines. The second definition, a machine is high-speed if it rotates in excess of 10 000 rpm and if its rpm multiplied by the square root of the rated power ($\text{rpm}\cdot\sqrt{kW}$) is over 100 000. [53] The highest achieved peripheral speeds for modern machines is 400 m/s for a solid rotor induction machine [15].

HS machines are commonly variable speed driven machines, where the load can be changed according to the demand of the application. The design process of a HS machine is challenging due to the interactions of different disciplines. To name three for example, the first is that high power density demands powerful cooling. Second, each of the disciplines are on the limits when attempting to achieve a high performing machine. Third, the tolerances between the rotating and non-rotating parts are tight. In HS machines it is not generally possible to use a standard off-the-shelf structure and each machine needs to be designed according to the specific requirements of the application.

Due the complex and highly iterative design process, several authors have published scientific articles regarding to the design process of high-speed electrical machines. Arkkio *et al.* [3] described a design for high-speed induction machines (HSIM) and high-speed permanent magnet synchronous machines (HSPMSM) viewed from electrical and thermal aspects. More extensively design methodology was implemented in [25] to define the maximum power and speed limits for a HSPMSM. Ranft [41] proposed a design methodology chart for a HSIM with electromagnetic and mechanical aspects. Cheng *et al.* [11] proposed a design flow chart for a HSPMSM with a full cylindrical magnet in the rotor. However, the flow chart

included only electrical and mechanical design, and the thermal analysis was done separately.

Bernard *et al.* [6] proposed a design flow and analytical optimization for a PMSM with a gearbox. The design flow was for a screwdriver application with infinite stiff supports, which limits its implementation for HS machinery. Although several design methodologies are presented in the literature, none of them propose a comprehensive multidisciplinary design process for 6-slot 2-pole HS applications that includes electrical, mechanical and thermal analyses.

In *publication III* a multidisciplinary design process for a 6-slot 2-pole high-speed electrical machine is proposed. One important aspect from mechanical engineering point of view is the modeling of these electrical machines and analyzing their dynamical behavior on different rotation speeds. The aim is that the rotating part operates without any excessive vibrations over the specified operation speed range. In the following section the fundamentals of the modeling part are introduced.

2.2 Finite element method

The finite element method is a widely used method in engineering that is used to solve physical problems. In FEM a physical system is simplified into a mathematical model. FEM is applied for example to fluid dynamics, electromagnetics and in mechanical engineering generally speaking to structural and dynamical analyses. FEM is a numerical method for solving differential equations. The solutions obtained by FEM are approximates due the numerical methods and a physical system is discretized into a finite number of elements. [12] The utilization of computer-aided design (CAD) has further increased of the utilization of FEM due the fact that a designed model can be directly utilized to create finite element mesh. [5]

Elements in FEM consist of nodes. Number of nodes and element type define the element's degrees of freedom (DOF) and are used to describe its kinematics. Nodes also define the element's geometry, *e.g.*, a two geometric node element is called a beam element. A FEM model consist from a continuous mesh of elements that are connected through nodes. [12]

Physical properties, such as material properties have to be defined in order to analyze a specific problem, and also the boundary conditions for each element has to be set. These boundary conditions define how the nodes of elements can move in respect to others. [12]

In the literature several types of elements can be found from a point mass to multi-degree-of-freedom solid elements. Depending on the problem analyzed these element types are chosen accordingly. Figure 2.2 depicts a four DOF beam element. [42]

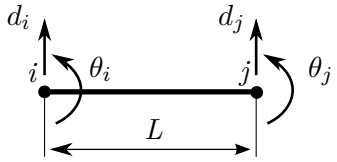

Figure 2.2. A four degrees of freedom beam element.

In mechanical engineering, FEM is used to solve for example stresses and strains in desired locations, in electrical engineering for electrical and magnetic fluxes and in thermal engineering for heat flux. For simple geometries analytical equations can be used to solve problems but usually the geometries are over simplified. However, in some applications such as beam structures these can be applied. FEM is not limited by the geometry of the studied problem. However, complex geometries often require more elements to solve the problem accurately and thus also often require more computational effort.

To build a FEM model it is required to set the problem and define the model properly in order to have a model that represents a physical system accurately. In some cases, where for example the loads or constrains are not known, this might lead unrealistic results. Due to this, usually the building of a FEM model is started from simple geometry where analytical equations can be used to verify that the created FEM model is set properly, *e.g.*, that the constrains that limit the elements' movements are set correctly.

Kinematics of elements are described through shape functions that describe single element behavior. By adding the separate elements together a set of equations can be solved simultaneously. For example, displacements can be solved at any location in the model. [12]

Formulating the shape functions for a four degrees of freedom beam element can be done as in [12], where a cubic polynomial with four parameters describes the deflection of the beam. It should be noted that also other interpolation methods can be used as well. In terms of polynomial coefficients $a_{0\ldots3}$ and displacement field x an interpolating polynomial, d, where rotations are assumed to be small ($d_\theta \approx \theta$) can be written in the form

$$d = a_0 + a_1 x + a_2 x^2 + a_3 x^3 \quad \text{or} \quad d = \boldsymbol{X}\boldsymbol{a}, \tag{2.1}$$

where interpolating polynomial vector $\boldsymbol{X} = [1 \;\; x \;\; x^2 \;\; x^3]$ and vector of polynomial coefficients $\boldsymbol{a} = [a_0 \;\; a_1 \;\; a_2 \;\; a_3]^T$. Noting that the displacements (d_i and d_j) and slopes (θ_i and θ_j) in the both end of the beam as

$$\begin{aligned} d &= d_i \;\text{ and }\; d_\theta = \theta_i \;\text{ at } x = 0, \\ d &= d_j \;\text{ and }\; d_\theta = \theta_j \;\text{ at } x = L, \end{aligned} \tag{2.2}$$

where L is the length of the beam. The equation 2.1 can then be written as

$$\underbrace{\begin{bmatrix} d_i \\ \theta_i \\ d_j \\ \theta_j \end{bmatrix}}_{\boldsymbol{x}} = \underbrace{\begin{bmatrix} 1 & 0 & 0 & 0 \\ 0 & 1 & 0 & 0 \\ 1 & L & L^2 & L^3 \\ 0 & 1 & 2L & 3L^2 \end{bmatrix}}_{\mathbf{A}} \underbrace{\begin{bmatrix} a_0 \\ a_1 \\ a_2 \\ a_3 \end{bmatrix}}_{\boldsymbol{a}} \quad \text{or} \quad \boldsymbol{x} = \mathbf{A}\boldsymbol{a}, \tag{2.3}$$

where $\mathbf{A}$ is a transformation matrix and $\boldsymbol{x}$ is vector of generalized coordinates. The polynomial coeffiecients can be solved as $\boldsymbol{a} = \mathbf{A}^{-1}\boldsymbol{x}$ and Equation 2.1 can be written as

$$d = \mathbf{N}\boldsymbol{x}, \text{ where } \mathbf{N} = \boldsymbol{X}\mathbf{A}^{-1} = \begin{bmatrix} 1 & x & x^2 & x^3 \end{bmatrix} \begin{bmatrix} 1 & 0 & 0 & 0 \\ 0 & 1 & 0 & 0 \\ -\frac{3}{L^2} & -\frac{2}{L} & \frac{3}{L^2} & -\frac{1}{L} \\ \frac{2}{L^3} & \frac{1}{L^2} & -\frac{2}{L^3} & \frac{1}{L^2} \end{bmatrix}, \tag{2.4}$$

where $\mathbf{N}$ is a shape function matrix. For the four degrees of freedom beam element it yields

$$\mathbf{N} = \begin{bmatrix} 1 - \frac{3x^2}{L^2} + \frac{2x^3}{L^3} & x - \frac{2x^2}{L} + \frac{x^3}{L^2} & \frac{3x^2}{L^2} - \frac{2x^3}{L^3} & -\frac{x^2}{L} + \frac{x^3}{L^2} \end{bmatrix}, \tag{2.5}$$

which can be used to obtain a mass matrix for the beam element as

$$\mathbf{m}_e = \rho A \int_0^L \mathbf{N}^T \mathbf{N} \mathrm{d}x, \tag{2.6}$$

where ρ is the material density and A is the cross-section area. Stiffness matrix as

$$\mathbf{k}_e = EI \int_0^L \mathbf{B}^T \mathbf{B} \mathrm{d}x, \tag{2.7}$$

where E is the material's Young's modulus, I moment of inertia of cross sectional area and $\mathbf{B}$ is a strain-displacement matrix that is the second derivative of shape function, $\mathbf{N}$, ($\mathbf{B} = \frac{\mathrm{d}^2}{\mathrm{d}x^2}\mathbf{N}$).

FEM enables to discretize a physical system into a mathematical model and predict its behavior under various conditions. These mathematical models can be used in the design process to analyze the different components in required environments. FEM has been applied in many engineering fields and in these fields to specific applications. In this dissertation FEM is applied to rotordynamics. Rotordynamics is a research field that studies the dynamical behavior of rotating machinery. Rotordynamics is explained in the next section in more detail.

2.3 Rotordynamics

Rotordynamics is a branch in mechanical systems that focuses on the behavior of rotating structures. Depending on the details of rotor models, they can be described as two general types, rigid and flexible. [14]

In rigid rotordynamics, analytical solutions are available and behavior can be calculated accurately for simplified geometries. However, the rigid assumption, where shaft deformation is neglected, over simplifies in many cases the problem, and as a consequence model prediction and actual behavior differs. On the other hand, flexible rotordynamics often requires numerical calculation methods such as FEM. To build a FEM model usually requires more variables compared to analytical calculations, which leads to the solution is being more complex compared to analytical solutions. However, it more accurately predicts a physical system behavior. [10]

In many applications such as compressors, and pumps the higher rotation velocity leads to high power density and that enables a smaller machine to compress or pump more. In many new applications the requirement to work above the first critical speed creates challenges to the design process and due to that a systematic design methodology is required to find a solution that is feasible from a multidisciplinary perspective.

In rotordynamics 3D beam elements are commonly used to predict rotor behavior. Euler-Bernoulli and Timoshenko beam elements are commonly used in commercial software. Example of an isotropic three dimensional beam element is shown in Figure 2.3, where element have 12 degrees of freedom defined by two nodes i and j and their translations (u, d, v) and rotations $(\theta_X, \theta_Y, \theta_Z)$. In addition mass elements can be used to model disks or bearing housings. [10] These elements are implemented to commercial software's, and in this work to a Matlab based rotordynamics program RoBeDyn.

Rotor-bearing system behavior can be described for rigid and flexible rotors with the equation of motion (EOM) as

$$\mathbf{M}\ddot{\boldsymbol{x}}(t) + (\mathbf{C} + \Omega\mathbf{G})\dot{\boldsymbol{x}}(t) + \mathbf{K}\boldsymbol{x}(t) = \boldsymbol{F}(t), \tag{2.8}$$

where $\mathbf{M}$ is the mass matrix, $\boldsymbol{x}$ is the vector of generalized coordinates (displacement), and $\dot{\boldsymbol{x}}$ and $\ddot{\boldsymbol{x}}$ are the first and second time derivatives of the generalized coordinates (velocity and acceleration). $\mathbf{C}$ is the damping matrix, Ω is rotation speed and $\mathbf{G}$ is the gyroscopic matrix and $\mathbf{K}$ is the stiffness matrix and $\boldsymbol{F}(t)$ is the time dependent force vector.

Eigenvalues can be solved to determine the natural frequencies of a rotor-bearing system first by setting the external force, $\boldsymbol{F}(t)$, to zero in Equation 2.8.

$$\mathbf{M}\ddot{\boldsymbol{x}}(t) + (\mathbf{C} + \Omega\mathbf{G})\dot{\boldsymbol{x}}(t) + \mathbf{K}\boldsymbol{x}(t) = 0. \tag{2.9}$$

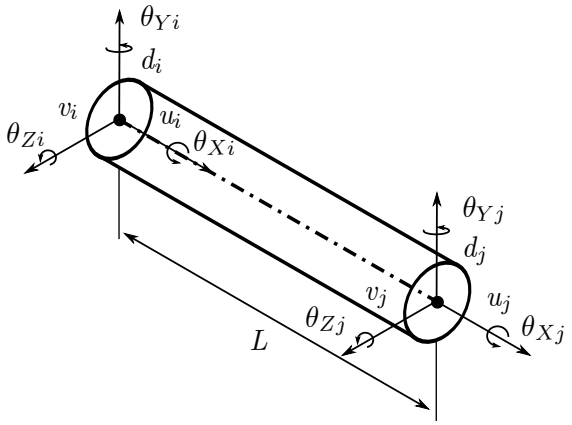

Figure 2.3. A Two-node, three dimensional isotropic beam element with 12 degrees of freedom.

Then multiplying the equation 2.9 by $\mathbf{M}^{-1}$ it becomes

$$\ddot{\boldsymbol{x}}(t) + \mathbf{M}^{-1}(\mathbf{C} + \Omega\mathbf{G})\dot{\boldsymbol{x}}(t) + \mathbf{M}^{-1}\mathbf{K}\boldsymbol{x}(t) = 0. \tag{2.10}$$

Converting the second order differential equation into first order system by denoting $\boldsymbol{y}_1 = \boldsymbol{x}$ and $\boldsymbol{y}_2 = \dot{\boldsymbol{x}}$

$$\begin{aligned} \dot{\boldsymbol{y}}_1 &= \dot{\boldsymbol{x}} = \boldsymbol{y}_2, \\ \dot{\boldsymbol{y}}_2 &= \ddot{\boldsymbol{x}} = -\mathbf{M}^{-1}(\mathbf{C} + \Omega\mathbf{G})\dot{\boldsymbol{x}}(t) - \mathbf{M}^{-1}\mathbf{K}\boldsymbol{x}(t) \end{aligned} \tag{2.11}$$

that can be written in matrix form as

$$\dot{\boldsymbol{y}} = \begin{bmatrix} \dot{\boldsymbol{y}}_1 \\ \dot{\boldsymbol{y}}_2 \end{bmatrix} = \begin{bmatrix} 0 & \mathbf{I} \\ -\mathbf{M}^{-1}\mathbf{K} & -\mathbf{M}^{-1}(\mathbf{C} + \Omega\mathbf{G}) \end{bmatrix} \begin{bmatrix} \boldsymbol{y}_1 \\ \boldsymbol{y}_2 \end{bmatrix} = \mathbf{D}\boldsymbol{y}, \tag{2.12}$$

where $\mathbf{I}$ is identity matrix and $\mathbf{D}$ is steady state matrix. Solution for the steady state matrix is assumed to be in the form $\boldsymbol{y} = \boldsymbol{z}e^{\lambda t}$ and then the generalized eigenvalue problem can be solved

$$\mathbf{D}\boldsymbol{z} = \lambda\boldsymbol{z}. \tag{2.13}$$

Eigenvalues are in complex conjugate pairs form for ith mode as

$$\lambda_i = \alpha_i \pm j\beta_i, \tag{2.14}$$

where α_i is the real part of the eigenvalue and can be expressed as $\alpha_i = \omega_{\mathrm{n}i}\xi_i$, where ξ_i is the damping ratio and $\omega_{\mathrm{n}i}$ is the natural frequency. β_i is the damped

natural frequency ($\omega_{\mathrm{d}i}$) that can be also expressed as $\beta_i = \omega_{\mathrm{d}i} = \omega_{\mathrm{n}i}\sqrt{1-\xi_i^2}$. Natural frequencies for ith mode can be calculated as

$$\omega_{\mathrm{n}i} = \sqrt{\alpha_i^2 + \beta_i^2}, \tag{2.15}$$

and the damping ratio of mode i can be calculated by

$$\xi_i = \frac{-\alpha_i}{\sqrt{\alpha_i^2 + \beta_i^2}}. \tag{2.16}$$

Eigenvectors ($\boldsymbol{z}_i$) for each eigenvalue can be solved by substituting $\lambda_i = \omega_{\mathrm{n}i}^2$ in Equation 2.13. If the eigenvalues are complex, then they occur in a pair of complex conjugates. Eigenvectors are in the form of

$$\boldsymbol{z}_i = \begin{bmatrix} \boldsymbol{u}_i \\ \lambda \boldsymbol{u}_i \end{bmatrix} \quad \bar{\boldsymbol{z}}_i = \begin{bmatrix} \bar{\boldsymbol{u}}_i \\ \bar{\lambda}\bar{\boldsymbol{u}}_i \end{bmatrix}. \tag{2.17}$$

In rotordynamics the eigenvectors corresponds to mode shapes ($\boldsymbol{u}_i$). Mode shapes define the whirling shape and shows the relative magnitude and phase of motion.

Rotor natural frequencies and mode shapes (free-free), where the bearing and support or any other additional parts than rotor description is removed from the system matrix at zero rotation speed ($\Omega = 0$). Equations 2.8-2.17 can be used to solve natural frequencies and mode shapes. Calculated rotor natural frequencies and mode shapes can also be validate experimentally by modal analysis. Figure 2.4 shows the six first mode shapes on a plane, where the two first are rigid body modes and following ones flexible modes of a rotor and their natural frequencies. A third rigid body mode exists also in axial direction, however usually the movement in the axial direction is constrained.

For an N-degrees of freedom (NDOF) system the N-number natural frequencies and mode shapes can be calculated. However, usually the lowest flexible mode shapes contain the most strain energy and are accurate enough. Thus, those are usually considered to be the most important.

A Campbell diagram (frequency interference diagram) includes the natural frequencies and excitation frequencies (rotation speed) in the same figure. In the Campbell diagram the support stiffness is included in the rotor model. In this figure the critical speeds where resonance can occur in the supported rotor is shown. Example of a Campbell diagram is shown in Figure 2.5 where a rotor is supported via two symmetrical AMBs.

In the figure, the dashed line (A) is rotation speed and the four first critical frequencies are shown. Where the dashed line crosses the solid lines are intersection points where resonance occurs. These rotation speeds should be avoided. The first

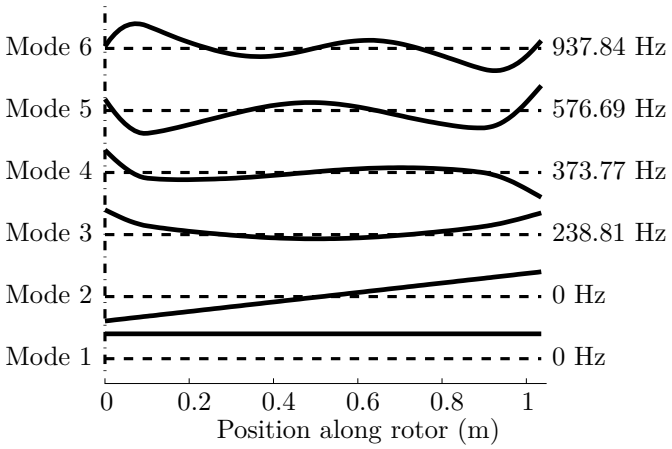

Figure 2.4. Free-free mode shapes and natural frequencies of the rotor.

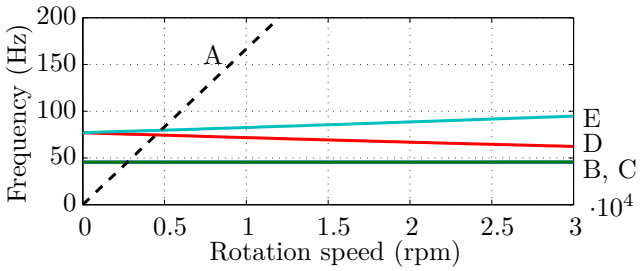

Figure 2.5. Campbell diagram of a rotor.

and second critical frequencies are at 45.54 Hz (B,C). The third and fourth (D,E) frequencies are at 76.94 Hz at zero rotation speed. The gyroscopic effect ($\Omega\mathbf{G}$) and cross-coupling terms of bearings and supports causes the frequencies (D,E) to separate as rotation speed increases. Usually, the frequency that is increasing over the rotation speed, in this case line E, is referred as the forward whirling mode (FW) and the one that is decreasing, in this case line D, is the backward whirling (BW) mode.

Figure 2.6 shows the rotor mode shape plots at 5000 rpm rotation speed. The cylindrical mode shown in the top is the mode that occurs at 45.54 Hz (B) and the conical mode that is shown in the bottom is the mode that occurs at 74.28 Hz (D). Both of them are backward whirling modes. The other two modes at 45.55 Hz (C) and 79.69 Hz (E) are forward whirling modes which have the same shape, however, they have the opposite whirling direction.

In the Campbell diagram the support properties can vary somewhat. However, a diagram where the support stiffness is varied reveals information for bearing

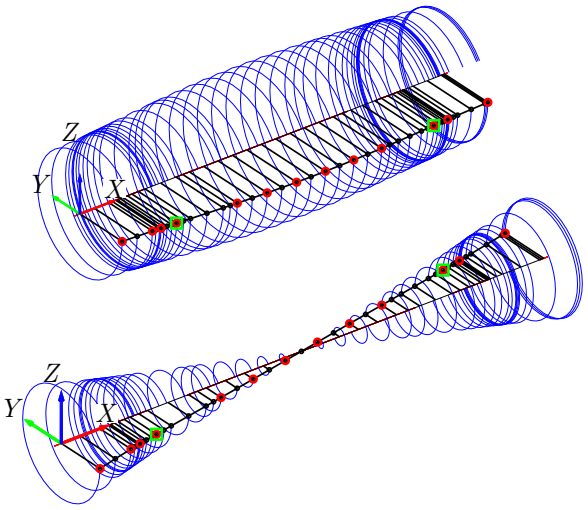

Figure 2.6. Backward mode shape plots at 5000 rpm. Top: cylindrical mode shape at 45.54 Hz, bottom: conical mode shape at 74.28 Hz.

selection and design. The diagram is called a critical speed map that shows the support stiffness effect at the critical speeds. Figure 2.7 shows a critical speed map. At low stiffness the first and second critical speed increases steadily and settles. On the other hand, the third mode is not affected at low stiffness, but with high support stiffness the critical speed is increased.

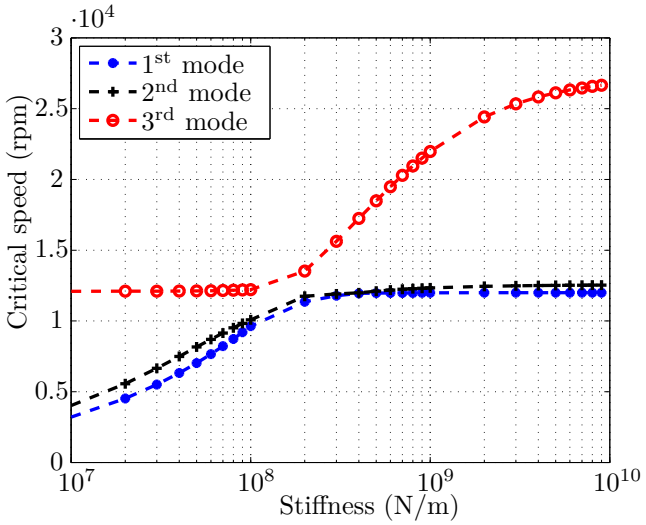

Figure 2.7. Critical speeds as a function of support stiffness.

Modeling of the support is a specific research topic and in the following sections a ball bearing modeling and active magnetic bearings are introduced. The supports affect the rotor's dynamical behavior dramatically and for example in the case of AMBs or journal bearings the supports enable operation above the first bending mode, which is difficult to achieve with rolling element bearings.

2.4 Ball bearing modeling

Bearings have an important role in all rotating machinery systems. One of the commonly used bearing types is a ball bearing. Modeling the dynamical behavior of a ball bearing includes several simultaneous contacts between the bearing components that make an accurate simulation of a ball bearing challenging and computationally heavy. The modeling and simulation provide accurate information of the dynamic performance of systems that contain ball bearings. However, depending on the complexity of the model, the computation time varies. It is possible to simulate ball bearings with excellent accuracy but in this case there is a need for more input parameters, including ones that are not widely available.

The basic concept in ball bearings is that the balls rotate inside two steel rings (races) and the balls are kept separate with a cage. The design varies depending on the specific type of bearing but the basic concept is the same in every ball bearing. Figure 2.8 describes the axial and transverse cross-section in the A-A plane of a ball bearing.

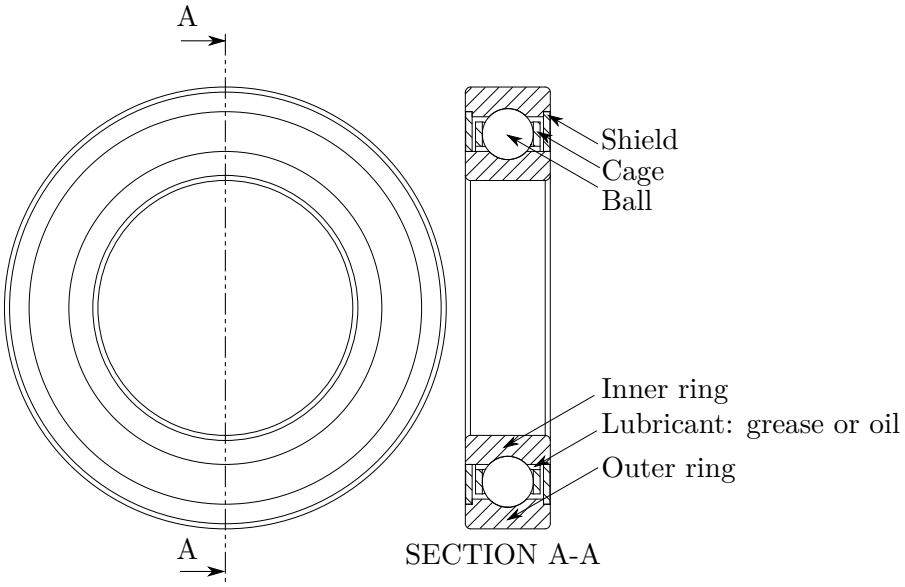

Figure 2.8. Cross-section in the A-A plane of a ball bearing.

Ball bearing models have been available since 1960, when Jones [24] presented a general theory for modeling an elastically constrained ball and a radial roller bearing. The model considers five degrees of freedom in the inner ring and includes the gyroscopic moments and centrifugal forces of the balls. The proposed model was verified later by Harris [18], and Hamrock and Dowson [17] who generalized the proposed theory. The proposed model did not include any geometrical imperfections, which led to numerous studies considering the effects of different kinds of defects in the bearing. There is also a general trend that the earlier models considered fever degrees of freedom than the more recently proposed models when studying the effects of imperfections to the dynamical behavior of rotor bearing systems.

Tandon and Choudhury [49] presented a thorough review for detecting defects in rolling element bearings. They classified bearing defects into two categories, distributed and localized. The defects caused by manufacturing error, improper installation or abrasive wear are called distributed defects; these include surface roughness, waviness, misaligned races and off-size rolling elements. The defects caused by fatigue are called localized defects; these include cracks, pits and spalls on the rolling surfaces.

Aktürk et al. [2, 1] proposed a three-degree-of-freedom ball bearing model where the effects of waviness, axial preload, and the number of balls were studied.

Jang and Jeong [19] proposed a five-degree-of-freedom model for a rigid rotor that is supported by at least two bearings. The model is used to study the waviness in races and balls. The results are verified by prior studies. Further, Jang and Jeong [20] included the gyroscopic moment and the centrifugal force of the balls in the model and studied the stiffness, contact force, displacement and vibration frequencies behavior with different waviness orders in each bearing and validated the results by prior researchers. Jang and Jeong [21] studied the effect of different waviness orders in the model that contains a pair of bearings and also the eccentricity of the center of mass of the rotor and bearing span center. Inertia forces were found to have a major effect when determining the bearing vibration frequencies.

Sopanen and Mikkola [46] presented a six-degrees-of-freedom ball bearing model theory where the sixth degree of freedom is the friction torque around the rotational axis. The model considers waviness in the inner and outer races as well as the localized defects in the races. In the second part, Sopanen and Mikkola [47] investigated the clearance variation on dynamical behavior, which was found to have a major effect. The low-order waviness generates vibrations at the frequencies at waviness orders multiplied with rotation speed. They also concluded that when the waviness is near the number of balls, the vibrations occur near the ball passage frequencies in the races. The localized defects were found to generate frequencies

at the bearing defect frequency. The results were verified by the results available in the literature. The model does not consider the centrifugal force and the gyroscopic moment.

Changqing and Qinqyu [9] propose a model that has five degrees of freedom and considers both centrifugal force and gyroscopic moment. They studied a rotor bearing system under internal clearance, axial preload, radial load and waviness. The first three were found to have a significant role in the system's stability, and the outer race waviness was found to have the most effect compared to the inner race and ball waviness. Changqing et al. [4] improved the proposed model and studied the axial preload effect on the ball bearing's dynamical behavior. In the study, it was concluded that the unstable periodic solution of a balanced rotor can be avoided with a proper axial preload.

Recently, Nakhaeinejad and Bryant [36] proposed a model of rolling element bearings by using a graphical vector bond method. The model consists of nine balls and two rings. The model includes centrifugal force and gyroscopic moment, contact elastic deflections and forces, contact slip, contact separation and defects on races. The model was verified with a test machine and by using the available solutions in the literature. However, the planar model does not consider the axial preload and its effect on the stiffness of the bearing. Xu et al. [57] studied a slider-crank mechanism where the revolute joint has been modeled as a ball bearing. The balls are modeled as individual parts. In the study, the clearance effect and the number of balls influencing the load that individual ball is having were studied. Xu et al. concluded that by having more balls, the load per individual part is decreased and the displacement is smaller compared to bearings that have fewer balls.

In conclusion, the research done in developing ball bearing models can be categorized into two main fields: the ones which consider dynamical forces due to high rotation speed and the simplified ones that do not. The research done earlier usually does not consider the dynamical forces, and the models developed more recently do. It has been found that the ball bearing that is modeled using five degrees of freedom can be used to simulate the dynamical behavior under imperfections due manufacturing and installation accurately. Friction force can be also added to the model, if the studied application has a special need for that, (*e.g.*, for studying the touchdown bearing behavior when magnetic bearings fail). However, when considering several degrees of freedom and inertia forces, solving the model becomes computationally heavy. Liew et al. [30] studied the effect of a two and a five-degrees-of-freedom bearing model with inertia and without. In the study, it was concluded that the five-degrees-of-freedom model with inertia forces needs approximately ten times more time to solve than without the inertia forces.

The objective of the ball bearing modeling *publications* (*I* and *II*) is to improve

the six-degrees-of-freedom ball bearing proposed by Sopanen and Mikkola [46, 47] by including the centrifugal force and the gyroscopic moment to the model. *Publication II* ([28]) The model is applied to a single structure and in *publication I* ([29]) it is applied to two additional structures with various sized bearings to discover more general behavior. The results obtained using the bearing models with and without ball inertia effects are compared and the justification for the inclusion of the computationally expensive centrifugal force and gyroscopic moment effects is discussed. Finally, the results are used to determine at what rotation speed inertia forces can be neglected and at what speed they are necessary to consider.

The two models implemented are divided into two categories. The first is referred to as the simplified model that is based on the relative displacements and velocities between the inner and outer races. Displacements and velocities can be calculated by creating a geometrical relationship. Accordingly, the relationship between the force-deflection can be expressed. The model has five degrees of freedom: three translational and two rotational degrees of freedom. The model includes non-linear Hertzian contact deformation. The geometry and material parameters are given as input and the bearing forces and torques are solved. The simplified model does not consider high-speed forces.

The second model is referred to as the refined model that is based on the force equilibrium between the external applied load and the internal load within the bearing. Rotation dependent forces, such as the centrifugal force and the gyroscopic moment of the ball are included. In the equilibrium condition, the deformation of the ball bearing is solved.

A set of justified simplifications are defined in the theory of bearing modeling. The friction torque and the effect of the hydrodynamic film are neglected in order to decrease model complexity without losing much of accuracy. The effects of those additional parameters are assumed to have similar effects on both models. Also the defects and form error of the bearing are not included and they are assumed to be perfectly manufactured (*i.e.*, the balls are round and races are circular). A more detailed theory of the bearing modeling can be found from [46, 29].

Ball bearings are one of the commonly used bearing types in industry. However, at high speeds the usage of ball bearings becomes more limited because the friction between the balls and the races causes the bearing to heat. Secondly, the characteristics of ball bearings include their high radial stiffness and low damping which are problematic especially in flexible rotors. [54] Thirdly, ball bearings require lubrication to work well. Lubrication needs to have lubrication system to the bearings or the grease in the bearings has to be changed periodically. In the next section another type of bearing, AMBs, are introduced.

2.5 Active magnetic bearings

Active magnetic bearings (AMB) is a type of bearing that uses magnetic force to levitate the rotor. The benefit compared to traditional rolling elements and journal bearings is that there is no mechanical contact between the rotor and stator. Due to the absence of contact there is no wear and lubrication is not required. In addition, the magnetic force is actively controlled which allows the control of the rotor's dynamical performance which is challenging or even not possible with other bearing topologies. The principle of an AMB supported rotor is depicted in Figure 2.9. [8]

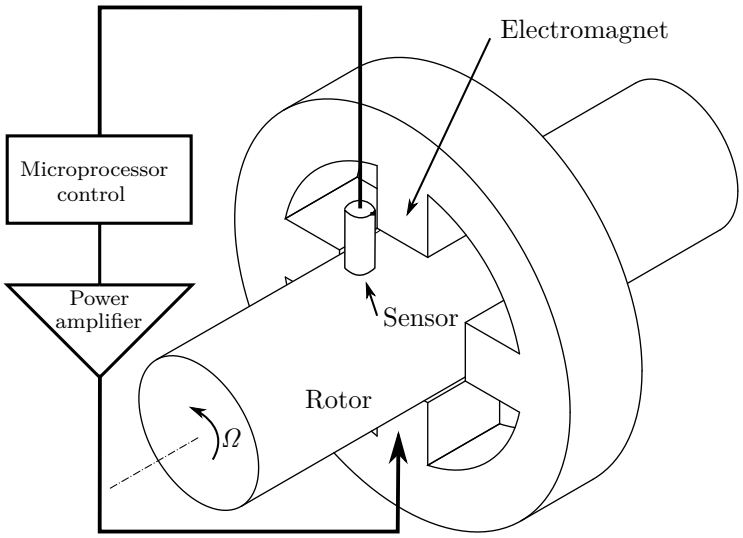

Figure 2.9. Active magnetic bearing working concept.

Due the nature of magnetic bearings they can only pull and for that reason the system is unstable without control and requires two opposite electromagnets to control the rotor movement in a single axis. The simplest practical control that would stabilize the system is a proportional-integral-derivative (PID) controller, which is also the most commonly used in the industry. [8]

The working principle for a single plane is that a sensor measures the rotor position. The measured position is compared to a reference position, which is for example the center of the bearing. The difference of the position is fed to a microprocessor. The microprocessor derives the control signal from the sensor information. The control signal is fed to a power amplifier that transforms the signal into current. The current is fed to the actuator coils resulting in a magnetic force pulling the rotor. When there is a sensor in at least two planes the rotor can be kept in the reference position. [8]

The magnetic bearing system can be considered to be similar to a simple mass-spring-damper system. In the mass-spring-damper system the mass, spring constant and damping coefficient describes the system behavior. In magnetic bearings the linearized force-displacement coefficient, k_x, that is also called position stiffness, is in a N/m unit. Also the force-current coefficient, k_i, which is also called to current stiffness, is in a N/A unit. To obtain these coefficients, an example of force by a pair of opposed symmetric electromagnets in single axis is shown. Figure 2.10 depicts the layout of the system.

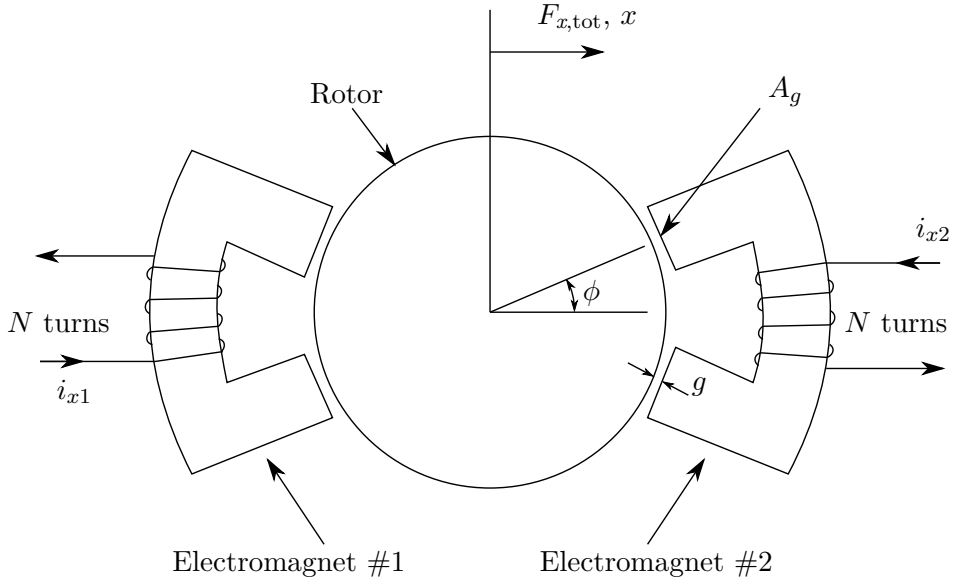

Figure 2.10. AMB system with opposed electromagnets.

The total force that can be achieved in a x-axis, $F_{x,\mathrm{tot}}$, for the system shown in Figure 2.10 be calculated as

$$F_{x,\mathrm{tot}} = F_{x2} - F_{x1} = \frac{A_g}{\mu_0}(B_{x2}^2 - B_{x1}^2) \tag{2.18}$$

$$= \frac{A_g}{\mu_0}\left(\frac{\mu_0^2 N^2 i_{x2}^2 \cos\phi}{4(g-x)^2} - \frac{\mu_0^2 N^2 i_{x1}^2 \cos\phi}{4(g+x)^2}\right) \tag{2.19}$$

$$= \frac{A_g \mu_0 N^2 \cos\phi}{4}\left(\frac{i_{x2}^2}{(g-x)^2} - \frac{i_{x1}^2}{(g+x)^2}\right), \tag{2.20}$$

where F_{x1} is the magnetic force to positive x-axis and F_{x2} is the magnetic force to negative axis, A_g is the air gap area, μ_0 is vacuum permeability, B is the magnetic flux density, N is the number of coil turns, ϕ is the angle between the magnet poles, i_{x1} and i_{x2} are the currents for the opposite magnet poles, g is the nominal air gap and x is the rotor position in the x-axis.

The force produced by magnetic bearing (eq. 2.20) is nonlinear in respect to the air gap and the current. Assuming that the movement is small, the air gap can be linearized. The current can be linearized by introducing a constant bias current, i_b, which together with controller current i_c forms the total current ($i_{x1} = i_b - i_c$, $i_{x2} = i_b + i_c$). The sign on the control current depends which direction the rotor is moved.

The equation 2.18 can be expressed in linearized form as

$$F_{x,\mathrm{tot}} = k_x x + k_i i, \tag{2.21}$$

where equation 2.20 is linearized in respect to current and air gap. This leads to current stiffness, k_i, and position stiffness k_x to be as

$$k_i = \left.\frac{\partial F_{x,\mathrm{tot}}}{\partial i_c}\right|_{x=x_0, i_c=i_{c0}} = \frac{\mu_0 N^2 A_g i_b \cos\phi}{g^2} \tag{2.22}$$

$$k_x = \left.\frac{\partial F_{x,\mathrm{tot}}}{\partial x}\right|_{x=x_0, i_c=i_{c0}} = \frac{\mu_0 N^2 A_g i_b^2 \cos\phi}{g^3}. \tag{2.23}$$

Magnetic bearings are applied to high demand applications, especially where oil-free operation is mandatory. These are, for example, underwater pumps or gas compression. Design of magnetic bearings often require model based simulation, where the studied structure is modeled in a way that the dynamics of the system and the auxillary components are included. This allows the use of advanced controllers. The method described in section 2.3 can be applied to create the model. The model can be used to design a controller for the system. In order to model the system properly deep understanding of the application is required. In *publication V* a compressor model is build and one performance measure is optimized.

Chapter 3

Summary of the findings

Simulation enables the finding of more complete and reliable designs than the conventional design tools would. In this dissertation simulation tools are used to find the limits and exceed the limits of conventional design. These are achieved through benchmarking two different complexity ball bearing models. The limits for the simulation models are found and the main findings are shown in this section. Exceeding the limits is achieved by simulating a compressor application where the load carrying capacity at the impeller location is improved at low frequencies.

This chapter is divided into three main sections. The first section shows an example of finding the boundaries in modeling and proposes when more detailed model is required. The second section describes the design process of a HS machine. The third section shows an example of exceeding the limits where through the use of an advanced controller the machine load capacity (*i.e.* how much load can be applied to the impeller at various frequencies before either the maximum load capacity of the AMB or allowable clearance is exceeded) was able to be improved. This research shows that the limits of current machines can be exceeded by the utilization simulation as a tool in the design process.

3.1 Bearing simulation

In *publications I* and *II*, two ball bearing models were compared against each other and the limits for the bearing models were identified for three different sized bearings. This publication shows that the limits can be identified through simulations. As result, in further simulation the model complexity can be considered to depend on the case.

Through the two ball bearing models the bearing stiffness coefficients were com-

pared. The model where rotation speed dependent variables that are centrifugal force and gyroscopic moment are neglected is referred to as the simplified model. The second model where speed dependent variables are included is referred to as the improved model. In *publications I* and *II* it is determined at which speeds the improved model predicts the bearing behavior more accurately. Motivation for the determination of the limits for bearing models arise from computational burden. The use of the improved model takes approximately ten times longer to obtain a solution compared to the simplified model.

First, in the study the ball bearing stiffness coefficients were calculated and compared. In addition to this a critical speed map where the support stiffness is varied from 10^7 N/m to 10^{10} N/m was examined. In the critical speed map the bearing stiffness is included and this shows the ball bearing models stiffness variation in relation to the critical speeds. It should be noted that the critical speed map depends highly on the rotor geometry being studied. In the end a Campbell diagram was studied for both of the bearing models and the difference could be observed. In this section one case, which is referred in *publications I* and *II* as "turbo blower" is shown together with the results for the machine.

In Figure 3.1 the bearing stiffness coefficients are shown. In the top the stiffness coefficients in the axial direction are shown and in the bottom for radial directions in a function of rotation speed. In the stiffness calculation, a speed of 16000 rpm was the maximum calculated value due it being the maximum value that the manufacturer suggest to be used for this specific bearing.

It can be seen that the stiffness values at zero rotation speed are equal, and that above 2000 rpm stiffness begins to diverge because in the improved model the centrifugal force and gyroscopic moments are affecting the balls. In the maximum evaluated speed the axial stiffness is decreased by a total of 18.0%, in the radial direction (y) by 27.0% and in z-direction, where the rotor load is applied, by 30.0% from the initial stiffness coefficients.

Second, in the critical speed map, the effect of the support stiffness on the critical speeds are shown. From this, it can be seen how increasing the bearing stiffness coefficient affects the critical speeds. At a low stiffness, the support stiffness primarily defines the critical speeds. Once the support stiffness increases enough, the critical speeds reach a constant value (*i.e.* increasing the bearing stiffness has no effect on the critical speed). Above this point, the rotor flexibility is defining the critical speeds.

Figure 3.2 shows the critical speed map where the radial bearing stiffness vary. In this figure the axial stiffness coefficient is zero. The critical speed map is plotted on the zero rotation speed for an unconstrained system. The first three modes are shown for the system where the two first are rigid body modes and the third is the first flexible mode.

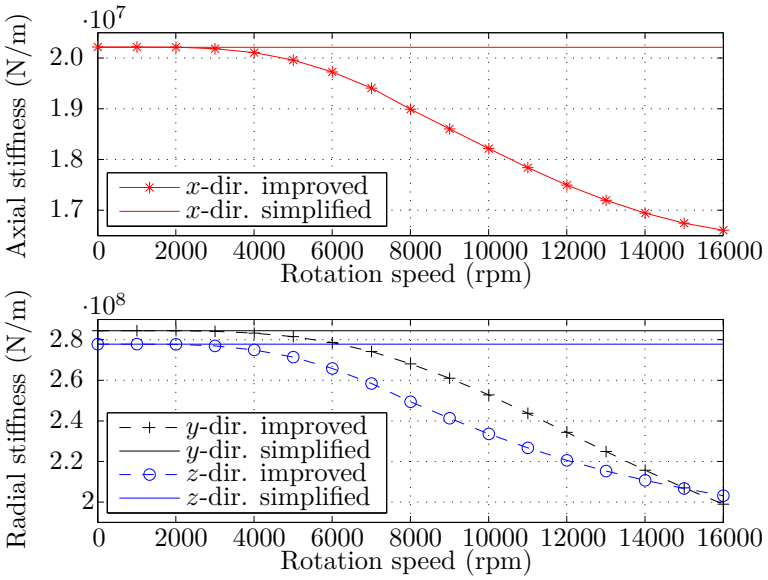

Figure 3.1. Bearing stiffnesses in the axial and radial directions as a function of rotation speed in turbo blower (0–16000 rpm).

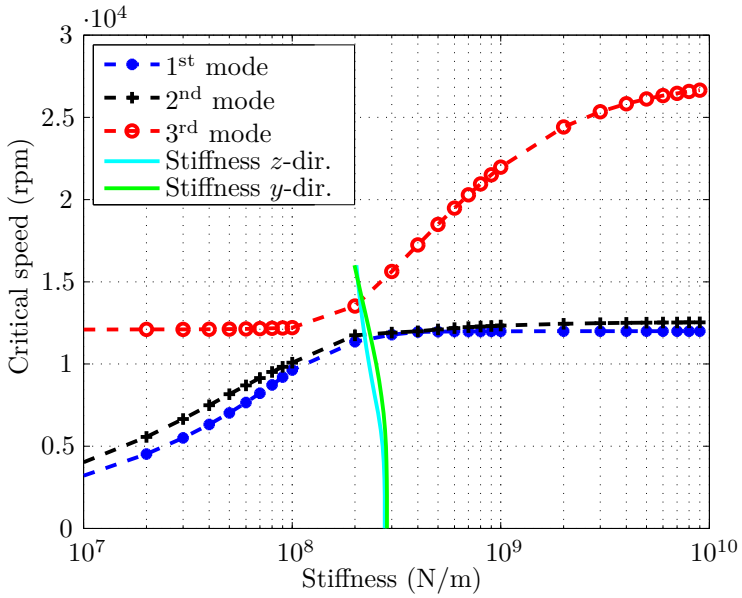

Figure 3.2. Undamped critical speed map. The radial stiffness is varied at zero velocity.

The first two modes have an inclining section when the bearing stiffness increases above $2.0 \cdot 10^8$ N/m. Below this value, bearing stiffness mainly determines the critical speeds of the rotor system. Correspondingly, for bearing stiffnesses higher than $2.0 \cdot 10^8$ N/m, the flexibility of the rotor has a more significant influence on the critical speeds. In this case, the variation of bearing stiffness will have an effect on the third mode but not on the first two modes.

In the Campbell diagram, the natural frequencies of the rotor-bearing systems are shown as a function of rotation speed. The critical speeds are found from the diagram. The Campbell diagrams with both ball bearing models is shown in Figure 3.3.

It can be seen in Figure 3.3 that the Campbell diagrams are identical up to 6000 rpm rotation speeds and as the rotation speed increases, the whirling frequencies start to differ. The first two critical speeds occur approximately at the same rotation speed in both bearing models. The third and fourth critical speeds occur in the improved bearing model at a lower rotation speed than in the simplified bearing model. The first critical speed is a backward whirling mode, the second is also a backward whirling mode, the third is a forward whirling mode and the fourth is a backward whirling mode (see Figure 3.3). A comparison of the critical speeds in the two bearing models is shown in Table 3.1.

Table 3.1. Turbo blower critical rotation speed from the Campbell diagram (Figure 3.3).

#	Critical speed (rpm)		
	Simplified model	Improved model	Difference [%]
1	8378	8372	0.07
2	8836	8816	0.23
3	13977	12861	8.68
4	14160	13065	8.38

The first two critical speeds occur close to each other and there is no clear difference between the models used to study this case. A clear difference can be seen at the third and fourth critical speeds. The critical speeds in the case of a high-speed ball bearing model are over 8% lower than with the simplified bearing model. The obtained results are in agreement with the critical speed map (Figure 3.2) where the first and second critical speeds are not affected by the different bearing stiffnesses as the third and fourth critical are.

Similar analyses were done for two other structures and a summary based on all of the studied cases in *publications I* and *II* is as follows:

In all the cases the bearing stiffness is constant until a specific rotation speed, which depends on the bearing size and then decreases with the improved model as the centrifugal force and gyroscopic moment affect the balls. Based on the

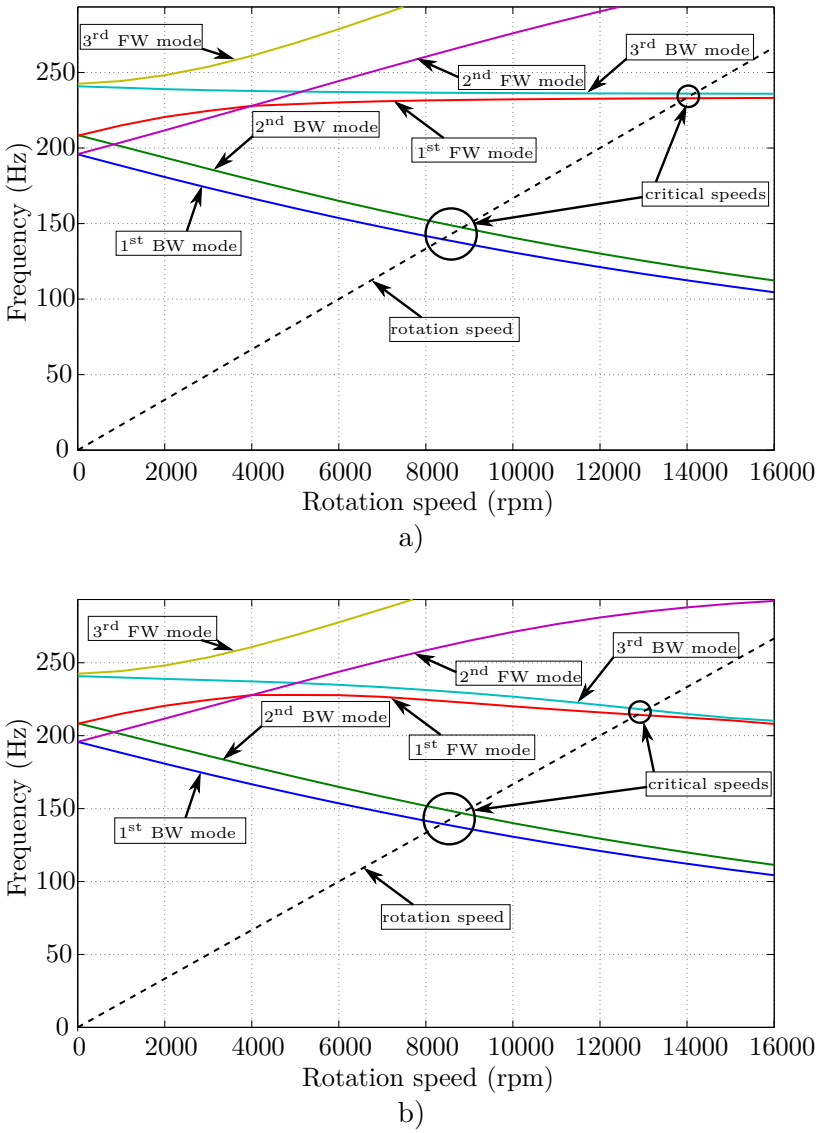

Figure 3.3. Campbell diagrams of the turbo blower: a) simplified bearing model and b) improved bearing model.

studied cases, the range where the stiffness is constant shows a linear relationship with the bore diameter. The relationship shows that the smaller the bearing, the higher percentage from the maximum rotation speed the bearing can be rotated before the stiffness decreases due to the centrifugal force and gyroscopic moment

affecting the balls.

In the next section, the design process of a high-speed electrical machine is shown. The design process is the basis for the high-speed electrical machine design process. Parallel to the design process simulation tools can be used to enable a more complete and reliable design.

3.2 Design process

Publications III [51] and *IV* [52] consider the limitations of high-speed electrical machines and propose a multidisciplinary design process for a PMSM consisting of six stator slots and two poles as well as a diametrically magnetized permanent magnet and a tooth-coil wound stator in high-speed applications. Even though the proposed design procedure is intended for the aforementioned PMSM type, it can be applied, with slight modifications, to other electrical machine types.

The design process of a HS machine involves several steps prior to construction of the first prototype. Figure 3.4 shows a general design flow chart for a HSPMSM. The design process is divided into nine steps. These steps are tasks for engineers and all have input and output design variables. Each of the steps should yield results that satisfy the design requirements (Step 1). The flow chart has six decision points where the fulfilment of the requirements list is verified. If the requirements are not met, then a new iteration round is required. Each step creates additional information and introduces further requirements, *e.g.*, in Step 2 a maximum shaft diameter can be evaluated from the initial requirements. If all the requirements are fulfilled, the process can proceed to the next step; otherwise the design should be changed until satisfactory results are achieved. In Figure 3.4 the proposed actions to satisfy the additional requirements are shown on the right side. When all of the steps are completed and the design requirements are fulfilled, the first prototype can be built. A detailed explanation for each step can be found in *publication III*.

The design process of an electrical machine is thus a highly iterative process and, for that reason, many concepts need to be analyzed before the final solution is found. The required calculations can first be done with analytical electromagnetic, thermal and structural analyses in order to constrain the dimensions. The constrained dimensions can then be used as a starting point in subsequent steps. FEM analysis can be used in the verification or to study the structure in more detail.

The proposed design process is specially developed and tested for a HSPMSM having 6 slots and 2 poles. The decision to consider a specific type of machine was made in order to limit the machine topology design variations, to simplify the initial design stage and to concentrate on the special features of the proposed

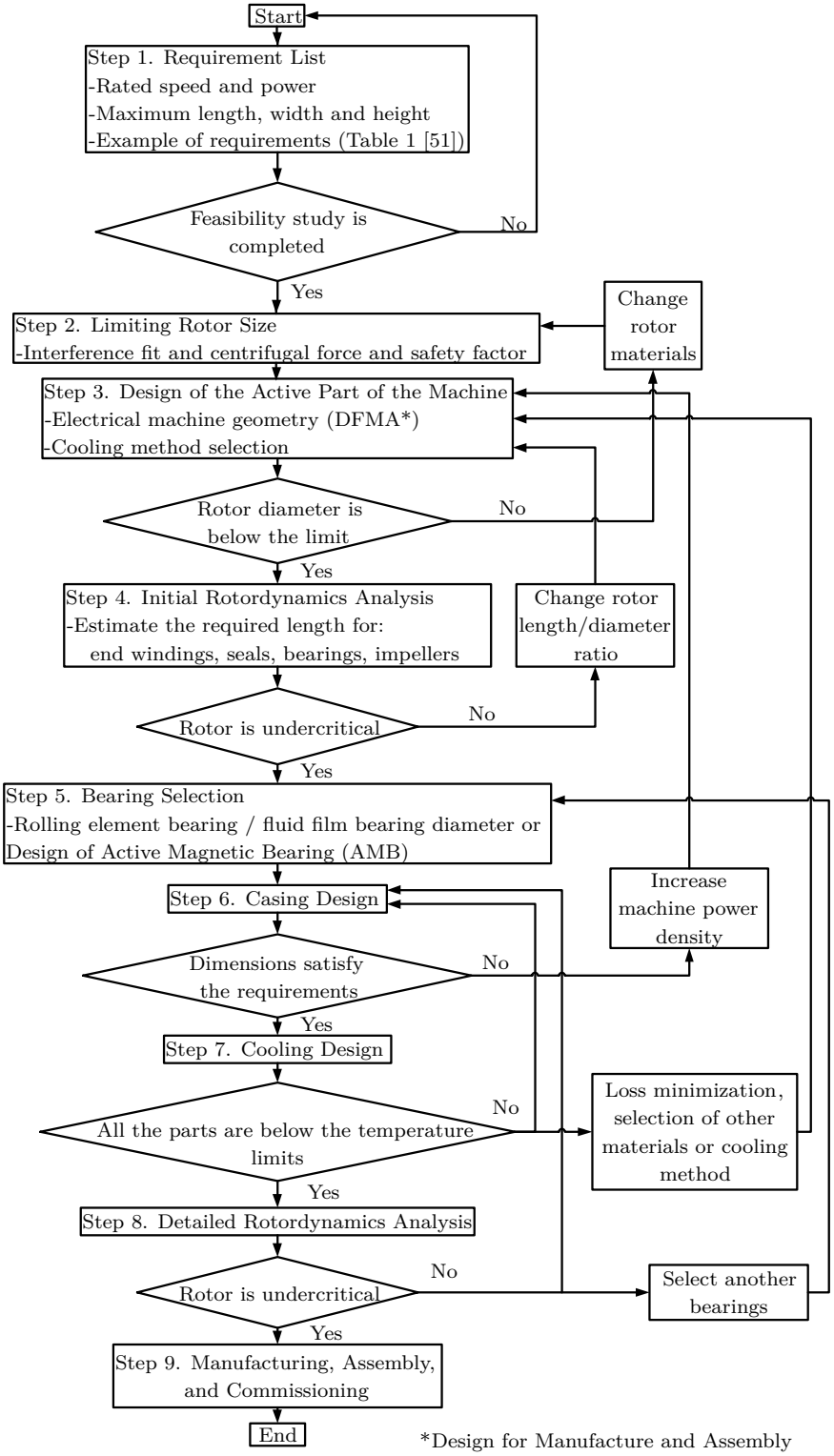

Figure 3.4. Design flow chart for a high-speed permanent magnet synchronous machine.

machine topology. In this type of machine the electromagnetic forces do not cause major effect due symmetrical stator structure and the utilization of permanent magnet that leads to longer air gap length compared to induction machines. [22]

An example of the utilization of simulation in the flow charts in step 4 is shown. In step 4 the initial rotordynamics analysis is done. An example is shown for two different rotors where one is short and one approximately twice longer. The developed prototypes shown in [51] utilize tooth-coil windings (TCW) configurations which do not require much space and enables a short rotor. Another winding option that could be utilize is distributed windings (DW). However, that would lead to the rotor being longer due to the fact that DW protrusion length in 2-pole machines requires more space to accommodate inside the electrical machine. Figure 3.5 depicts a critical speed map for a short rotor that uses TCW and a long rotor that uses DW. The solid lines refer to the TCW structure and the dashed lines to the structure in which DW are utilized. The vertical lines represent typical bearing stiffnesses with different bearing topologies. Magnetic bearings have an approximate stiffness value of $1 \cdot 10^6$ N/m, journal bearings $5 \cdot 10^7$ N/m, and ball bearings $1 \cdot 10^8$ N/m. The bearing stiffness margin in Figure 3.5 is $\pm$ 10% and the given values are in the radial direction. In the end, the longer rotor represents the case where the end windings require more space than assumed in the initial analysis. Practically, the longer the rotor the lower the critical speeds. A rotor that requires high critical speeds has to be short. A short design also leads to a smaller and lighter machine, which is usually a desired feature.

As a conclusion, Figure 3.5 shows that increasing the length of the rotor leads to lower critical speeds. For example, with ball bearings the achievable stiffnesses are in range of $1 \cdot 10^8$ N/m. With TC windings, the first critical speed is 70000 rpm, the second 72 000 rpm and the third 145000 rpm. If the active part length is increased by 50% because of the distributed windings, the first critical speed drops to 35000 rpm, the second to 71000 rpm, and the third to 100000 rpm. In this case, the first and the third critical speeds have the biggest change when the length is increased as the second critical speed is almost the same with both models. By extension of the length of the active part, the first critical speed is reduced to half of that of the original structure. For undercritical operation with a 20% safety margin the machine with TC windings could be driven at the rated speed of 56000 rpm and the machine with DW at the rated speed of 28000 rpm.

In the next section a HS machine simulation model was developed that is utilized in a chiller compressor application. The aim is to improve performance at low frequencies. In order to improve the performance a full model of a chiller was developed and a control algorithm was designed.

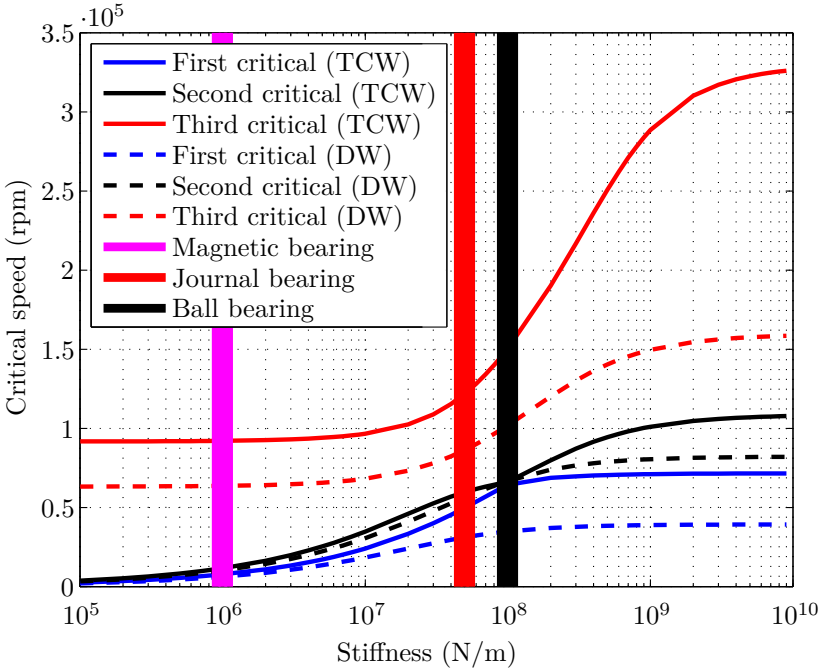

Figure 3.5. Critical speeds with TC winding structure (solid lines) and with the 50% longer DW structure (dashed lines).

3.3 Compressor machine load capacity at low frequencies

In *publication V* dynamic machine load capacity at the impeller location in the radial direction in a chiller compressor application was studied. It is a measure of how much load can be applied to the impeller at various frequencies before either the maximum load capacity of the AMB or the allowable clearance is exceeded. This measure will be referred to as the machine load capacity.

The maximum machine load capacity at the impeller location as a function of frequency is compared with the five different control designs. Four controllers are PID controllers *i.e.* first and second order centralized PID controllers as well as first and second order decentralized controllers. The fifth controller is a full MIMO ($\mathcal{H}_\infty$) controller.

The maximum machine load capacity at the impeller location as a function of frequency is compared with the five different control designs. First, the machine load capacity for the system controlled with a second order decentralized PID controller is shown along with the defined performance measures. Figure 3.6 depicts the over all machine load capacity limit as well as the allowable load at the impeller (w_1) without exceeding the individual performance limits which are

bearing maximum force and clearance ($\bar{z}_{1..4}$). $\bar{z}_1$ and $\bar{z}_2$ are the maximum bearing forces, where the first is located closer to the impeller. Similarly $\bar{z}_3$ and $\bar{z}_4$ are the clearances at the bearing location, where the first is located closer to the bearing. Figure 3.6 depicts the performance measurements over low frequencies. It can be seen that the machine load capacity is simply a piecewise continuous combination of the minimum individual performance measures at each frequency. Details of the calculations can be found in *publication V*.

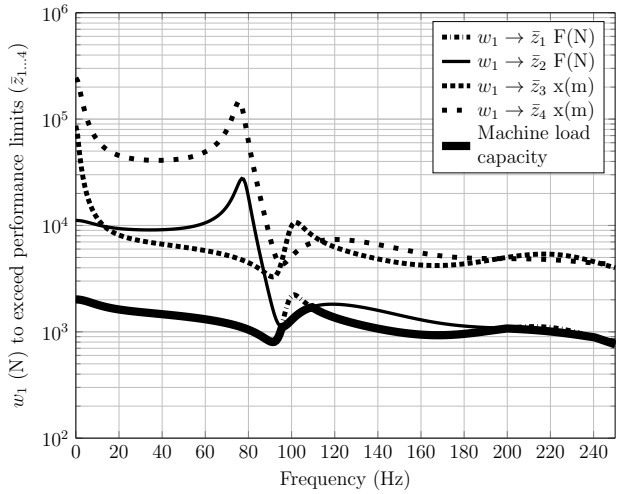

Figure 3.6. Machine load capacity limit for each performance measurement.

Second, the machine load capacities with the other four controllers and the limiting performance are studied. In Figure 3.7, the machine load capacity with the first and second order decentralized and centralized PIDs, $\mathcal{H}_\infty$ controller and limiting performance for the studied case are shown. Limiting performance is defined to be the maximum machine load capacity for the chosen case study, that can be theoretically achieved (see details in *publication V*). It can be seen that the PID controllers have low performance compared to the higher order $\mathcal{H}_\infty$ controller. This is due the fact that the higher order controller can be specifically tuned over a specific frequency range where as PID controllers have limited options over a specific frequency range.

Third, the machine load capacity calculation is repeated for the 40% longer bearings. Figure 3.8 depicts the machine load capacity with the original bearing with $\mathcal{H}_\infty$ control as well as the 40% longer bearing performance results.

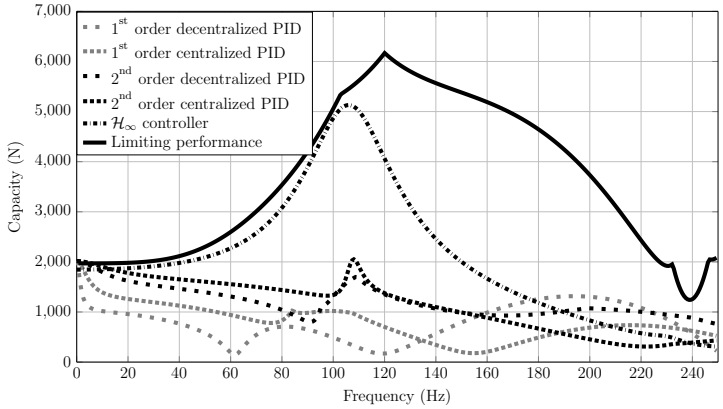

Figure 3.7. Machine load capacity at the impeller location.

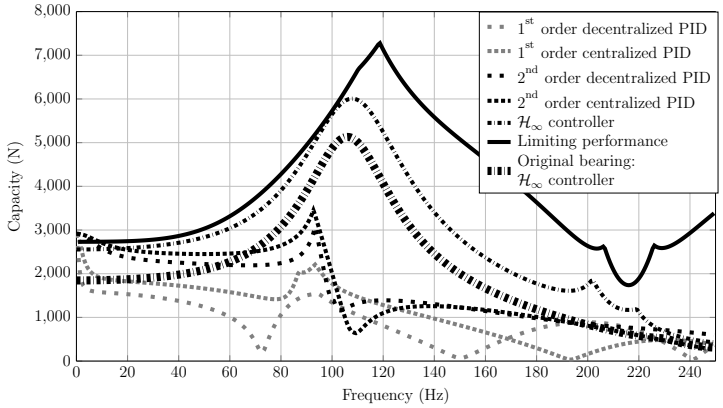

Figure 3.8. Machine load capacity at the impeller location with 40% longer bearings and with the original bearing machine load capacity with $\mathcal{H}_\infty$ controller.

The machine load capacity at the impeller location in a single-stage centrifugal compressor supported with AMB's is studied. Two models were developed and five control designs were developed and analyzed for each model. The following conclusions can be made:

- Lack of machine load capacity over the surge/stall (0–100 Hz) frequency range is not fundamental to the technology but may be an artifact of the specific choice to use PID controllers.
- Improved surge/stall performance may often be accomplished without costly hardware replacement and only requires software modifications.
- Improving magnetic actuator capacity may often not be the most effective way to increase machine load capacity in the surge/stall regime

Chapter 4

Conclusions

In this dissertation, specific aspects of designing rotating electrical machinery were discussed. Special attention was paid on the multidisciplinary design process, bearing simulation and improving magnetic bearing supported system performance by coupled simulations at low frequencies.

In the bearing analysis, two different ball bearing models were implemented in three varied sized rotors that were supported with identical bearings and the model performance was compared. Rotation speeds were determined for these rotors regarding up to which rotation speed the simplified model would predict the behavior accurately.

The bearing stiffness is constant with the simplified model due the fact that it does not consider any speed dependent variables. This model predicts well if the inertia effects are small. Inertia effects are small at low or medium rotation speeds.

The complex model has inertia effects, *i.e.*, centrifugal force and gyroscopic moment are included. This model requires up to ten times more computationally burden due speed dependent variables. However, this model predicts the behavior more accurately in high speeds. The inclusion of inertia effects causes the importance of stiffness to decrease as these forces are significant.

The design process of high speed machines is multidisciplinary and highly iterative due to the complex interaction of the many design variables involved. Consequently no single optimum solution exists and multiple possible solutions can meet the requirements.

In the design process study a multidisciplinary systematic design process for high speed permanent magnet synchronous machines is introduced. A flow chart is

presented and the process is applied to two machines. Following the proposed design flow chart, the design of these machines is systematic and leads to a faster design times due to less iterations and mistakes. In the design process the electromagnetics, mechanical stresses, rotordynamics, thermal analysis and manufacturing and assembly are highlighted. The design process considers the requirements for the machine and proceeds step-by-step in a way that the previous step must be satisfactory in order to proceed to next step.

In the AMB study, it was shown that it is possible to study and improve system performance with coupled simulation models. This enables finding novel solutions without building a prototype. In the study a compressor application was modeled and simulations were made in order to improve load capacity in radial direction in a compressor application at low frequencies. It was found that with an advanced controlled magnetic bearing supported compressor the rotor can withstand significantly more load at the impeller location at low frequencies.

In the electrical machine design process the use of standard tools of electrical machine design and the absence of simulation parallel to the design process prevents the development of better rotating electrical machines.

It was shown that the simulation tools enable *finding the limits* of systems which is shown by an example of two ball bearing models. Second, simulation tools can help to *exceed the limits* of systems, which is shown by the AMB supported compressor used to maximize the load capacity in the impeller location through a different control algorithm.

4.1 Suggestions for the future work

The close interaction with simulation in the design process has shown promising results. It allows to benchmark performance already in the design phase. Also, simulation can be used as well as to optimize machines that are already build.

In the bearing simulation study the used bearing model could be applied to other rotor structures and it could have been possible to perform an experiment with a physical rotor. This would enable to have a more general rule on when it is required to use the complex model to estimate system performance accurately. Also other types of rolling element bearings exist and in those a similar study could be performed to understand in more detail when it is necessary include centrifugal and gyroscopic moments to the model.

In the design process, the proposed design methodology could be refined so that it can adapt to other HS electrical machine topologies. For engineers implementing this design process to a single software would lead to a faster design time.

In the AMB study, it was found that an advanced controller could give significant performance improvements in a compressor application. To continue this work,

implementing the designed controller to an actual machine would be the next step. The study could be extended to other applications where in low frequencies high machine load capacity is required.

[1] Aktürk, N. The effect of waviness on vibrations associated with ball bearings. *Journal of Tribology 121*, 4 (1999), 667–677.

[2] Aktürk, N., Uneeb, M., and Gohar, R. The effects of number of balls and preload on vibrations associated with ball bearings. *Journal of Tribology 119*, 4 (1997), 747–753.

[3] Arkkio, A., Jokinen, T., and Lantto, E. Induction and permanent-magnet synchronous machines for high-speed applications. In *International Conference on Electrical Machines and Systems (ICEMS)* (2005).

[4] Bai, C., Zhang, H., and Xu, Q. Effects of axial preload of ball bearing on the nonlinear dynamic characteristics of a rotor-bearing system. *Nonlinear Dynamics 53*, 3 (2008), 173–190.

[5] Bathe, K.-J. *Finite Element Procedures*, 1st ed. Prentice-Hall, New Jersey, 1996.

[6] Bernard, N., Martin, F., and El-Hadi Zaïm, M. Design methodology of a permanent magnet synchronous machine for a screwdriver application. *IEEE Transactions on Energy Conversion 27*, 3 (2012), 624–633.

[7] Binder, A., and Schneider, T. High-speed inverter-fed AC drives. In *International Aegean Conference on Electrical Machines and Power Electronics (ACEMP)* (2007).

[8] Bleuler, H., Cole, M., Keogh, P., Larsonneur, R., Maslen, E., Okada, Y., Schweitzer, G., and Traxler, A. *Magnetic Bearings: Theory, Design, and Application to Rotating Machinery*, 1st ed. Springer Science & Business Media, Berlin Heidelberg, 2009.

[9] Changqing, B., and Qingyu, X. Dynamic model of ball bearings with internal clearance and waviness. *Journal of Sound and Vibration 294*, 1 (2006), 23–48.

[10] Chen, W., and Gunter, E. *Introduction to Dynamics of Rotor-Bearing Systems*, 1st ed. Trafford Publishing, 2005.

[11] Cheng, F., Xu, H., and Xue, S. Study on the design method of high speed permanent magnet synchronous machine. In *International Conference on Electrical Machines and Systems (ICEMS)* (2011).

[12] Cook, R., Malkus, D., and Plesha, M. *Concepts and Applications of Finite Element Analysis*, 3rd ed. John Wiley & Sons, Hoboken, 2007.

[13] Drury, B. *Control Techniques Drives and Controls Handbook*, 2nd ed. The Institution of Engineering and Technology, United Kingdom, 2009.

[14] Genta, G. *Dynamics of Rotating Systems*, 1st ed. Springer, New York, 2005.

[15] Gerada, D., Mebarki, A., Brown, N. L., Gerada, C., Cavagnino, A., and Boglietti, A. High-speed electrical machines: Technologies, trends, and developments. *IEEE Transactions on Industrial Electronics 61*, 6 (2014), 2946–2959.

[16] Gieras, J. F. *Permanent Magnet Motor Technology: Design and Applications*, 2nd ed. CRC press, Boca Raton, 2002.

[17] Hamrock, B. J., and Dowson, D. *Ball Bearing Lubrication: the Elastohydrodynamics of Elliptical Contacts*, 1st ed. Wiley-Interscience, New York, 1981.

[18] Harris, T. A., and Kotzalas, M. N. *Advanced Concepts of Bearing Technology: Rolling Bearing Analysis*, 5th ed. CRC Press, Boca Raton, 2006.

[19] Jang, G., and Jeong, S.-W. Nonlinear excitation model of ball bearing waviness in a rigid rotor supported by two or more ball bearings considering five degrees of freedom. *Journal of Tribology 124*, 1 (2002), 82–90.

[20] Jang, G., and Jeong, S.-W. Analysis of a ball bearing with waviness considering the centrifugal force and gyroscopic moment of the ball. *Journal of Tribology 125*, 3 (2003), 487–498.

[21] Jang, G., and Jeong, S.-W. Vibration analysis of a rotating system due to the effect of ball bearing waviness. *Journal of Sound and Vibration 269*, 3 (2004), 709–726.

[22] Jastrzębski, R. P., Smirnov, A., Hynynen, K., Nerg, J., Sopanen, J., Lindh, T., Heikkinen, J., and Pyrhönen, O. Commissioning and control of the AMB supported 3.5 kW laboratory gas blower prototype. *Solid State Phenomena 198* (2013), 451–456.

[23] Jokinen, T., and Luomi, J. High-speed electrical machines. In *Conference on High Speed Technology* (1988).

[24] Jones, A. A general theory for elastically constrained ball and radial roller bearings under arbitrary load and speed conditions. *Journal of Basic Engineering 82*, 2 (1960), 309–320.

[25] Kolondzovski, Z., Arkkio, A., Larjola, J., and Sallinen, P. Power limits of high-speed permanent-magnet electrical machines for compressor applications. *IEEE Transactions on Energy Conversion 26*, 1 (2011), 73–82.

[26] Kurvinen, E., Dmitrochenko, O., Matikainen, M., and Mikkola, A. Comparison of deterministic multibody simulation and random analysis in a linearized model of a vibratory feeder. In *the 11th Finnish Mechanics Days* (2012).

[27] Kurvinen, E., and Eskelinen, H. Improving the product design process by applying DFMA case: PM motor. *International Review of Mechanical Engineering 6*, 6 (2012), 1297–1301.

[28] Kurvinen, E., Sopanen, J., and Mikkola, A. Comparison of ball bearing model performance with and without centrifugal and gyroscopic forces. In *International Mechanical Engineering Congress and Exposition (IMECE)* (2014).

[29] Kurvinen, E., Sopanen, J., and Mikkola, A. Ball bearing model performance on various sized rotors with and without centrifugal and gyroscopic forces. *Mechanism and Machine Theory 90* (2015), 240–260.

[30] Liew, A., Feng, N., and Hahn, E. Transient rotordynamic modeling of rolling element bearing systems. *Journal of Engineering for Gas Turbines and Power 124*, 4 (2002), 984–991.

[31] Lindh, P., Heikkinen, J., Kurvinen, E., Pyrhönen, J., and Naumanen, V. The multidisciplinary design of rotor geometry in a permanent magnet traction motor. *International Review of Electrical Engineering (IREE) 8*, 5 (2013), 1437–1445.

[32] Lindh, P., Lindh, T., Heikkinen, J., Kurvinen, E., Satrustegui De Legarra, M., and Martinez-Iturralde Maiza, M. Indirect water cooling system improvements for vehicle motor applications. In *International Conference on Compatibility and Power Electronics (CPE)* (2015).

[33] Lindh, P., Pyrhönen, J., Polikarpova, M., Kurvinen, V., Heikkinen, J., and Naumanen, V. Electrical and mechanical design of a PM traction

motor with tooth coils. In *Conference on Power Electronics and Applications (EPE)* (2013).

[34] Motavalli, S. Review of reverse engineering approaches. *Computers and Industrial Engineering 35*, 1 (1998), 25–28.

[35] Nagy, R. L., Ullman, D. G., and Dietterich, T. G. A data representation for collaborative mechanical design. *Research in Engineering Design 3*, 4 (1992), 233–242.

[36] Nakhaeinejad, M., and Bryant, M. D. Dynamic modeling of rolling element bearings with surface contact defects using bond graphs. *Journal of Tribology 133*, 1 (2011), 1–12.

[37] Pahl, G., and Beitz, W. *Engineering Design: A Systematic Approach*, 3rd ed. Springer Verlag, United Kingdom, 2007.

[38] Pakaste, R., Laukia, K., Wilhelmson, M., and Kuuskoski, J. Experience with azipod propulsion systems on board marine vessels. *ABB Review 2* (1999), 1–12.

[39] Pyrhönen, J., Jokinen, T., and Hrabovcová, V. *Design of Rotating Electrical Machines*, 1st ed. John Wiley & Sons, United Kingdom, 2009.

[40] Pyrhönen, J., Lindh, P., Polikarpova, M., Kurvinen, E., and Naumanen, V. Heat-transfer improvements in an axial-flux permanent-magnet synchronous machine. *Applied Thermal Engineering 76* (2015), 245–251.

[41] Ranft, C. J. G. *Mechanical design and manufacturing of a high speed induction machine rotor*. PhD thesis, North-West University, 2010.

[42] Rao, J. Finite element methods for rotor dynamics. In *History of Rotating Machinery Dynamics*, vol. 20 of *History of Mechanism and Machine Science*. Springer Netherlands, 2011.

[43] Richtlinie, V. Methodik zum Entwickeln und Konstruieren Technischer Systeme und Produkte. In *VDI Richtlinie 2221*. VDI-Verlag Düsseldorf, 1993.

[44] Schmied, J., and Pradetto, J. Behavior of a one ton rotor being dropped into auxiliary bearings. In *Third International Symposium on Magnetic Bearings* (1992).

[45] Sohlenius, G. Concurrent engineering. *CIRP Annals-Manufacturing Technology 41*, 2 (1992), 645–655.

[46] Sopanen, J., and Mikkola, A. Dynamic model of a deep-groove ball bearing including localized and distributed defects. Part 1: Theory. *Proceedings of the Institution of Mechanical Engineers, Part K: Journal of Multi-body Dynamics 217*, 3 (2003), 201–211.

[47] Sopanen, J., and Mikkola, A. Dynamic model of a deep-groove ball bearing including localized and distributed defects. Part 2: Implementation and results. *Proceedings of the Institution of Mechanical Engineers, Part K: Journal of Multi-body Dynamics 217*, 3 (2003), 213–223.

[48] Staub, A. O., and Owen, E. Solid-state motor controllers. *IEEE Transactions on Industry Applications IA-22*, 6 (1986), 1113–1120.

[49] Tandon, N., and Choudhury, A. A review of vibration and acoustic measurement methods for the detection of defects in rolling element bearings. *Tribology International 32*, 8 (1999), 469–480.

[50] Tong, W. *Mechanical Design of Electric Motors*, 1st ed. CRC Press, Boca Raton, 2014.

[51] Uzhegov, N., Kurvinen, E., Nerg, J., Pyrhönen, J., Sopanen, J., and Shirinskii, S. Multidisciplinary design process of a 6-slot 2-pole high-speed permanent magnet synchronous machine. *IEEE Transactions on Industrial Electronics 99 Accepted* (2015), 1–12.

[52] Uzhegov, N., Kurvinen, E., and Pyrhönen, J. Design limitations of 6-slot 2-pole high-speed permanent magnet synchronous machines with tooth-coil windings. In *Conference on Power Electronics and Applications (EPE)* (2014).

[53] van Millingen, R., and van Millingen, J. Phase shift torquemeters for gas turbine development and monitoring. In *International Gas Turbine and Aeroengine Congress and Exposition* (1991).

[54] Vance, J. M., Zeidan, F. Y., and Murphy, B. *Machinery Vibration and Rotordynamics*, 1st ed. John Wiley & Sons, New Jersey, 2010.

[55] Waide, P., and Brunner, C. U. *Energy-Efficiency Policy Opportunities for Electric Motor-Driven Systems*. OECD Publishing, 2011.

[56] Widmer, J. D., Martin, R., and Kimiabeigi, M. Electric vehicle traction motors without rare earth magnets. *Sustainable Materials and Technologies 3* (2015), 7–13.

[57] Xu, L.-X., Yang, Y.-H., Li, Y.-G., Li, C.-N., and Wang, S.-Y. Modeling and analysis of planar multibody systems containing deep groove ball bearing with clearance. *Mechanism and Machine Theory 56*, 1 (2012), 69–88.

Publication I

Kurvinen E., Sopanen J., and Mikkola A.
Ball Bearing Model Performance on Various Sized Rotors with and without Centrifugal and Gyroscopic Forces

Reprinted from
Mechanism and Machine Theory
Vol. 90, pp. 240–260, 2015.

Mechanism and Machine Theory 90 (2015) 240–260

Contents lists available at ScienceDirect

Mechanism and Machine Theory

journal homepage: www.elsevier.com/locate/mechmt

Ball bearing model performance on various sized rotors with and without centrifugal and gyroscopic forces

Emil Kurvinen *, Jussi Sopanen, Aki Mikkola

Lappeenranta University of Technology, Department of Mechanical Engineering, P.O. Box 20, FI-53851 Lappeenranta, Finland

ARTICLE INFO

Article history:
Received 23 July 2014
Received in revised form 13 January 2015
Accepted 27 March 2015
Available online xxxx

Keywords:
Ball bearing
Centrifugal forces
Dynamical analysis
Gyroscopic moment
Inertia effect

ABSTRACT

Bearing performance significantly affects the dynamic behaviors and estimated working life of a rotating system. A common bearing type is the ball bearing, which has been under investigation in numerous published studies. The complexity of the ball bearing models described in the literature varies. Naturally, model complexity is related to computational burden. In particular, the inclusion of centrifugal forces and gyroscopic moments significantly increases the system degrees of freedom and lengthens solution time. On the other hand, for low or moderate rotating speeds, these effects can be neglected without significant loss of accuracy. The objective of this paper is to present guidelines for the appropriate selection of a suitable bearing model for three case studies. To this end, two ball bearing models were implemented. One considers high-speed forces, and the other neglects them. Both models were used to study three structures, and the simulation results were compared. The bearing behavior is studied at different shaft rotation speeds and the simulation results are used to determine when the model containing the centrifugal and gyroscopic forces should be used.

1. Introduction

Bearings have an important role in every rotating machinery systems. One of the commonly used bearing types is a ball bearing, which is under investigation in this paper. Modeling the dynamical behavior of a ball bearing includes several simultaneous contacts between the bearing components that make the accurate simulation of a ball bearing challenging and computationally heavy. The modeling and simulation provide accurate information of the dynamic performance of systems that contain ball bearings. However, depending on the complexity of the model, the computation time varies. It is possible to simulate ball bearings with excellent accuracy but then there is a need for more input parameters, including those that are not widely available.

The basic concept in ball bearings is that the balls rotate inside two steel rings (races) and the balls are kept separate with a cage. The design varies depending on the specific type of bearing but the basic concept is the same in every ball bearing.

Jones [1] presented a general theory for modeling an elastically constrained ball and radial roller bearing. The model considers five degrees of freedom of the inner ring and includes gyroscopic moments and centrifugal forces of the balls. The proposed model was verified later by Harris and Kotzalas [2] and Hamrock and Dowson [3] who generalized the proposed theory. The proposed model did not include any geometrical imperfections, which led to numerous studies considering the effects of different kinds of defects in the bearing. There is also a general trend that the earlier models considered fewer degrees of freedom than more recently proposed models when studying the effects of imperfections to the dynamical behavior of rotor-bearing systems.

Tandon and Choudhury [4] presented a thorough review for detecting defects in rolling element bearings. They classified bearing defects into two categories, distributed and localized. The defects caused by manufacturing error, improper installation or abrasive

* Corresponding author. Tel.: +358 50 569 5969; fax: +358 5621 2499.
E-mail addresses: emil.kurvinen@lut.fi (E. Kurvinen), jussi.sopanen@lut.fi (J. Sopanen), aki.mikkola@lut.fi (A. Mikkola).

http://dx.doi.org/10.1016/j.mechmachtheory.2015.03.017
0094-114X/

Nomenclature

Latin

c_d	diametral clearance
d	ball diameter
d_m	pitch diameter
d_s	bore diameter
d'_m	pitch diameter under loading
D	diameter
e	eccentricity
E'	effective modulus of elasticity
E	modulus of elasticity
f	conformity ratio
F	force
I_p	polar moment of inertia
j	number of ball
K_{con}	contact stiffness coefficient
k_e	approximated ellipticity parameter
L	distance (Fig. 6)
m	mass of the ball
n	number of balls
M_g	gyroscopic moment
r	Radius
R	curvature sum
R_d	curvature difference
R_x	effective radii of curvature in x-plane
R_y	effective radii of curvature in y-plane
T	moment

Greek

α	contact angle (improved model)
β	attitude angle (azimuth angle) (simplified model)
γ	misalignment
δ	deformation
ζ	second ellipticity integral
θ	angle between the shaft centerline and ball rotational axis
ξ	first ellipticity integral
λ	race control
ν	Poisson's ratio
ϕ	contact angle (simplified model)
ψ	angular location (improved model)
ω	rotation speed

Subscripts

a*y*	solid a, *y*-direction
a*x*	solid a, *x*-direction
B	ball
b*y*	solid b, *y*-direction
b*x*	solid b, *x*-direction
c	centrifugal
f	initial contact angle
h	housing
i/in	inner race
j	jth ball
o/out	outer race
s	shaft

x	axis x-direction
y	axis y-direction
z	axis z-direction

Superscripts

in	inner
out	outer
r	radial
t	axial
tot	total

wear are called distributed defects; those include surface roughness, waviness, misaligned races and off-size rolling elements. The defects caused by fatigue are called localized defects; those include cracks, pits and spalls on the rolling surfaces.

Aktürk et al. [5,6] proposed a three-degree-of-freedom ball bearing model where the effects of waviness, axial preload, and the number of balls were studied.

Jang and Jeong [7] proposed a five-degree-of-freedom model for a rigid rotor that is supported at least with two bearings. The model is used to study the waviness in races and balls. The results are verified with prior researchers. Further, Jang and Jeong [8] included the gyroscopic moment and centrifugal force of the balls in the model and studied the stiffness, contact force, displacement and vibration frequencies behavior with different waviness order in each bearing and validated the results with prior researchers. Jang and Jeong [9] studied the effect of different waviness order in the model that contains a pair of bearings and also the eccentricity of the center of mass of the rotor and bearing span center. The inertia forces were found to have a major effect when determining the bearing vibration frequencies.

Sopanen and Mikkola [10] presented a six-degree-of-freedom ball bearing model theory where the sixth degree of freedom is the friction torque around the rotational axis. The model considers waviness in the inner and outer races as well as the localized defects in the races. In the second part, Sopanen and Mikkola [11] investigated the clearance variation in the dynamical behavior, which was found to have a major effect. The low-order waviness generates vibrations at the frequencies at waviness order multiplied with rotation speed. They also concluded that when the waviness is near the number of balls, the vibrations occur near the ball passage frequencies in the races. The localized defects were found to generate frequencies at the bearing defect frequency. The results were verified with the results available in the literature. The model does not consider the centrifugal force and gyroscopic moment.

Changqing and Qinqyu [12] propose a model that has five degrees of freedom and considers both centrifugal force and gyroscopic moment. They studied a rotor bearing system under internal clearance, axial preload, radial load and waviness. The first three were found to have a significant role in systems stability, and the outer race waviness was found to have the most effect compared to inner race and ball waviness. Bai et al. [13] improved the proposed model and studied the axial preload effect on the ball bearings dynamical behavior. In the study, it was concluded that the unstable periodic solution of a balanced rotor can be avoided with the proper axial preload.

Recently, Nakhaeinejad and Bryant [14] proposed a model of rolling element bearings by using graphical vector bond method. The model consists of nine balls and two rings. The model includes centrifugal force and gyroscopic moment, contact elastic deflections and forces, contact slip, contact separation and defects on races. The model was verified with a test machine and by using the available solutions in the literature. However, the planar model does not consider the axial preload and its effect on the stiffness of the bearing. Xu et al. [15] studied a crankshaft mechanism where the revolute joint has been modeled as a ball bearing. The balls are modeled as individual parts. In the research, the clearance effect and number of balls influencing the load that an individual ball is having are studied. Xu et al. concluded that by having more balls, the load per individual part is decreased and the displacement is smaller compared to bearings that have fewer balls.

In conclusion, the research done in developing the ball bearing model can be categorized into two main fields: the ones which consider dynamical forces due to high rotation speed and the simplified ones that do not. The research done earlier usually does not consider the dynamical forces and the models developed more recently do. It is found that the ball bearing that is modeled using five degrees of freedom can be used to simulate the dynamical behavior under imperfections (due to manufacturing and installation) accurately. Friction force can also be added to the model, if the studied application has a special need for that (e.g., studying the touchdown bearing behavior when magnetic bearings fail). However, when considering several degrees of freedom and inertia forces, solving the model becomes computationally heavy to solve. Liew et al. [16] studied the effect of a two- and a five-degree-of-freedom bearing model with inertia and without. In the study, it was concluded that the five-degree-of-freedom model with inertia forces needs 10 times more time to solve than without the inertia forces.

The objective of this research is to improve the six-degree-of-freedom ball bearing proposed by Sopanen and Mikkola [10,11] by including the centrifugal force and gyroscopic moment to the model. As suggested by Kurvinen et al. [17] the models should be implemented into different structures with various sized bearings to discover more general behavior. The proposed models are utilized in the simulation of rotor dynamics in the simulation of three industrial applications, a high-speed electric motor (turbo blower), a high-speed machine and a high-speed generator. The applications are suited with a pair of different sized bearings: 70 mm, 55 mm

and 25 mm, respectively. The results obtained using the bearing models with and without ball inertia effects are compared and the justification for the inclusion of computationally expensive centrifugal force and gyroscopic moment effects is discussed. Finally, the results are used to determine at what rotation speed inertia forces can be neglected and at what speed they are necessary to consider.

2. Methods

The simplified model is based on the relative displacements and velocities between the inner and outer races. Displacements and velocities can be calculated by creating a geometrical relationship. Accordingly, the relationship between the force and deflection can be expressed. The model has five degrees of freedom: three translational and two rotational degrees of freedom. The model includes non-linear Hertzian contact deformation. The geometry and material parameters are given as input and the bearing forces and torques are solved. The simplified model does not consider high-speed forces.

The refined model is based on the force equilibrium between the external applied load and the internal load within the bearing. Rotation dependent forces, such as centrifugal force and gyroscopic moment of the ball are included. In the equilibrium condition, the deformation of the ball bearing is solved.

The ball bearing contains several parts including the cage that holds the balls in a fixed distance from the inner and outer races. The races connect the bearing to the shaft and housing. Each part should be considered in detail when creating an accurate mathematical model. However, the model should be computationally efficient and therefore the following general assumptions are made to decrease the degrees of freedom in the models:

1. Friction torque is neglected.
2. The effect of elastohydrodynamic film is neglected.
3. The defects and form error of the unit are neglected.

The friction torque and the effects of the hydrodynamic film are neglected in order to decrease model complexity. The effects of those additional parameters are assumed to have similar effects on both models. The defects and form error of the bearing are not included and they are assumed to be perfectly manufactured (i.e., the balls are round and races are circular.)

2.1. Ball bearing dynamic model without centrifugal and gyroscopic forces

The theory of modeling the deep-groove ball bearing is presented in detail in [10]. The modeling theory is briefly reviewed in this paper in order to provide a complete presentation. In this study, the ball bearing model without centrifugal and gyroscopic forces is called the “simplified model”.

2.1.1. Elliptical contact conjunction

The elliptical contact conjunction is used to determine the contact stiffness between the ball and races. In ball bearings, the ball and race are two solids that have different radii of curvature in two directions. Fig. 1 shows the contact geometry and the normal force, F, applied to two solids. The radius of contact conjunction is defined to be positive when the surface is convex and negative when concave.

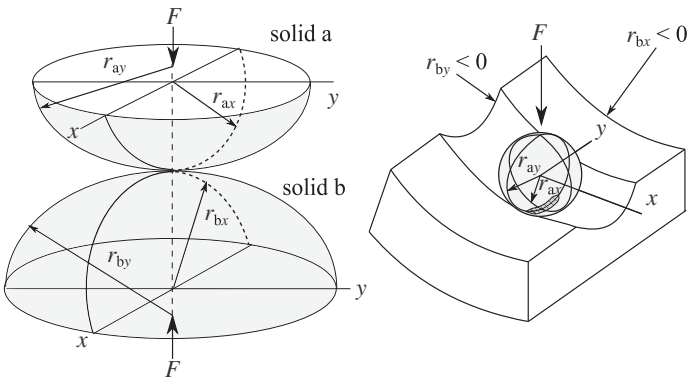

Fig. 1. Elliptical contact conjunctions.

The curvature sum, R, and curvature difference, R_d, that are used to define the contact deformation are calculated as

$$\begin{aligned}&\frac{1}{R}=\frac{1}{R_x}+\frac{1}{R_y}\\&R_d=R\left(\frac{1}{R_x}-\frac{1}{R_y}\right),\\&\text{where}\\&\frac{1}{R_x}=\frac{1}{r_{ax}}+\frac{1}{r_{bx}},\frac{1}{R_y}=\frac{1}{r_{ay}}+\frac{1}{r_{by}}\end{aligned}\tag{1}$$

where R_x and R_y represent the effective radii of curvature in the x and y planes. Subscripts ax, ay, bx and by refer to the radii in solids a and b in x- and y-directions, respectively. When the normal force is applied to the solids, the contact area is elliptical. The contact stiffness coefficient, K_{con}, for the elliptical contact conjunction can be calculated as

$$\begin{aligned}&K_{con}=\pi\widetilde{k}_e E'\sqrt{\frac{R\widetilde{\xi}}{4.5\widetilde{\zeta}^3}},\\&\text{where}\\&\widetilde{k}_e=1.0339\left(\frac{R_y}{R_x}\right)^{0.6360},\\&E'=\frac{2}{\frac{1-\nu_a^2}{E_a}+\frac{1-\nu_b^2}{E_b}},\\&\widetilde{\xi}=1.003+0.5968\left(\frac{R_y}{R_x}\right),\\&\widetilde{\zeta}=1.5277+0.6023ln\left(\frac{R_y}{R_x}\right).\end{aligned}\tag{2}$$

where $\widetilde{k}_e$ is the approximated ellipticity parameter, E' is the effective modulus of elasticity, ν is the Poisson's ratio, E is the material modulus of elasticity and subscripts a and b refer to solids that are in contact. Parameters ξ and $\widetilde{\zeta}$ are the approximation formulae for the first and second elliptical integrals [3].

2.1.2. Ball bearing geometry, total stiffness coefficient and displacements

The geometry of a deep groove ball bearing is shown in Fig. 2, where d is the ball diameter, r_{out} is the outer groove radius, r_{in} is the inner groove radius, c_d is the diametral clearance, D_h is the bearing housing diameter, d_m is the pitch diameter, d_s is the bore diameter, D_i is the inner raceway diameter, and D_o is the outer raceway diameter, respectively.

The relation between contact stiffness and deformation, δ_0, for a single ball is expressed as [3]

$$\delta_0=\left(\frac{F}{K_{con}}\right)^{2/3},\tag{3}$$

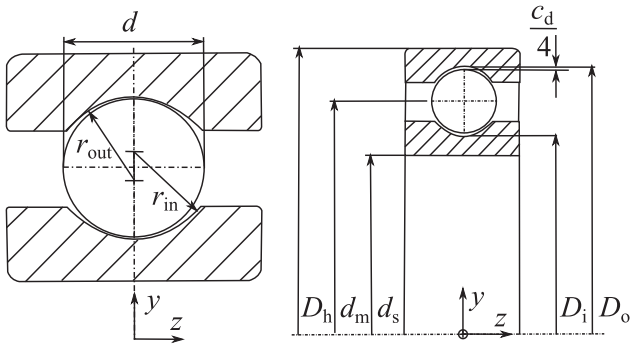

Fig. 2. Main dimensions of a ball bearing.

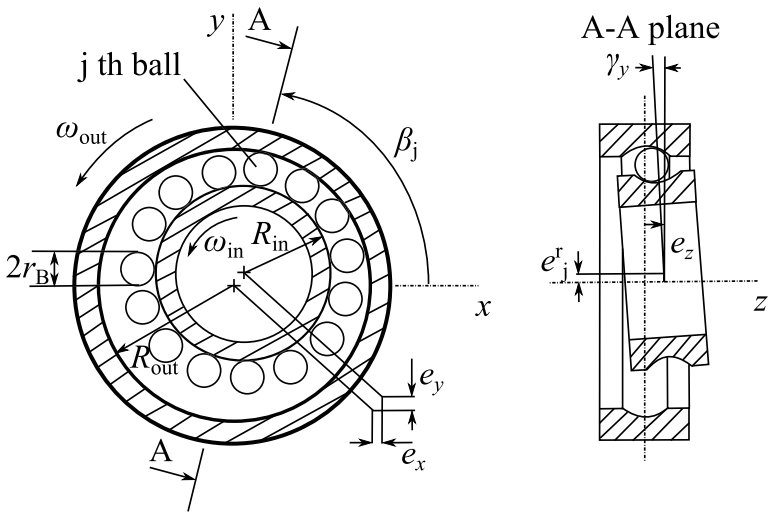

Fig. 3. Axial and transverse cross-section in the A–A plane of illustrative structure of a ball bearing.

where F is the normal load. The total stiffness of a single ball bearing involves the inner, K^{in}_{con}, and the outer ring, K^{out}_{con}, contact stiffness and that is expressed as [3]

$$K^{tot}_{con} = \frac{1}{\left(\left(\frac{1}{K^{in}_{con}}\right)^{2/3} + \left(\frac{1}{K^{out}_{con}}\right)^{2/3}\right)^{3/2}}. \tag{4}$$

2.1.3. Ball bearing forces and moments in the complete ball bearing

Ball bearing forces and moments are calculated from the relative displacements between the rings. Fig. 3 shows the layout for each ball and the relative displacements between the inner and outer rings.

Radial, e^r_j, and axial, e^t_j, displacements in ball j can be stated as

$$\begin{aligned} e^r_j &= e_x \cos\beta_j + e_y \sin\beta_j \\ e^t_j &= e_z - \left(-\gamma_x \sin\beta_j + \gamma_y \cos\beta_j\right)(R_{in} + r_{in}) \end{aligned} \tag{5}$$

where e_x, e_y, and e_z are the given relative displacements in x, y, and z directions, β_j is the attitude angle (azimuth angle) of ball j and γ_x and γ_y are the angular misalignments of the inner race about x and y axes. The attitude angle can be calculated for the jth ball as follows

$$\beta_j = \frac{2\pi(j-1)}{n}, \tag{6}$$

where n is the number of balls in the bearing [3]. The contact angle for ball j, ϕ_j, is depicted in Fig. 4.

The contact angle, ϕ_j, for ball j can be calculated as

$$\phi_j = \tan^{-1}\left(\frac{e^t_j}{R_{in} + r_{in} + e^r_j - R_{out} + r_{out}}\right). \tag{7}$$

The distance between the race surfaces along the line of contact, d_j, is then calculated as

$$d_j = r_{out} + r_{in} - \frac{R_{in} + r_{in} + e^r_j - R_{out} + r_{out}}{\cos\phi_j}. \tag{8}$$

The total elastic deformation can then be calculated as

$$\delta^{tot}_j = 2r_B - d_j. \tag{9}$$

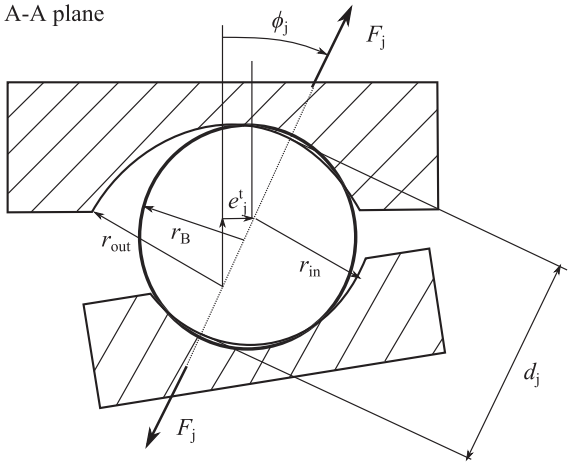

Fig. 4. Cross-section of a ball bearing in the A–A plane.

The contact force acting on ball j can be calculated for each ball as

$$F_j = K_{con}^{tot}\left(\delta_j^{tot}\right)^{3/2}, \tag{10}$$

where K_{con}^{tot} is the total stiffness coefficient determined by Eq. (4) [3]. The resultant bearing forces and moments in the shaft can be calculated in respect to the x, y and z directions as

$$\left.\begin{aligned} F_x &= -\sum_{j=1}^{n} F_j \cos\phi_j \cos\beta_j \\ F_y &= -\sum_{j=1}^{n} F_j \cos\phi_j \sin\beta_j \\ F_z &= -\sum_{j=1}^{n} F_j \sin\phi_j \\ T_x &= -\sum_{j=1}^{n} F_j (R_{in}+r) \sin\phi_j \sin\beta_j \\ T_y &= -\sum_{j=1}^{n} F_j (R_{in}+r) \sin\phi_j \left(-\cos\beta_j\right) \end{aligned}\right\}. \tag{11}$$

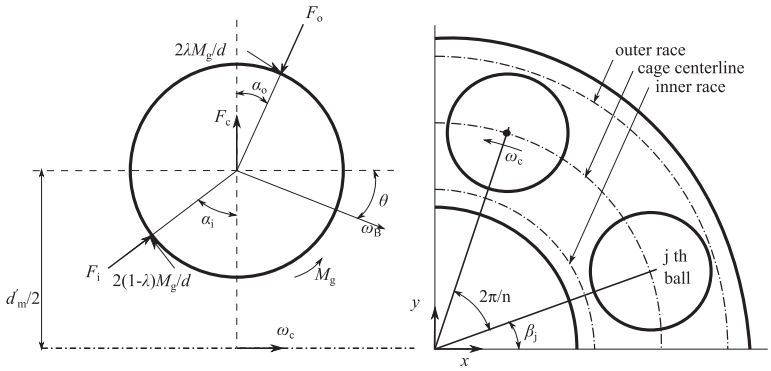

Fig. 5. Forces and moments acting on the ball on high-speed operation.

It should be noted that in summations in Eq. (10) only the force components where compression exists between the races and ball are included (i.e., $\delta_j^{tot} > 0$).

2.2. Ball bearing dynamic model with centrifugal and gyroscopic forces

In high-speed operations, the contact angles in the inner and outer race contacts are no longer identical. This will have a noticeable effect on the ball bearings' dynamic behavior in high-speed. In this study, the ball bearing model with centrifugal and gyroscopic forces is called the "improved model". Fig. 5 shows the forces and contact angles within a single ball and the position of the jth ball in the bearing. The ball is subjected to the centrifugal force, F_c, and the contact forces on the inner and outer races, F_i and F_o. In addition, a gyroscopic moment, M_g, and counter friction forces are affecting the ball deformation. The force equilibrium for a single ball can be calculated when the contact angles are known in the inner and outer races α_i and α_o, respectively. Notation λ represent the race control and it has a value of 0 when inner-race control is valid or 1 when outer-race control is valid.

In the case of a substantial centrifugal force, the contact angles in the inner and outer race contacts are different. Pitch diameter under loading, d'_m, can be expressed as a function of nominal pitch diameter d_m, L_4 distance (Fig. 6), ball diameter d, outer race conformity ratio, f_o, and initial contact angle, α_f, and calculated as

$$d'_m = d_m + 2L_4 - 2d(f_o - 0.5)\cos\alpha_f. \tag{12}$$

The initial contact angle can be calculated from the diametral clearance, c_d, ball diameter, d, and outer and inner conformity ratios, f_o and f_i, as

$$\alpha_f = \cos^{-1}\left(1 - \frac{c_d}{2d(f_o + f_i - 1)}\right). \tag{13}$$

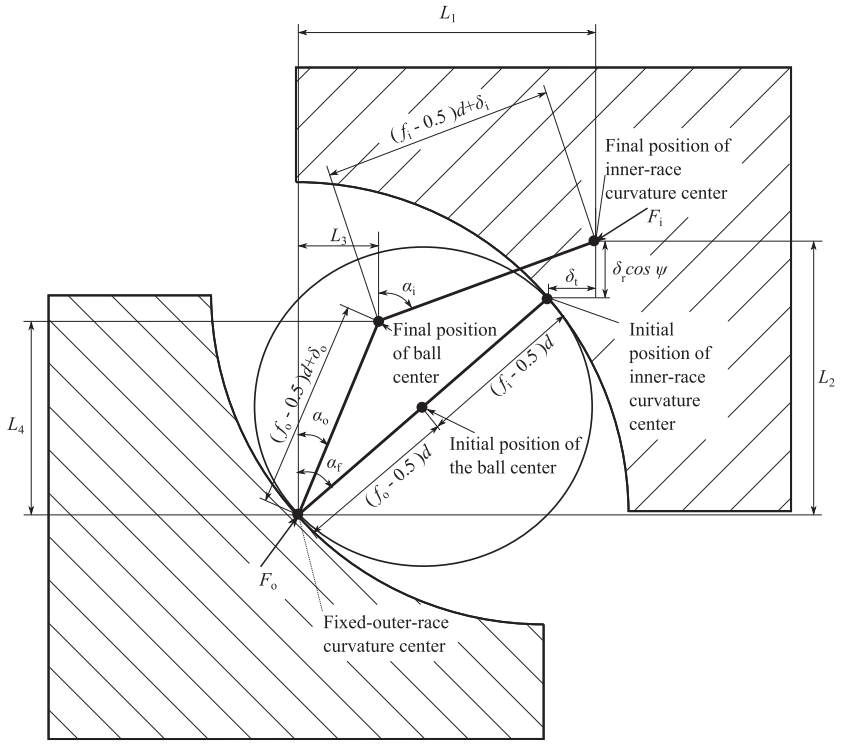

Fig. 6. Deflection of the center of ball and curvature races at angular location ψ [3].

The angle between ball rotational axis and bearing centerline, θ, can be calculated as

$$\theta = \tan^{-1}\left(\frac{d'_m \sin\alpha_{o/i}}{d'_m \cos\alpha_{o/i} \pm d}\right) \tag{14}$$

for the outer-race control the contact angle α_o is used and in the nominator the diameter is added and for the inner-race control contact angle α_i is used and in the nominator the diameter is subtracted [3].

Fig. 6 shows the initial and final (loaded) positions of the ball and inner race curvature center.

Based on Fig. 6 the following geometric relation for each ball can be expressed using the Pythagorean theorem as

$$\begin{aligned} &L_4^2 + L_3^2 - [(f_o - 0.5)d + \delta_o]^2 = 0 \\ &(L_2 - L_4)^2 + (L_1 - L_3)^2 - [(f_i - 0.5)d + \delta_i]^2 = 0, \end{aligned} \tag{15}$$

where f_i and f_o are the inner and the outer race conformity ratio that is a measure of the geometrical conformity of the race and the ball in a plane that passes through the center of the bearing and is transverse to the race (shown in Fig. 2). Forces applied to the ball are shown in Fig. 5, and these can be calculated when the total elastic deformation in the inner and outer race contacts and the stiffness coefficients are known as [3]

$$\begin{aligned} F_o &= K_o \delta_o^{3/2} \\ F_i &= K_i \delta_i^{3/2}. \end{aligned} \tag{16}$$

The equilibrium condition for each ball can be expressed with the help of Newton's second law as

$$\begin{aligned} &F_o \sin\alpha_o - F_i \sin\alpha_i - \frac{2M_g}{d}(\lambda \cos\alpha_o - (1-\lambda)\cos\alpha_i) = 0 \\ &F_o \cos\alpha_o - F_i \cos\alpha_i + \frac{2M_g}{d}(\lambda \sin\alpha_o - (1-\lambda)\sin\alpha_i) - F_c = 0, \end{aligned} \tag{17}$$

where λ has a value of 1 in the case of outer-race control and 0 when inner-race control is applied. The race control theory was proposed by Jones [1], where λ is a calculated parameter to define the race in which no slipping occurs. The required torques to spin the ball against the inner and outer races are evaluated. A race, which requires more torque to spin, defines the race control, (i.e., if λ is 1 the outer-race control exists), and when λ is 0 then the inner race contact exists. In Eq. (17) the centrifugal force can be expressed as

$$F_c = \frac{1}{2} m d'_m \omega_c^2, \tag{18}$$

where m is mass of the ball, d'_m is the pitch diameter under loading and ω_c is the angular velocity of the cage. The gyroscopic moment of the ball can be calculated as

$$M_g = I_p \omega_B \omega_c \sin\theta, \tag{19}$$

where I_p is the mass moment of inertia of the ball, ω_B is the angular velocity of the ball about its rotation axis, ω_c is the angular velocity of the cage and θ is the angle between the shaft center line and ball rotational axis. Eq. (17) can be re-expressed as

$$\begin{aligned} &\frac{K_o \delta_o^{3/2} L_3}{d(f_o - 0.5) + \delta_o} - \frac{K_i \delta_i^{3/2}(D\sin\alpha_f + \delta_t - L_3)}{d(f_i - 0.5) + \delta_i} \\ &- \frac{2}{d} I_p \omega_B \omega_c \sin\theta \left(\frac{\lambda L_4}{d(f_o - 0.5) + \delta_o} - \frac{(1-\lambda)(D\cos\alpha_f + \delta_r \cos\psi - L_4)}{d(f_i - 0.5) + \delta_i}\right) = 0, \\ &\frac{K_o \delta_o^{3/2} L_4}{d(f_o - 0.5) + \delta_o} - \frac{K_i \delta_i^{3/2}(D\cos\alpha_f + \delta_r \cos\psi - L_4)}{d(f_i - 0.5) + \delta_i} \\ &+ \frac{2}{d} I_p \omega_B \omega_c \sin\theta \left(\frac{\lambda L_3}{d(f_o - 0.5) + \delta_i} - \frac{(1-\lambda)(D\sin\alpha_f + \delta_t - L_3)}{d(f_i - 0.5) + \delta_i}\right) \\ &- \frac{m\omega_c^2}{2}(d_e + 2L_4 - 2(f_o - 0.5)d\cos\alpha_f) = 0. \end{aligned} \tag{20}$$

The iterative solution is required due to the nonlinear equations and the Newton–Raphson method is utilized to solve the four equations in Eqs. (15) and (20). The unknown variables to solve are L_3, L_4, δ_i and δ_o. Good assumptions for tangential and

radial displacement, δ_t and δ_r, can be made by using a condition of equilibrium applied to the complete ball bearing as follows

$$\begin{aligned} F_t - \sum_{k=1}^{n}\left[F_{kj}\sin\alpha_{kj} - \frac{2\left(1-\lambda_j\right)M_{gj}}{d}\cos\alpha_{kj}\right] &= 0, \\ F_r - \sum_{k=1}^{n}\left[F_{kj}\cos\alpha_{kj} - \frac{2\left(1-\lambda_j\right)M_{gj}}{d}\sin\alpha_{kj}\right]\cos\psi_j &= 0, \end{aligned} \tag{21}$$

where F_t is the axial load and F_r is the radial load [3].

3. Case studies and results

The two developed models are implemented into a three different sized rotors. In size order from largest to smallest the studied cases are a solid rotor blower (turbo blower), a high-speed machine and a high-speed generator. The turbo blower is supported with two 6014 hybrid deep-groove ball bearings, the machine with two 71911 CE/HCP4A high precision ball bearings and the generator with two S7005 CE/HCP4A high precision angular contact ball bearings. The turbo blower rotor's geometry is similar to that presented earlier in Pyrhönen et al. [18]. However, in this study, the constant bearing stiffness used in the earlier work have been replaced by stiffnesses obtained using the developed ball bearing models. The structures for the high-speed machine and high-speed generator are presented in the following sections. In the studied cases inner race bearing stiffness coefficients, critical speed maps and Campbell diagrams are studied.

3.1. Turbo blower structure

The main layout and dimensions of the turbo blower are shown in Fig. 7 while the parameters used in the analysis are shown in Table 1.

The turbo blower is supported with two SKF 6014/HC2 deep-groove ball bearings and those are located in nodes 4 and 19 (Fig. 7). The main bearing dimension and parameters are shown in the Table 2.

Both bearings are loaded with a 300 axial load and a 700 radial load (z-direction). The bearing support is considered to be rigid. The initial guess for the radial displacement, δ_r, is 70 μm and for the axial direction, δ_t, is 10 μm. Using Eqs. (15) and (20) the initial deformations δ_i and δ_o and initial distances L_3 and L_4 can be obtained.

3.2. High-speed machine structure

The main layout and dimensions of the high-speed machine are shown in Fig. 8 while the parameters used in the analysis are shown in Table 3.

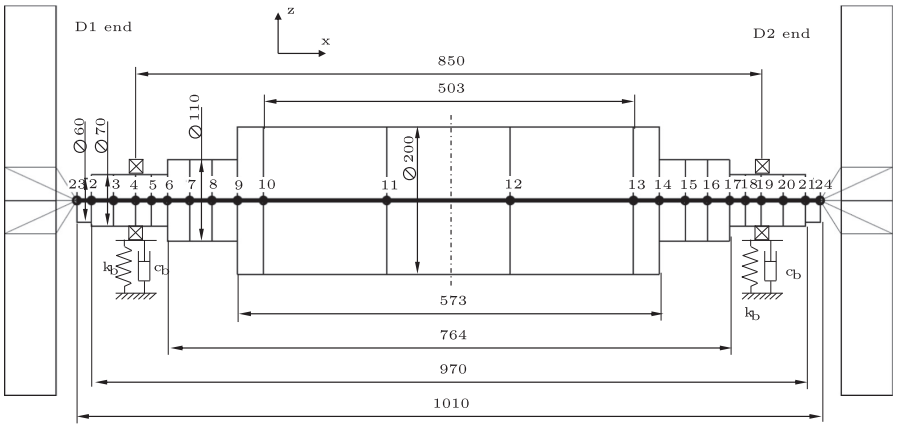

Fig. 7. Layout and finite element discretization of the turbo blower with two impellers. The dimensions are in millimeters. The slitted part of the rotor is between nodes 10 and 13.

Table 1
Parameters used in the turbo blower analysis.

Young's modulus	210 GPa
Material density	7800 $\frac{kg}{m^3}$
Poisson's ratio (rotor)	0.3
Properties of the slitted part	
Area	0.0251 m^2
Second moment of area	6.2832×10^{-5} m^4
Impeller mass properties	
Mass	19.0 kg
Polar mass moment of inertia	0.5 kg m^2
Diametral mass moment of inertia	0.3 kg m^2
Stiffness of impeller attachment	
Translational	1.0×10^{11} $\frac{N}{m}$
Rotational	1.5×10^{6} $\frac{Nm}{rad}$
Rotor unbalance masses	
D1 impeller (node 23)	36 g mm @ 270°
D1 rotor end (node 9)	50 g mm @ 0°
D2 rotor end (node 14)	50 g mm @ 0°
D2 impeller (node 24)	50 g mm @ 90°
Total mass of the rotor	174.85 kg

Table 2
Dimensions of the 6014/HC type deep-groove hybrid ball bearing.

Bore diameter	d_s	70 mm
Outer diameter	D	110 mm
Width	W	20 mm
Pitch diameter	d_m	89.85 mm
Ball diameter	d	11.91 mm
Number of balls	n	14
Diametral clearance	c_d	5.5 μm
Bearing damping coefficient	c_b	0.55 $\frac{Ns}{mm}$
Inner and outer race conformity	R_i, R_o	0.52
Static load rating	C_0	31,000 N
Modulus of elasticity (races)	E_r	207 GPa
Poisson's ratio (races)	ν_r	0.3
Modulus of elasticity (balls)	E_b	315 GPa
Density (balls)	ρ_b	3200 $\frac{kg}{m^3}$
Poisson's (balls)	ν_b	0.26
Reference speed	n_{max}	16,000 rpm
Misalignment	γ_y	0°

The high-speed machine is supported with two 71911 CE/HCP4A angular contact ball bearings. The bearings are located at nodes 9 and 25 (Fig. 8). The main bearing dimension and parameters are shown in Table 4.

Both bearings are loaded with a 800 N axial load and a 90 N radial load (z-direction). The bearing support is considered to be rigid. The initial guess for the radial displacement, δ_r, is 50 μm and for the axial direction, δ_t, is 10 μm. Using Eqs. (15) and (20) the initial deformations δ_i and δ_o and initial distances L_3 and L_4 can be obtained.

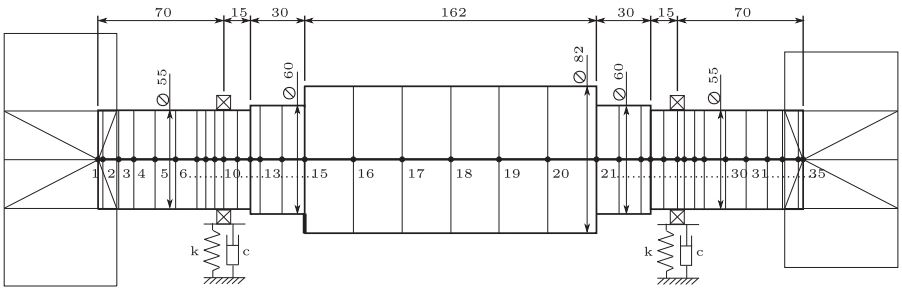

Fig. 8. Layout and finite element discretization of the high-speed machine. The dimensions are in millimeters. The impellers are located at nodes 1 and 35.

Table 3
High-speed machine parameters used in the analysis.

Young's modulus (rotor)	210 GPa
Material density (rotor)	7800 $\frac{kg}{m^3}$
Poisson's ratio (rotor)	0.3
Impeller mass properties	
Mass (node 1)	6.0 kg
Polar mass moment of inertia	0.055 kg m^2
Diametral mass moment of inertia	0.031 kg m^2
Mass (node 35)	5.1 kg
Polar mass moment of inertia	0.028 kg m^2
Diametral mass moment of inertia	0.017 kg m^2
Rotor unbalance masses	
Rotor (node 15 and 21)	0.681 g mm @ 0°
Machine (node 1)	0.165 g mm @ 0°
Machine (node 35)	0.135 g mm @ 0°
Total mass of the rotor	26.0 kg

Table 4
Dimensions of the 71911 CE/HCP4A angular contact ball bearing.

Bore diameter	d_s	55 mm
Outer diameter	D	80 mm
Width	W	13 mm
Pitch diameter	d_m	67.538 mm
Ball diameter	d	7.938 mm
Number of balls	n	21
Diametral clearance	c_d	5.5
Inner and outer race conformity	R_i, R_o	0.52 μm
Static load rating	C_0	10,600 N
Modulus of elasticity (races)	E_r	207 GPa
Poisson's ratio (races)	v_r	0.3
Modulus of elasticity (balls)	E_b	315 GPa
Density (balls)	ρ_b	3200 $\frac{kg}{m^3}$
Poisson's (balls)	v_b	0.26
Reference speed	n_{max}	43,000 rpm
Misalignment	γ_y	0

3.3. High-speed generator structure

The main layout and dimensions of the high-speed generator are shown in Fig. 9 while the parameters used in the analysis are shown in Table 5.

The high-speed generator is supported with two S7005 CE/HCP4A angular contact ball bearing. The bearings are located at nodes 9 and 38 (Fig. 9). The main bearing dimension and parameters are shown in Table 6.

Both bearings are loaded with a 265 N axial load and a 20 N radial load (z-direction). The bearing support is considered to be rigid. The initial guess for the radial displacement, δ_r, is 50 μm and for the axial direction, δ_t, is 10 μm. Using Eqs. (15) and (20) the initial deformations δ_i and δ_o and initial distances L_3 and L_4 can be obtained.

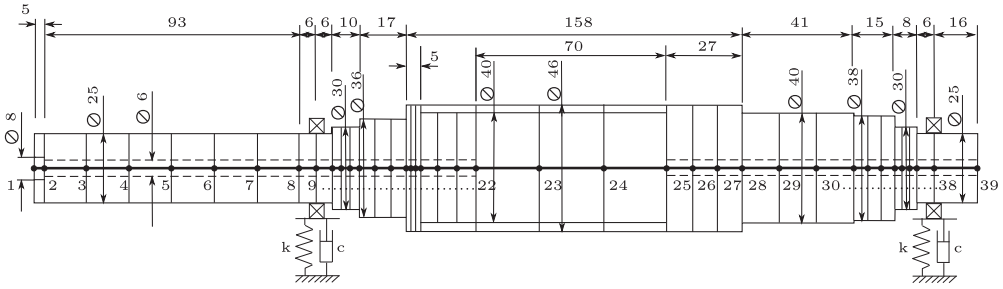

Fig. 9. Layout and finite element discretization of the high-speed generator. A permanent magnet is located between nodes 22 and 25. The dimensions are in millimeters.

Table 5
Parameters used in the high-speed generator analysis.

Young's modulus (rotor)	210 GPa
Material density (rotor)	7800 $\frac{kg}{m^3}$
Poisson's ratio (rotor)	0.3
Young's modulus (PM)	150 GPa
Material density (PM)	8400 $\frac{kg}{m^3}$
Poisson's ratio (PM)	0.3
Rotor unbalance masses	
Rotor end (node 1)	0.485 g mm @ 0°
Permanent magnet (node 22)	0.148 g mm @ −90°
Total mass of the rotor	2.5 kg

Table 6
Dimensions of the S7005 CE/HCP4A angular contact ball bearing.

Bore diameter	d_s	25 mm
Outer diameter	D	47 mm
Width	W	12 mm
Pitch diameter	d_m	35.15 mm
Ball diameter	d	6.35 mm
Number of balls	n	14
Diametral clearance	c_d	5.5 μm
Inner and outer race conformity	R_i, R_o	0.52
Static load rating	C_0	4150 N
Modulus of elasticity (races)	E_r	207 GPa
Poisson's ratio (races)	v_r	0.3
Modulus of elasticity (balls)	E_b	315 GPa
Density (balls)	ρ_b	3200 $\frac{kg}{m^3}$
Poisson's (balls)	v_b	0.26
Reference speed	n_{max}	56,000 rpm
Misalignment	γ_y	0°

3.4. Results of the simulations

Two bearing models were implemented into three different size rotor models. An analysis was performed using a custom in-house code in Matlab software. The rotor is modeled by finite element method (FEM) [19] and the used element type is the Timoshenko beam element [20]. The stiffness of the bearing inner race, critical speed maps and Campbell diagrams are studied.

3.4.1. Ball bearing stiffness coefficients

In the simplified ball bearing model, the bearing stiffness coefficient does not depend on the rotation speed. On the contrary, in a high-speed bearing model, the bearing stiffnesses are strongly dependent of the rotation speed. The diagonal stiffness values for the simplified bearing model in the translational direction are shown in the Table 7.

In the turbo blower model, the bearing is designed for a maximum rotation speed of 16,000 rpm which was also kept as the maximum value for the stiffness calculation. The high-speed machine bearings were designed for a maximum of 43,000 rpm and the stiffness was studied to 45,000 rpm. The smallest, high-speed generator bearings were designed for the maximum rotation speed of 56,000 rpm. The generator bearing stiffness values were studied up to 70,000 rpm. The stiffness values as a function of rotation speed with the improved bearing model are shown in Fig. 10 for the turbo blower (a), Fig. 11 for the high-speed machine (b) and Fig. 12 for the high-speed generator (c). In these figures, the stiffness calculated with the simplified bearing model is also included.

The stiffness coefficient in the blower decreases rapidly if the rotation speed is above 2000 rpm and at the maximum rotation speed, the axial stiffness decreases by a total of 18.0%, the radial direction in y-direction by 27.0% and the z-direction by 30.0% (i.e. direction of the applied force) from the initial stiffness coefficient.

Table 7
Axial and radial stiffnesses with the simplified bearing model.

Model	Axial stiffness $x(\frac{N}{m})$	Radial stiffness $y(\frac{N}{m})$	Radial stiffness $z(\frac{N}{m})$
Turbo blower	2.021×10^7	2.8445×10^8	2.7784×10^8
High-speed machine	5.628×10^7	4.0941×10^8	4.0958×10^8
High-speed generator	2.648×10^7	2.0158×10^8	2.0158×10^8

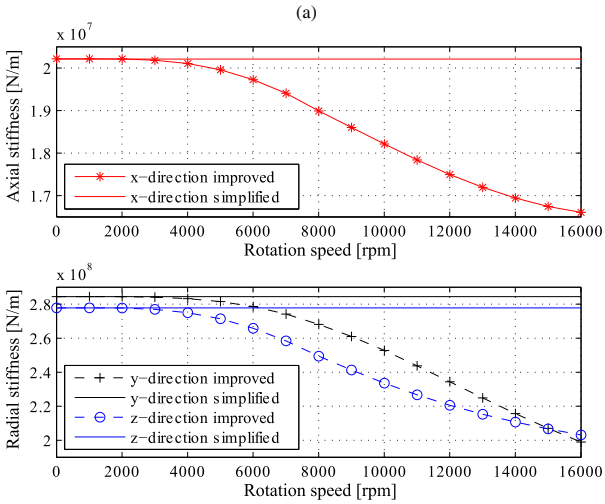

Fig. 10. Bearing stiffnesses in the axial and radial directions as a function of rotation speed in turbo blower (0–16,000 rpm).

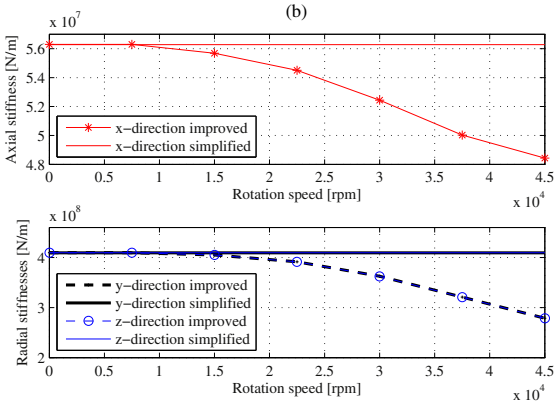

Fig. 11. Bearing stiffnesses in the axial and radial directions as a function of rotation speed of a high-speed machine (0–45,000 rpm).

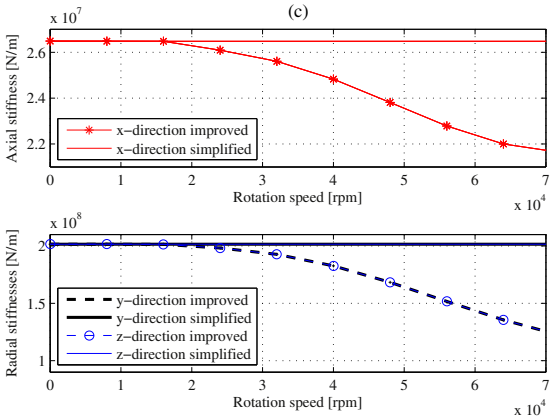

Fig. 12. Bearing stiffnesses in the axial and radial directions as a function of the rotation speed of a high-speed generator (0–70,000 rpm).

Table 8
Limiting rotation speeds when the stiffness starts to decrease.

Model	Constant stiffness (rpm)	Bearing maximum rotation speed (rpm)	Percentage from the designed maximum
Turbo blower	0–2000	16,000	12.5
High-speed machine	0–7500	43,000	17.4
High-speed generator	0–16,000	56,000	28.6

The stiffness coefficient in the high-speed machine decreases in the axial direction by 14.0% and in the radial directions by 31.9% from the original value to the value at 45,000 rpm.

In the high-speed generator the axial stiffness decreases by 18.3% and the radial stiffness by 39.4% when comparing the stiffness value in the zero rotation speed and in the maximum calculated speed 70,000 rpm.

In the studied cases, the stiffness decreases as the rotation speed increases and that is caused by the centrifugal force and gyroscopic moment affecting the ball. Based on Table 7 and Figs. 10, 11 and 12, it can be concluded that, at low rotation speeds, the stiffness coefficients are in good agreement between the two models. In the studied cases, when the stiffness begins to decrease a clear variation is visible. For the first case, a, when the rotor rotation speed is below 2000 rpm the stiffness is constant. For the second case, b, when the rotor rotation speed is below 7500 rpm the stiffness is constant. For the third case, c, when the rotor rotation speed is below 16,000 rpm the stiffness is constant. The rotation speeds and the velocity range when the stiffness is constant are shown in Table 8. The maximum rotation speed for each bearing is given by the manufacturer.

Based on these three cases, the range where the stiffness is constant shows a linear relationship with the bore diameter. The relationship shows that the smaller the bearing, the higher percentage from the maximum rotation speed the bearing can be rotated before the stiffness decreases due to the centrifugal force and gyroscopic moment affecting the balls.

3.5. Critical speed maps

In the critical speed map, the effect of support stiffness on the critical speeds is shown. From this, it can be seen how increasing the bearing stiffness affects the critical speeds. At low stiffness, the support stiffness (bearings) primarily defines the critical speeds. Once the support stiffness increases enough, the critical speeds reach a constant value (i.e. increasing the bearing stiffness has no effect on the critical speed). Above this point, the rotor flexibility defines the critical speeds. [21]

a) Turbo blower In the critical speed map, the general relation between the support stiffness and the system can be seen. Fig. 13 shows the critical speed map where the radial bearing stiffness (y- and z-directions) varies. The axial (x) stiffness coefficient is set to zero. Critical speed maps are plotted on the zero rotational velocity for an unconstrained system. In the turbo blower, three first modes are shown.
The first two modes have an inclining section when the bearing stiffness increases above $2.0 \times 10^8 \frac{N}{m}$. Below this value, the bearing stiffness mainly determines the critical speeds of the rotor system. Correspondingly, for bearing stiffnesses higher than $2.0 \times 10^8 \frac{N}{m}$, the flexibility of the rotor has a more significant influence on the critical speeds. In this case, the variation of bearing stiffness will have an effect on the third mode but not on the first two modes.

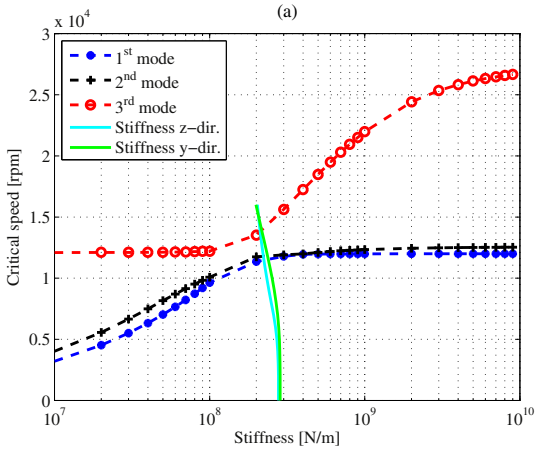

Fig. 13. Undamped critical speed map. The radial stiffness is varied at zero velocity.

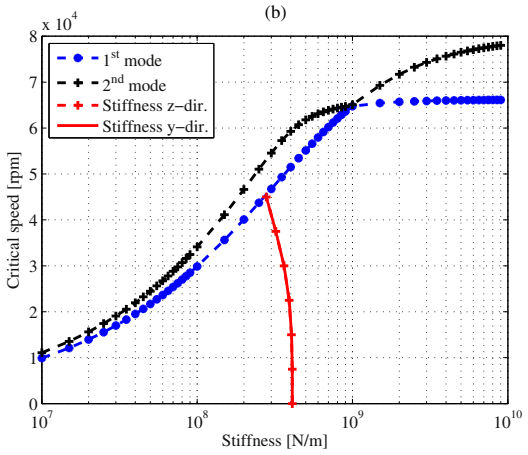

Fig. 14. Critical speed map of a high-speed machine.

b) High-speed machine Fig. 14 shows the critical speed map of the high-speed machine, where the radial bearing stiffness (y- and z-directions) varies and the first two modes are shown.
The two first modes have an inclining section when the bearing stiffness increases above $1.0 \times 10^9 \frac{N}{m}$. Below this value, the bearing stiffness mainly determines the critical speed of the rotor system. Correspondingly, for bearing stiffnesses higher than $1.0 \times 10^9 \frac{N}{m}$, the flexibility of the rotor has a more significant influence on the critical speeds. In this case, the bearing stiffness variation will have an effect on both modes.

c) High-speed generator Fig. 15 shows the critical speed map of the high-speed generator, where the radial bearing stiffness (y- and z-directions) varies and the two first modes are shown.
The two first modes have an inclining section when the bearing stiffness increases above $1.0 \times 10^8 \frac{N}{m}$. Below this value, the bearing stiffness mainly determines the critical speed of the rotor system. Correspondingly, for bearing stiffnesses higher than $1.0 \times 10^8 \frac{N}{m}$, the flexibility of the rotor has a more significant influence on the critical speeds. In this case, the variation of bearing stiffness will lower the critical speeds so that the second mode will decrease more than the first mode.

3.5.1. Campbell diagrams

a) Turbo blower In a Campbell diagram, the natural frequencies of the rotor-bearing systems are shown as a function of rotation speed. The critical speeds are found from the diagram. The Campbell diagrams for the turbo blower with two bearing models are shown in Fig. 16.

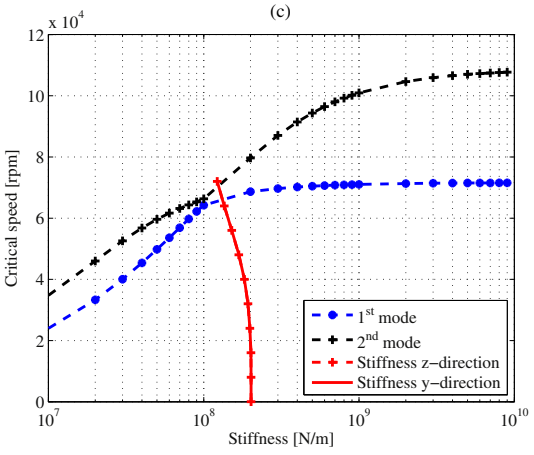

Fig. 15. Critical speed map of a high-speed generator.

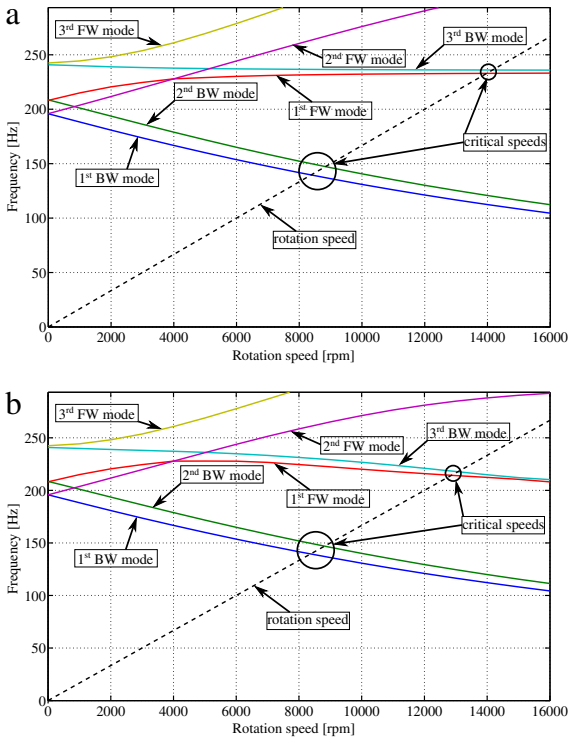

Fig. 16. Campbell diagrams of the turbo blower: a) simplified bearing model and b) improved bearing model.

It can be seen in Fig. 16 that the Campbell diagrams are identical up to 6000 rpm rotation speeds and as the rotation speed increases, the whirling frequencies start to differ. The first two critical speeds occur approximately at the same rotation speed in both bearing models. The third and fourth critical speeds occur in the improved bearing model at a lower rotation speed than in the simplified bearing model. The first critical speed is a backward whirling mode, the second is also a backward whirling mode, the third is a forward whirling mode and the fourth is a backward whirling mode (see Fig. 16; a comparison of the critical speeds in the two bearing models is shown in Table 9).

The first two critical speeds occur close to each other and there is no clear difference between the models used to study this case. A clear difference can be seen at the third and fourth critical speeds. The critical speeds in the case of a high-speed ball bearing model are over 8% lower than with the simplified bearing model. The obtained results are in agreement with the critical speed map (Fig. 13) where the first and second critical speeds are not affected by the different bearing stiffnesses as the third and fourth critical speeds are.

b) High-speed machine

The Campbell diagrams with the simplified and improved bearing models for the high-speed machine are shown in Fig. 17.

It can be seen in Fig. 17 that the Campbell diagrams are in good agreement up to 15,000 rpm and as the rotation speed increases, the whirling frequencies start to differ. When the rotation speeds are faster than

Table 9
Turbo blower critical rotation speed from the Campbell diagram.

#	Critical speed (rpm)		
	Simplified model	Improved model	Difference [%]
1	8378	8372	0.07
2	8836	8816	0.23
3	13,977	12,861	8.68
4	14,160	13,065	8.38

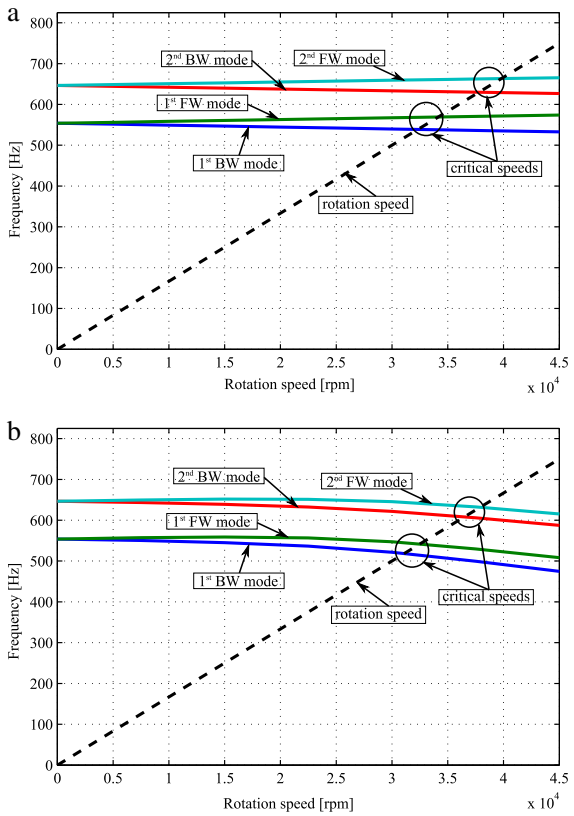

Fig. 17. Campbell diagrams of the high-speed machine: a) simplified bearing model and b) improved bearing model.

15,000 rpm, the whirling frequencies in the improved model are lower compared to the simplified model. With the high-speed machine, the differences in all the first four critical speeds are similar in magnitude. The faster the machine rotates, the bigger the difference between the two models is. The first critical speed is a backward whirling mode, the second is a forward whirling mode, the third is a backward whirling mode and the fourth is a forward whirling mode (see Fig. 17). A comparison of the critical speeds in the two bearing models is shown in Table 10.

The critical speeds in the improved ball bearing model are from 3% to almost 5% lower than with the simplified bearing model. The difference is the same magnitude with all the first four critical speeds. It can also be seen from the critical speed map (Fig. 14) why the four first critical speeds have approximately a similar effect on the bearing stiffness.

c) High-speed generator

The Campbell diagrams for the high-speed generator are shown in Fig. 18. The Campbell diagram with the simplified model is calculated up to 90,000 rpm in order to show the third and fourth critical speeds.

It can be seen in Fig. 18 that at rotation speeds up to 16,000 rpm, the Campbell diagrams are identical, and as the rotation speed increases, the whirling frequencies start to differ. The first two critical speeds occur

Table 10
Critical rotations speed in high-speed machine from the Campbell diagram.

#	Critical speed (rpm)		
	Simplified model	Improved model	Difference [%]
1	32,324	31,093	3.80
2	34,155	32,480	4.90
3	37,796	36,483	3.50
4	39,798	37,910	4.70

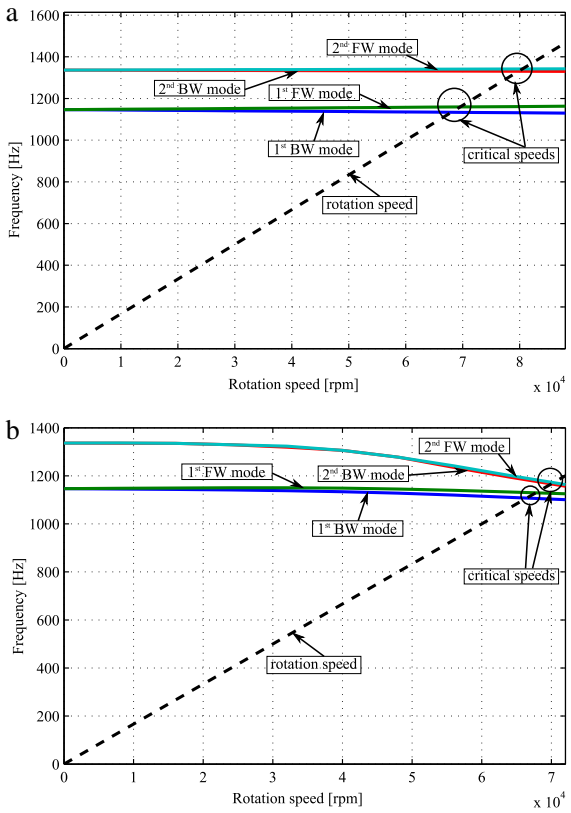

Fig. 18. Campbell diagrams of the high-speed generator: a) simplified bearing model and b) improved bearing model.

approximately at the same rotation speed and the third and fourth critical speeds occur at a lower rotation speed than in the simplified bearing model. The first critical speed is a backward whirling mode, the second is a forward whirling mode, the third is a backward whirling mode and the fourth is a forward whirling mode. A comparison of the critical speeds in the two models is shown in Table 11.

The two first critical speeds occur close to each other and there is over 2% difference between the models used to study this case. A clearer difference can be seen in the third and fourth critical speeds. The critical speeds in the case of a high-speed ball bearing model are over 12% lower than with the simplified bearing model. The critical speed map (Fig. 15) clearly explains why the first and second critical speeds are not affected by the different bearing stiffnesses as the third and fourth critical speeds are.

4. Discussion

In the case of ball bearings, an increase in model complexity leads to an increased number of input parameters and initial guesses that are crucial for successful simulation. The theoretical background for modeling ball bearings, including the centrifugal and

Table 11
Critical rotations speed from the Campbell diagram.

#	Critical speed (rpm)		
	Simplified model	Improved model	Difference [%]
1	68,026	66,438	2.33
2	69,568	67,756	2.60
3	79,853[a]	69,981	12.36
4	80,501[a]	70,300	12.67

[a] Occurs over the speed range.

gyroscopic forces, has been available since 1960. Nevertheless, it is still unclear under which conditions (e.g. size of the rotor or rotation speed range) an obligation to use or not use the model including the high speed effects exists.

The studied cases show that the bearing stiffness coefficients are in agreement with the simplified and improved model at low rotation speeds. In fact, the results show that in the improved bearing model, the bearing coefficients are almost constant up to a certain rotation speed. When the stiffness is constant, then there are no real benefits of using the improved ball bearing model. The largest case with the biggest bearing bore diameter, the turbo blower, concludes that it can be rotated up to 2000 rpm with the simplified bearing model having zero difference to the improved model. The second largest case with the medium-sized bore diameter, the high-speed machine, concludes that it can be rotated up to 7500 rpm having zero difference to the improved model. The smallest case, the high-speed generator, with the smallest bore diameter concludes that it can be rotated up to 16,000 rpm having zero difference to the improved model. It should be noted that in ball bearing modeling, there are several parameters and factors to be considered and the relationship shown in this paper is only valid with the studied cases.

In the literature, it is stated that for low and moderate speeds that the centrifugal and gyroscopic forces can be ignored and at high speeds, it is obligatory to consider them. For the studied rotors and with the used bearing types, the results are in agreement with the general statement in the literature. It should be noted that the results might vary even with the same structure when, for example, the clearance or bearing loading is varied. Due to this, common rules for the studied structures cannot be suggested.

In all the cases the stiffness decreased when the rotation speed increased. Similar results are shown in the study by Butner et al. [22].

The critical speed map shows that the stiffness variation in the high speed bearing model does not decrease the stiffness sufficiently for it to have an influence on the first two critical speeds. The difference between the third and fourth critical speeds can also be seen in the critical speed map. As the bearing stiffness decreases, the critical speeds also decrease.

In the Campbell diagram, in the improved bearing model, the critical frequencies decrease as the rotation speed increases. The difference in the Campbell diagram calculations shows behavior similar to that which was presented in an early study by Cao and Altintas [23]. From the critical speed map at zero velocity, similar behavior can also be seen. Depending on which location the bearing stiffness is in on the critical speed map (i.e. are the bearing stiffness defining the critical speeds or the rotor itself), the decrease in the critical speed varies in the studied cases.

The appropriate bearing model selection can be a subject of argument. The stiffness values for the studied rotors from both models (Figs. 10, 11 and 12) show that if the values obtained with the improved model are close to the values obtained from the simplified model then the simplified model is justified. As the stiffness values diverge from the simplified model results when the speed is increased then the critical speed map should be plotted. A sensitivity analysis of the rotor critical speeds due to bearing stiffness variation should then be investigated. If the critical speeds are sensitive then the improved model should be used and the Campbell diagram should be plotted to see the detailed effects. Then the safety margin from the critical speeds to the specific operation speed can be determined.

5. Conclusion

The paper presented the implementation of two different ball bearing models in three rotors supported by two identical ball bearings, a turbo blower, a high-speed machine and a high-speed generator, respectively. The main findings from the study can be concluded as follows.

1. The ball bearing stiffness coefficients obtained from the two ball bearing models are identical in the turbo blower up to 2000 rpm, in the high-speed machine up to 7500 rpm and in the high-speed generator up to 16,000 rpm.
2. With the improved model, where the centrifugal force and gyroscopic moment is included, the stiffness for the turbo blower at 16,000 rpm is decreased by 18% in the axial direction, 27% in the radial direction y and 30% in the radial direction z where a load is applied. For the high-speed machine the axial stiffness is decreased at 45,000 rpm by 14% in the axial direction, and 32% in the radial directions. For the high-speed generator at 70,000 rpm the stiffness is decreased by 18% in the axial direction and 39% in the radial directions.
3. In the turbo blower case, a clear difference in the Campbell diagram is visible over 9000 rpm between the simplified and improved bearing models. For this structure after 9000 rpm, the improved bearing model is justified. In the high-speed machine the two bearing models start to differ noticeably above 15,000 rpm and in the higher rotation speeds the improved model is justified. In the high-speed generator, the two bearing models differ at higher than 16,000 rpm then, the improved model is justified.

For future development, the studied models could be tested with actual bearings and could also try to eliminate parameters in order to propose an analytical equation for the modeling purpose of what the limiting rotation speed is when the improved model should be used.

References

[1] A. Jones, A general theory for elastically constrained ball and radial roller bearings under arbitrary load and speed conditions, J. Basic Eng. 82 (2) (1960) 309–320.
[2] T.A. Harris, M.N. Kotzalas, Advanced Concepts of Bearing Technology: Rolling Bearing Analysis, fifth edn CRC Press, 2006.
[3] B.J. Hamrock, D. Dowson, Ball Bearing Lubrication: The Elastohydrodynamics of Elliptical Contacts, Wiley-Interscience, 1981.
[4] N. Tandon, A. Choudhury, A review of vibration and acoustic measurement methods for the detection of defects in rolling element bearings, Tribol. Int. 32 (8) (1999) 469–480.
[5] N. Aktürk, M. Uneeb, R. Gohar, The effects of number of balls and preload on vibrations associated with ball bearings, J. Tribol. 119 (4) (1997) 747–753.
[6] N. Aktürk, The effect of waviness on vibrations associated with ball bearings, J. Tribol. 121 (4) (1999) 667–677.

[7] G. Jang, S.-W. Jeong, Nonlinear excitation model of ball bearing waviness in a rigid rotor supported by two or more ball bearings considering five degrees of freedom. Transactions—American Society of Mechanical Engineers, J. Tribol. 124 (1) (2002) 82–90.
[8] G. Jang, S.-W. Jeong, Analysis of a ball bearing with waviness considering the centrifugal force and gyroscopic moment of the ball. Transactions—American Society of Mechanical Engineers, J. Tribol. 125 (3) (2003) 487–498.
[9] G. Jang, S.-W. Jeong, Vibration analysis of a rotating system due to the effect of ball bearing waviness, J. Sound Vib. 269 (3) (2004) 709–726.
[10] J. Sopanen, A. Mikkola, Dynamic model of a deep-groove ball bearing including localized and distributed defects. Part 1: theory, Proc. Inst. Mech. Eng. Part K J. Multi-body Dyn. 217 (3) (2003) 201–211.
[11] J. Sopanen, A. Mikkola, Dynamic model of a deep-groove ball bearing including localized and distributed defects. Part 2: implementation and results, Proc. Inst. Mech. Eng. Part K J. Multi-body Dyn. 217 (3) (2003) 213–223.
[12] B. Changqing, X. Qingyu, Dynamic model of ball bearings with internal clearance and waviness, J. Sound Vib. 294 (1) (2006) 23–48.
[13] C. Bai, H. Zhang, Q. Xu, Effects of axial preload of ball bearing on the nonlinear dynamic characteristics of a rotor-bearing system, Nonlinear Dyn. 53 (3) (2008) 173–190.
[14] M. Nakhaeinejad, M.D. Bryant, Dynamic modeling of rolling element bearings with surface contact defects using bond graphs, J. Tribol. 133 (1) (2011) 1–12.
[15] L.-X. Xu, Y.-H. Yang, Y.-G. Li, C.-N. Li, S.-Y. Wang, Modeling and analysis of planar multibody systems containing deep groove ball bearing with clearance, Mech. Mach. Theory 56 (1) (2012) 69–88.
[16] A. Liew, N. Feng, E. Hahn, Transient rotordynamic modeling of rolling element bearing systems, J. Eng. Gas Turbines Power 124 (4) (2002) 984–991.
[17] E. Kurvinen, J. Sopanen, A. Mikkkola, Comparison of ball bearing model performance with and without centrifugal and gyroscopic forces, ASME International Mechanical Engineering Congress and Exposition, Proceedings (IMECE), ASME 2014, pp. 1–10.
[18] J. Pyrhönen, J. Nerg, A. Mikkola, J. Sopanen, T. Aho, Electromagnetic and mechanical design aspects of a high-speed solid-rotor induction machine with no separate copper electric circuit in the megawatt range, Electr. Eng. 91 (1) (2009) 35–49.
[19] G. Genta, Dynamics of Rotating Systems, Springer, 2005.
[20] P. Kohnke, ANSYS, Inc. theory manual, Twelfth edition SAS IP Press, 2001, 1286 p.
[21] W. Chen, E. Gunter, Introduction to Dynamics of Rotor-bearing Systems, Trafford on Demand Pub, 2005.
[22] M. Butner, B. Murphy, R. Akian, The influence of mounting compliance and operating conditions on the radial stiffness of ball bearings: analytic and test results, ASME Rotating Machinery and Vehicle Dynamics, DE, 35 1991, pp. 155–162.
[23] Y. Cao, Y. Altintas, A general method for the modeling of spindle-bearing systems, J. Mech. Des. 126 (6) (2004) 1089–1104.

Publication II

Kurvinen E., Sopanen J., and Mikkola A.
Comparison of ball bearing model performance with and without centrifugal and gyroscopic forces

Reprinted with permission from
ASME Proceedings IMECE,
International Mechanical Engineering Congress and Exposition.
Montreal, Canada, 14.-20.11.2014,

Proceedings of the ASME 2014 International Mechanical Engineering Congress & Exposition
IMECE2014
November 14–20, 2014, Montreal, Quebec, Canada

IMECE2014-37880

COMPARISON OF BALL BEARING MODEL PERFORMANCE WITH AND WITHOUT CENTRIFUGAL AND GYROSCOPIC FORCES

Emil Kurvinen*
Lappeenranta University of Technology
Department of Mechanical Engineering
P.O. Box 20, FI-53851 Lappeenranta, Finland
emil.kurvinen@lut.fi

Jussi Sopanen
Lappeenranta University of Technology
Department of Mechanical Engineering
P.O. Box 20, FI-53851 Lappeenranta, Finland
jussi.sopanen@lut.fi

Aki Mikkola
Lappeenranta University of Technology
Department of Mechanical Engineering
P.O. Box 20, FI-53851 Lappeenranta, Finland
aki.mikkola@lut.fi

ABSTRACT

Bearing performance significantly affects the dynamic behaviors and estimated working life of a rotating system. A common bearing type is the ball bearing, which has been under investigation in numerous published studies. The complexity of the ball bearing models described in the literature varies as models with or without the inclusion of centrifugal forces or the gyroscopic moments of the rolling elements are equally proposed. Naturally, model complexity is related to computational burden. In particular, the inclusion of centrifugal forces and gyroscopic moments significantly increases the system degrees of freedom and lengthens solution time. On the other hand, for low or moderate rotating speeds, these effects can be neglected without significant loss of accuracy.

The objective of this paper is to present guidelines for the appropriate selection of a suitable bearing model for a case study. To this end, two ball bearing models were implemented. One considers high-speed forces, and the other neglects them. Both models were used to study a single structure, and the simulation results were compared. The bearing behavior is studied at different shaft rotation speeds and the simulation results are used to determine when the model containing the centrifugal and gyroscopic forces should be used.

NOMENCLATURE

Latin	
c_d	Clearance
d	Ball diameter
d_m	Pitch diameter
d_s	Bore diameter
$d_m^{'}$	Pitch diameter under loading
D	Diameter
e	Eccentricity
$E^{'}$	Effective modulus of elasticity
E	Modulus of elasticity
f	Conformity ratio
F	Force
I_p	Polar moment of inertial
j	Number of ball
K_con	Contact stiffness coefficient
$\tilde{k}_\mathrm{e}$	Approximated ellipticity parameter
L	Distance (Figure 6)

*Address all correspondence to this author.

m	Mass of the ball
n	Number of balls
M_g	Gyroscopic moment
r	Radius
R	Curvature sum
R_d	Curvature difference
R_x	Effective radii of curvature in x-plane
R_y	Effective radii of curvature in y-plane
T	Moment

Greek

α	Contact angle
β	Attitude angle (azimuth angle)
γ	Misalignment
δ	Deformation
$\tilde{\zeta}$	Second ellipticity integral
θ	Angle between the shaft centerline and ball rotational axis
$\tilde{\xi}$	First ellipticity integral
λ	Race control
ν	Poisson's ratio
ϕ	Contact angle
ψ	Angular location
ω	Rotation speed

Subscripts

ay	Solid a, y-direction
ax	Solid a, x-direction
B	Ball
by	Solid b, y-direction
bx	Solid b, x-direction
c	Centrifugal
f	Initial contact angle
i/in	Inner race
j	j th ball
o/out	Outer race
s	Shaft
x	Axis x-direction
y	Axis y-direction
z	Axis z-direction

Superscripts

in	Inner
out	Outer
r	Radial
t	Axial
tot	Total

1 INTRODUCTION

Bearings have a critical role in rotating machinery systems and the unexpected failure of the bearing might break the machine. A commonly used bearing type is the deep groove ball bearing that is under investigation in this paper. The basic structure in ball bearings is that the balls rotate inside two steel rings (races) and the balls are kept separate by a cage. Detailed design varies depending on the specific type of bearing whereas the basic concept is the same in every ball bearing.

Modeling the dynamical behavior of a ball bearing includes several simultaneous contacts between the bearing components that make an accurate simulation of the ball bearing's dynamic behavior challenging and computationally expensive.

The general theory for the elastically constrained ball and roller bearing was proposed by Jones [1] and later verified and generalized by Harris [2] and Hamrock and Dowson [3]. The model did not include any geometrical imperfections, these occur due to the manufacturing and installation process. Several studies were performed to consider the imperfections and defects in the bearing. Aktürk et al. [4, 5] proposed a three degree of freedom ball bearing model where the effects of waviness, axial preload, and number of balls were studied.

Jang and Jeong [6] developed a five degree of freedom model to study the waviness in the races and balls. Later, Jang and Jeong [7] included the centrifugal force and gyroscopic moment to the proposed model and studied the waviness order effect of the,*e.g*, stiffness and contact force.

Sopanen and Mikkola [8, 9] developed a six degree of freedom ball bearing model where the additional degree of freedom is the friction torque around the rotational axis. The model was used to study the effect of the inner and outer race waviness and localized defects. The model did not include the centrifugal force and gyroscopic moment due to moderate rotation speeds of the studied applications.

Changqing and Qingyu [10] proposed five degrees of freedom model where the centrifugal force and gyroscopic moment are included. The internal clearance, axial preload, radial load, and waviness were studied. In general, several models are proposed and the main focus of the research has been to study the effect of different imperfections. The first models consider only three degrees of freedom and the latter studies consider five or six degrees of freedom and include the centrifugal force and gyroscopic moment effect.

The inclusion of the high speed forces has significant effect on the computational burden. For bearing performance, the main effect of the centrifugal forces is that the contact angles in the ball to inner race and ball to outer race contact have different values. This is contrary to the simplified ball bearing model where the contact angles can be assumed to be approximately identical. In the case of high rotation speed the different contact angles causes that the ball cannot roll without sliding which, in turn, creates additional frictional heat and limits the maximum rotation speed of the bearing. Difference in the contact angles affects the bearing stiffness. The rotational velocity causes the contact angles variation and due to this the stiffness changes as a function of rotation velocity.

In this paper, the theories behind two different ball bearing models are briefly presented and then one case example is presented. The aim of this study is to analyze the rotation speed range between moderate and high-speed and to give more accurate information as to when the centrifugal force and gyroscopic moment should be included in the model and when these can be neglected.

2 SYSTEM MODELING

The simplified model is based on the relative displacements and velocities between the inner and outer races. Displacements and velocities can be calculated by creating a geometrical relationship. Accordingly, the relationship between the force-deflection can be expressed. The model has five degrees of freedom, three translational and two rotational degrees of freedom. The model includes non-linear Hertzian contact deformation. The geometry and material parameters are given as input and the bearing forces and torques are solved. The simplified model does not consider the high-speed forces.
The refined model is based on the force equilibrium between the external applied load and the internal load within the bearing. Rotation dependent forces, centrifugal force and gyroscopic moment of the ball are included. In the equilibrium condition, the deformation of the ball bearing is solved. The ball bearing contains several parts including the cage that holds the balls in a fixed distance from the inner and outer race, which connect the bearing to the shaft and housing, and the balls. Each part should be considered in details when creating an accurate mathematical model. However, the model should be computationally efficient and therefore the following general assumptions are made to decrease the degrees of freedom in the models:

1. Friction torque is neglected.
2. Effect of elastohydrodynamic film is neglected.
3. Defects and form error of the unit are neglected.

The relative difference between the two models by exluding the effect of friction torque and elastohydrodynamic film are negligble and due that those are not considered in the models. Defects and form error of the bearing are not included and they are assumed to be perfectly manufactured, *i.e* the balls are round and races are circular.

2.1 Ball bearing dynamic model without centrifugal and gyroscopic forces (simplified)

The theory of modeling the deep-groove ball bearing is presented in detail in [8]. The modeling theory is briefly reviewed in this paper in order to provide a complete presentation.

2.1.1 Elliptical contact conjunction

The elliptical contact conjunction is used to determine the contact stiffness between the ball and races. In ball bearings, the ball and race are two solids that have different radii of curvature in two directions. Figure 1 shows the contact geometry and the normal force, F, applied to two solids. The radius of contact conjunction is defined to be positive when the surface is convex and negative when concave. The curvature sum, R, and curvature difference, R_{d} , that are used to define the contact deformation are as

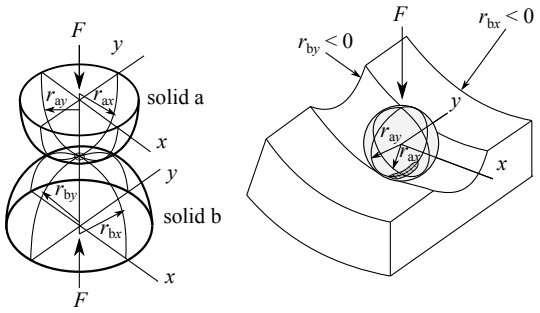

FIGURE 1. ELLIPTICAL CONTACT CONJUNCTIONS

$$\begin{aligned}
&\tfrac{1}{R} = \tfrac{1}{R_x} + \tfrac{1}{R_y} \\
&R_{\mathrm{d}} = R\left(\tfrac{1}{R_x} - \tfrac{1}{R_y}\right), \text{where} \\
&\tfrac{1}{R_x} = \tfrac{1}{r_{\mathrm{ax}}} + \tfrac{1}{r_{\mathrm{bx}}}, \tfrac{1}{R_y} = \tfrac{1}{r_{\mathrm{ay}}} + \tfrac{1}{r_{\mathrm{by}}}
\end{aligned} \tag{1}$$

where R_x and R_y represent the effective radii of curvature in the x and y planes. Subscripts ax, ay, bx and by refer to the radiuses in solids a and b in x- and y-directions, respectively. When the normal force is applied to the solids the contact area is elliptical. The contact stiffness coefficient, K_{con}, for the elliptical contact conjunction can be calculated as

$$\begin{aligned}
&K_{\mathrm{con}} = \pi \tilde{k}_{\mathrm{e}} E' \sqrt{\tfrac{R\tilde{\xi}}{4.5\tilde{\zeta}^3}}, \text{where} \\
&\tilde{k}_{\mathrm{e}} = 1.0339\left(\tfrac{R_y}{R_x}\right)^{0.6360}, \\
&E' = \tfrac{2}{\frac{1-\nu_{\mathrm{a}}^2}{E_{\mathrm{a}}} + \frac{1-\nu_{\mathrm{b}}^2}{E_{\mathrm{b}}}}, \\
&\tilde{\xi} = 1.003 + 0.5968\left(\tfrac{R_y}{R_x}\right), \\
&\tilde{\zeta} = 1.5277 + 0.6023\ln\left(\tfrac{R_y}{R_x}\right).
\end{aligned} \tag{2}$$

where, $\tilde{k}_e$ is the approximated ellipticity parameter, E' is the effective modulus of elasticity, ν is the Poisson's ratio, E is the material modulus of elasticity and subscripts a and b refers to solids that are in contact. Parameters $\tilde{\xi}$ and $\tilde{\zeta}$ are the approximation formulae for first and second elliptical integrals [3].

2.1.2 Ball bearing geometry and total stiffness coefficient and displacements

The geometry of a deep groove ball bearing is shown in Fig. 2, where d is the ball diameter, r_{out} the outer groove radius, r_{in} is the inner groove radius, c_d is the diametral clearance, D is the bearing housing diameter, d_m is the pitch diameter, d_s is the bore diameter, D_i is the inner raceway diameter, and D_o is the outer raceway diameter, respectively. The relation between con-

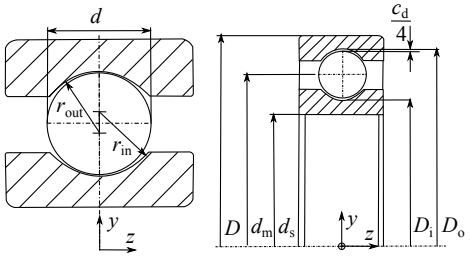

FIGURE 2. ELLIPTICAL CONTACT CONJUNCTIONS

tact stiffness and deformation, δ_0, for a single ball is expressed as

$$\delta_0 = \left(\frac{F}{K_{con}}\right)^{2/3}, \tag{3}$$

where F is the normal load and K_{con} is the contact stiffness coefficient. The total stiffness of a single ball bearing involves the inner, K_{con}^{in}, and the outer ring, K_{con}^{out}, contact stiffness and that is expressed as

$$K_{con}^{tot} = \frac{1}{\left(\left(\frac{1}{K_{con}^{in}}\right)^{2/3} + \left(\frac{1}{K_{con}^{out}}\right)^{2/3}\right)^{3/2}}. \tag{4}$$

2.1.3 Ball bearing forces and moments in the complete ball bearing

Ball bearing forces and moments are calculated from the relative displacements between the rings. Figure 3 shows the layout for each ball and the relative displacements between the inner and outer ring.

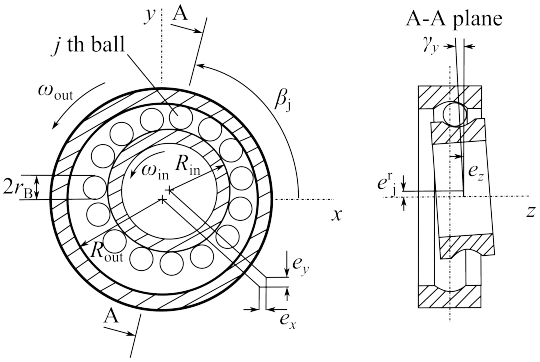

FIGURE 3. AXIAL AND TRANSVERSE CROSS-SECTION IN THE A-A PLANE OF ILLUSTRATIVE STRUCTURE OF A BALL BEARING

Radial, e_j^r, and axial, e_j^t, displacements in of ball j can be stated as

$$\begin{aligned} e_j^r &= e_x \cos\beta_j + e_y \sin\beta_j \\ e_j^t &= e_z - (-\gamma_x \sin\beta_j + \gamma_y \cos\beta_j)(R_{in} + r_{in}) \end{aligned} \tag{5}$$

where e_x, e_y, e_z are the given relative displacements in x, y, z directions, β_j is the attitude angle (azimuth angle) of ball j and γ_x and γ_y are the angular misalignments of the inner race about x and y axes. The contact angle for ball j is depicted in Fig. 4.

Contact angle, ϕ_j, for ball j can be calculated as

$$\phi_j = \tan^{-1}\left(\frac{e_j^t}{R_{in} + r_{in} + e_j^r - R_{out} + r_{out}}\right). \tag{6}$$

The distance between the race surfaces along the line of contact is then calculated as

$$d_j = r_{out} + r_{in} - \frac{R_{in} + r_{in} + e_j^r - R_{out} + r_{out}}{\cos\phi_j}. \tag{7}$$

The total elastic deformation can then be calculated as

$$\delta_j^{tot} = 2r_B - d_j. \tag{8}$$

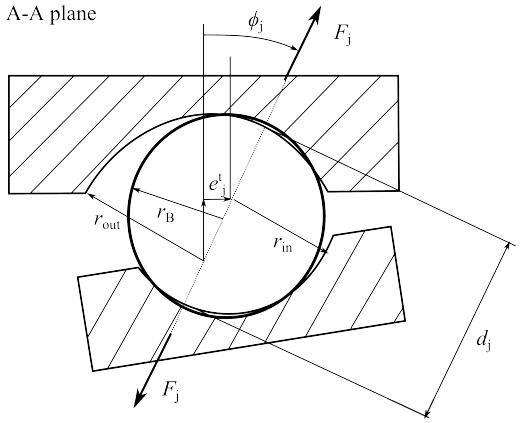

FIGURE 4. CROSS-SECTION OF A BALL BEARING IN THE A-A PLANE

The contact force acting on ball j can be calculated for each ball as

$$F_j = K_{con}^{tot}(\delta_j^{tot})^{3/2}, \tag{9}$$

where K_{con}^{tot} is the total stiffness coefficient determined by Eq. 4. The resultant bearing forces and moments in the shaft can be calculated in respect of the x, y and z directions as

$$\left.\begin{aligned} F_x &= -\sum_{j=1}^{n} F_j \cos\phi_j \cos\beta_j \\ F_y &= -\sum_{j=1}^{n} F_j \cos\phi_j \sin\beta_j \\ F_z &= -\sum_{j=1}^{n} F_j \sin\phi_j \\ T_x &= -\sum_{j=1}^{n} F_j (R_{in}+r)\sin\phi_j \sin\beta_j \\ T_y &= -\sum_{j=1}^{n} F_j (R_{in}+r)\sin\phi_j \left(-\cos\beta_j\right) \end{aligned}\right\} \tag{10}$$

It should be noted that in summations in Eq. 10 only the force components where compression exists between the races and ball are included, *i.e.*, $\delta_j^{tot} > 0$.

2.2 Ball bearing dynamic model with centrifugal and gyroscopic forces (complex)

In high-speed operations, the contact angles in the inner and outer race contacts are no longer identical. This will have a noticeable effect on the ball bearing dynamic behavior. Figure 5 shows the forces and contact angles within a single ball and the position of jth ball in the bearing. The ball is subjected to the centrifugal force, F_c, and the contact forces on the inner and outer races, F_i and F_o. In addition, a gyroscopic moment, M_g, and counter friction forces are affecting to the ball deformation. The force equilibrium for a single ball can be calculated when the contact angles are known in the inner and outer races α_i and α_o, respectively. Notation λ represent the race control and it has a value of 0 or 1.

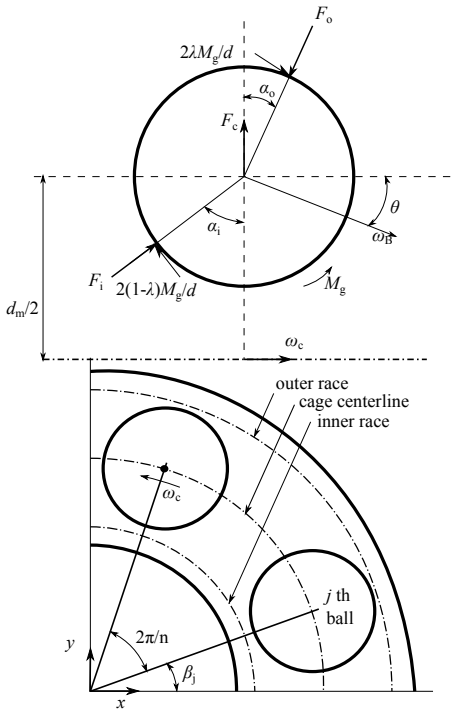

FIGURE 5. FORCES AND MOMENTS ACTING ON THE BALL ON HIGH-SPEED OPERATION.

In the case of a substantial centrifugal force, the contact angles in the inner and outer race contacts are different. Figure 6 shows the initial and final (loaded) positions of the ball and inner race curvature center. Based on Fig. 6 the following geometric relation for the each ball can be expressed using Pythagorean

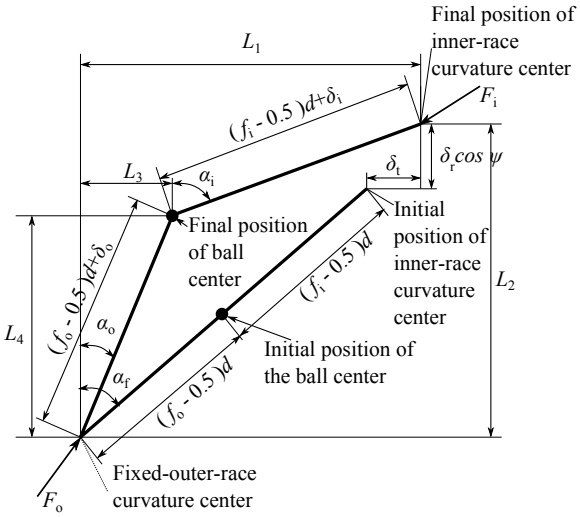

FIGURE 6. DEFLECTION OF THE CENTER OF BALL AND CURVATURE RACES AT ANGULAR LOCATION . [3]

theorem as

$$\begin{aligned} &L_4^2+L_3^2-[(f_o-0.5)\,d+\delta_o]^2=0\\ &(L_2-L_4)^2+(L_1-L_3)^2-[(f_i-0.5)\,d+\delta_i]^2=0, \end{aligned} \tag{11}$$

where f_i and f_o are the inner and outer race conformity ratio that is a measure of the geometrical conformity of the race and the ball in a plane that passes through the center of the bearing and is transverse to the race (shown in Fig. 2). Forces applied to the ball are shown in Fig. 5, and these can be calculated when the total elastic deformation in the inner and outer race contacts and the stiffness coefficients are known as

$$\begin{aligned} F_o &= K_o\delta_o^{3/2}\\ F_i &= K_i\delta_i^{3/2}. \end{aligned} \tag{12}$$

The equilibrium condition for each ball can be expressed with the help of Newton's second law as

$$\begin{aligned} &F_o\sin\alpha_o-F_i\sin\alpha_i\\ &-\tfrac{2M_g}{d}\left[\lambda\cos\alpha_o-(1-\lambda)\cos\alpha_i\right]=0\\ &F_o\cos\alpha_o-F_i\cos\alpha_i\\ &+\tfrac{2M_g}{d}\left[\lambda\sin\alpha_o-(1-\lambda)\sin\alpha_i\right]-F_c=0, \end{aligned} \tag{13}$$

where λ have value of 1 in case of outer-race control and 0 when inner-race control is applied. The race control theory was proposed by Jones [1], where λ is a calculated parameter to define the race in which no slipping occurs. The required torques to spin the ball against the inner and outer race is evaluated. A race, which requires more torque to spin, defines the race control, *i.e.* if λ is 1 the outer-race control exists and when λ is 0 then the inner race contact exists. In Eq. 13 the centrifugal force can be expressed as

$$F_c=\frac{1}{2}md_m'\omega_c^2, \tag{14}$$

where m is mass of the ball, $d_m'$is the pitch diameter under loading and ω_c is the angular velocity of the cage. Pitch diameter under loading can be expressed as a function of nominal pitch diameterd_m, ball diameter d, outer race conformity ratio and initial contact angle as

$$d_m'=d_m+2L_4-2d\,(f_o-0.5)\cos\alpha_f \tag{15}$$

The gyroscopic moment of the ball can be calculated as

$$M_g=I_p\omega_B\omega_c\sin\theta, \tag{16}$$

where I_p is the mass moment of inertia of the ball, ω_B is the angular velocity of the ball about its rotation axis, ω_c is the angular velocity of the cage and θ is the angle between the shaft center line and ball rotational axis. Equation 13 can be re-expressed as

$$\begin{aligned} &\tfrac{K_o\delta_o^{3/2}L_3}{d(f_o-0.5)+\delta_o}-\tfrac{K_i\delta_i^{3/2}(D\sin\alpha_f+\delta_t-L_3)}{d(f_i-0.5)+\delta_i}\\ &-\tfrac{2}{d}I_p\omega_B\omega_c\sin\theta\left[\begin{array}{l}\tfrac{\lambda L_4}{d(f_o-0.5)+\delta_o}\\ -\tfrac{(1-\lambda)(D\cos\alpha_f+\delta_r\cos\psi-L_4)}{d(f_i-0.5)+\delta_i}\end{array}\right]=0,\\ &\tfrac{K_o\delta_o^{3/2}L_4}{d(f_o-0.5)+\delta_o}-\tfrac{K_i\delta_i^{3/2}(D\cos\alpha_f+\delta_r\cos\psi-L_4)}{d(f_i-0.5)+\delta_i}\\ &+\tfrac{2}{d}I_p\omega_B\omega_c\sin\theta\left[\begin{array}{l}\tfrac{\lambda L_3}{d(f_o-0.5)+\delta_i}\\ -\tfrac{(1-\lambda)(D\sin\alpha_f+\delta_t-L_3)}{d(f_i-0.5)+\delta_i}\end{array}\right]\\ &-\tfrac{m\omega_c^2}{2}\left[d_e+2L_4-2\,(f_o-0.5)\,d\cos\alpha_f\right]=0. \end{aligned} \tag{17}$$

The iterative solution is required due the nonlinear equations and the Newton-Raphson method is utilized to solve the four equations in Eq. 11 and Eq. 17. The unknowns to solve are L_3, L_4,

δ_i and δ_o. Good assumptions for tangential and radial displacement, δ_t and δ_r , can be made by using a condition of equilibrium applied to the complete ball bearing,

$$\begin{aligned} F_t - \sum_{k=1}^{n} \left[F_{kj} \sin \alpha_{kj} - \frac{2\left(1-\lambda_j\right) M_{gj}}{d} \cos \alpha_{kj} \right] = 0, \\ F_r - \sum_{k=1}^{n} \left[F_{kj} \cos \alpha_{kj} - \frac{2\left(1-\lambda_j\right) M_{gj}}{d} \sin \alpha_{kj} \right] \cos \psi_j = 0, \end{aligned} \tag{18}$$

where F_t is the axial load and F_r is the radial load. [3]

3 CASE STUDY AND RESULTS

The two developed models are implemented into a solid rotor blower model supported with two 6014 hybrid deep-groove ball bearings. The rotor's geometry is similar to that presented earlier in Pyrhönen et al. [11]. However, in this study, the constant bearing stiffnesses used in the earlier work have been replaced by stiffnesses obtained using the developed ball bearing models.

3.1 Turbo blower structure

The main layout and dimensions of the turbo blower are shown in Fig. 7 while the parameters used in the analysis are shown in Tab. 1.

TABLE 1. PARAMETERS USED IN THE ANALYSIS.

Modulus of elasticity	210 GPa
Material density	$7,800\ \frac{\text{kg}}{\text{m}^3}$
Poisson's ratio (rotor)	0.3
Properties of the slitted part	
Area	$0.0251\ \text{m}^2$
Second moment of area	$6.2832 \times 10^{-5}\text{m}^4$
Impeller mass properties	
Mass	19.0 kg
Polar mass moment of inertia	$0.5\ \text{kgm}^2$
Diametral mass moment of inertia	$0.3\ \text{kgm}^2$
Stiffness of impeller attachment	
Translational	$1.0 \times 10^{11}\ \frac{\text{N}}{\text{m}}$
Rotational	$1.5 \times 10^{6}\ \frac{\text{Nm}}{\text{rad}}$
Rotor unbalance masses	
D1 Impeller (node 23)	36 gmm@270°
D1 Rotor end (node 9)	50 gmm@0°
D2 Rotor end (node 14)	50 gmm@0°
D2 Impeller (node 24)	50 gmm@90°
Total mass of the rotor	174.85 kg

The turbo blower is supported with two SKF 6014/HC2 deep-groove ball bearings. The main bearing dimension and parameters are shown in the Tab. 2.

TABLE 2. DIMENSIONS OF THE 6014\HC2 TYPE DEEP-GROOVE HYBRID BALL BEARING.

Bore diameter, d_s	70 mm
Outer diameter, D	110 mm
Width, W	20 mm
Pitch diameter, d_m	89.85 mm
Ball diameter, d	11.91 mm
Number of balls, n	14
Diametral clearance C2, c_d	5.5 µm
Bearing damping coefficient, c_b	$0.55\ \frac{\text{Ns}}{\text{mm}}$
Inner and outer race conformity, R_i, R_o	0.52
Static load rating, C0,	31,000 N
Modulus of elasticity (races), E_r	207 GPa
Poisson's ratio (races), ν_r	0.3
Modulus of elasticity (balls), E_b	315 GPa
Density (balls), ρ_b	$3,200\ \frac{\text{kg}}{\text{m}^3}$
Poisson's (balls), ν_b	0.26
Reference speed, n_{max}	$16,000\ \text{min}^{-1}$

Both bearings are loaded with 300 N axial load and 700 N radial load (z-direction).

3.2 Results of the simulation

Two bearing models were implemented into the rotor dynamic model of the blower. Analysis was performed using a custom in-house code in Matlab software.

3.2.1 Ball bearing stiffness coefficients

In the simplified ball bearing model the bearing stiffness coefficient does not depend on the rotation speed. On the contrary, in a high speed bearing model the bearing stiffnesses are strongly dependent of the rotation speed. The diagonal stiffness values for the simplified bearing model in the translational direction are shown in the Tab 3.

TABLE 3. AXIAL AND RADIAL STIFFNESSES WITH THE SIMPLIFIED BEARING MODEL

Axial stiffness	Radial stiffness	Radial stiffness
x (N/m)	y (N/m)	z (N/m)
2.021×10^7	2.8445×10^8	2.7784×10^8

The stiffness values from 0 min^{-1} to 16,000 min^{-1} for the

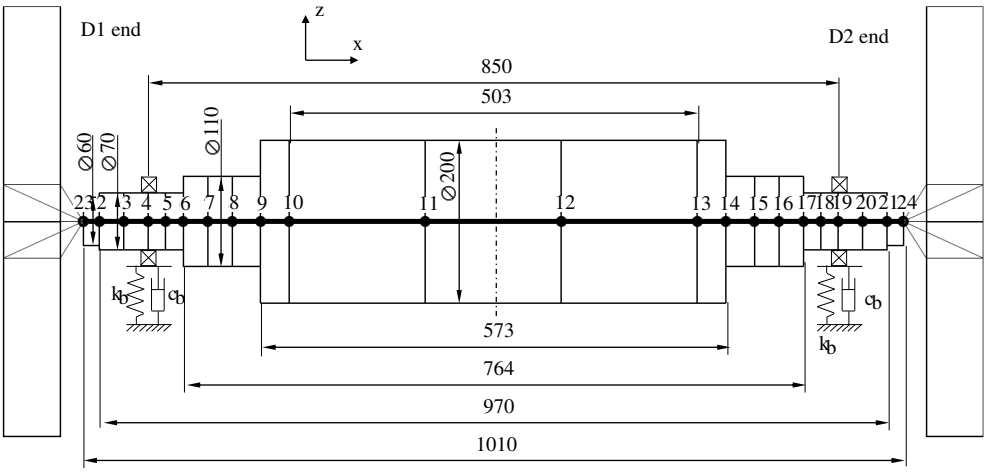

FIGURE 7. LAYOUT OF THE TURBO BLOWER WITH TWO IMPELLERS. THE DIMENSIONS ARE IN MILLIMETERS. THE SLITTED PART OF THE ROTOR IS BETWEEN NODES 10 AND 13.

high speed model are shown in Fig. 8. It can be seen that the stiffness decreases as the rotation speed increases.

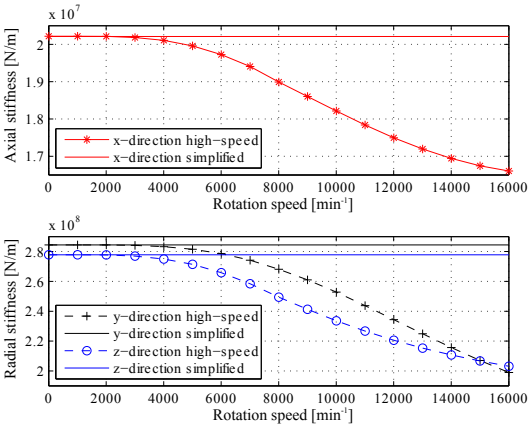

FIGURE 8. BEARING STIFFNESSES IN THE AXIAL AND RADIAL DIRECTIONS AS A FUNCTION OF ROTATION SPEED 0 TO 16,000 min^{-1}.

Based on Tab. 3 and Fig. 8 it can be concluded that at moderate rotation speeds the stiffness coefficients are in good agreement between the two models. In the studied case, the stiffness coefficients significantly differ after the rotor begins rotating over 2,000 min^{-1}. The stiffness coefficient decreases rapidly and at the maximum rotation speed the axial stiffness decreases by a total of 18.0 %, the radial direction in y-direction by 27.0 % and the z-direction by 30.0 % (i.e. direction of the applied force) from the initial stiffness coefficient. The stiffness decreases due to the centrifugal force and gyroscopic moment.

3.2.2 Campbell diagram

In a Campbell diagram, the natural frequencies of the rotor-bearing systems are shown as a function of rotation speed. The critical speeds are found from the diagram. The Campbell diagrams for the two bearing models are shown in Fig. 9. It can be seen in Fig. 9 that at moderate rotation speeds the Campbell diagrams are identical and as the rotation speed increases the whirling frequencies starts to differ. The first two critical speeds occur approximately in the same rotation speed and the third and fourth critical speeds occurs in the lower rotation speed in the simple bearing model.The whirling modes of the critical speeds are marked in the Fig. 9. A Comparison of the critical speeds in the two models is shown in Tab. 4.

The two first critical speeds occur close to each other and there is no clear difference between the models used to study this case. A clear difference can be seen in the third and fourth crit-

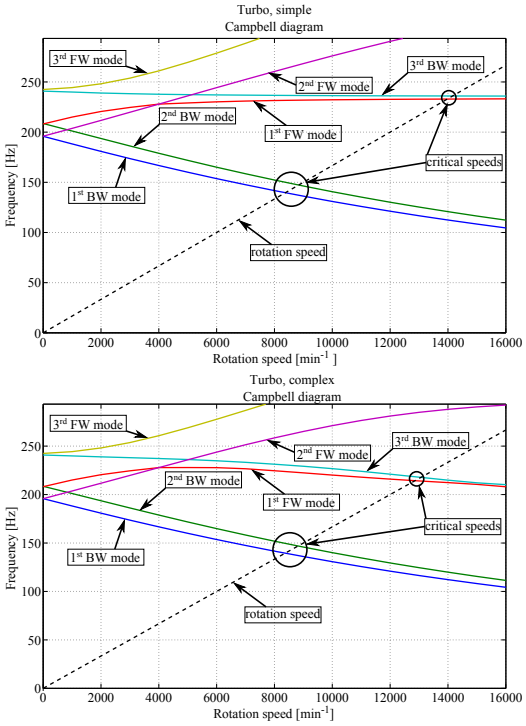

FIGURE 9. CAMPBELL DIAGRAMS. THE TOP WITH THE SIMPLE BEARING MODEL AND THE BOTTOM WITH COMPLEX BEARING MODEL.

TABLE 4. CRITICAL ROTATION SPEEDS FROM THE CAMPBELL DIAGRAM

#	Critical speed [min^{-1}]		
	Simple model	High speed model	Difference [%]
1	8,378	8,372	0.07
2	8,836	8,816	0.23
3	13,977	12,861	8.68
4	14,160	13,065	8.38

ical speed. The critical speeds in the case of a high-speed ball bearing model are over 8 % lower than with the simple bearing model. The rotor is designed to rotate 11,000 min^{-1}. With the simple bearing model and the current model the safety margin is 20 % for lower and higher rotational velocities. On this range the critical speeds are not conflicting in the operation rotational velocity. The complex bearing model results in a 5 % lower safety margin due the third and fourth critical speeds being closer to the operation speed.

3.2.3 Critical speed map

In the critical speed map, the general relation between the support stiffness and the system can be seen. Figure 10 shows the critical speed map where the radial bearing stiffness (z) varies and the four first modes are shown. Axial (x) and radial (y) stiffness coefficients are kept constant. The values are similar to that obtained with a simple ball bearing model (Tab. 3).

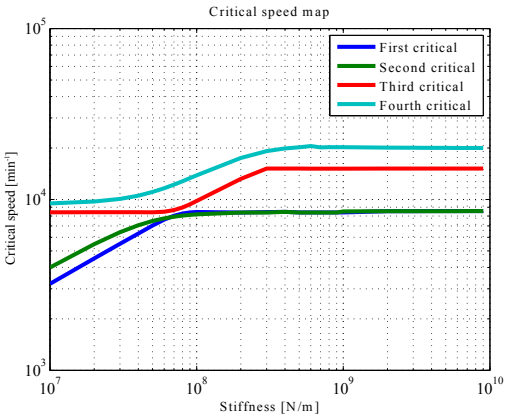

FIGURE 10. UNDAMPED CRITICAL SPEED MAP WHERE THE RADIAL STIFFNESS IN DIRECTION Z IS VARIED

The two critical speeds have an inclining section when the bearing stiffness increases above $5.0 \times 10^7 \frac{N}{m}$. Below this value the bearing stiffness mainly determines the critical speed of the rotor system. Correspondingly, for bearing stiffnesses higher than $5.0 \times 10^7 \frac{N}{m}$, the flexibility of the rotor has a more significant influence on the critical speeds. Therefore, the critical speed map clearly explains why the first and second critical speeds are not affected by the different bearing stiffnesses as the third and fourth critical are.

4 DISCUSSION

In the case of ball bearings, an increase in the model complexity leads to an increased number of input parameters and initial guesses that are crucial for successful simulation. The theoretical background for modelling ball bearings, including the centrifugal and gyroscopic forces, has been available since

1960. Nevertheless, it is still unclear under which conditions (*e.g.* size of the rotor or rotation speed range) there is an obligation to use or not use the model including the high speed effects.

The studied case shows that the stiffness of the bearing with the used parameters is almost identical in both models up to 2,000 min^{-1}. If the structure is designed to rotate slower than 2,000 min^{-1} then the high-speed model is not justified. For the studied structure the results obtained using different bearing models are almost identical up to 9,000 min^{-1}. Above this speed the difference is, on the other hand, very clear. The third and fourth critical speeds especially decrease noticeably with the high-speed model. In this case, the safety margin for the simple model is 20 % at the nominal speed of 11,000 min^{-1}. For the high-speed model the safety margin is 15 %. In the literature it is stated that for low and moderate speeds the centrifugal and gyroscopic forces can be ignored and at high-speeds it is obligatory to consider them. For the studied rotor and with the used bearing type the results are in agreement with the general statement in the literature.

It should be noted that results might vary even with the same structure when, for example, the clearance or bearing loading is varied. Due to this, common rules for the studied structure cannot be suggested.

The critical speed map shows that the stiffness variation in the high-speed bearing model does not decrease the stiffness sufficiently for it to have an influence on the first two critical speeds. The difference between the third and fourth critical speeds can also be seen in the critical speed map. As the bearing stiffness decreases, the critical speeds also decrease.

5 CONCLUSION

The paper presented the implementation of two different ball bearing models into a solid rotor electric motor supported by two identical ball bearings. The main findings from the study can be concluded as

- The ball bearing stiffness coefficients obtained from the two models are identical up to 2,000 min^{-1}.
- With the complex model, where the centrifugal force and gyroscopic moment is included, the stiffness at the 16,000 min^{-1} is decreased by 18 % in the axial direction, 27 % in the radial direction y and 30 % in the radial direction z where a load is applied.
- In the studied case a clear difference in the Campbell diagram is visible over 9,000 min^{-1} between the simple and high speed bearing models.

For future development, the studied models could be implemented into different structures with different size bearings in order to discover a more general rule to justify the complex bearing model.

REFERENCES

[1] Jones, A., 1960. "A general theory for elastically constrained ball and radial roller bearings under arbitrary load and speed conditions". *Journal of Basic Engineering,* ***82***(2), pp. 309–320.

[2] Harris, T. A., and Kotzalas, M. N., 2006. *Advanced Concepts of Bearing Technology: Rolling Bearing Analysis*, fifth edition ed. CRC Press.

[3] Hamrock, B. J., and Dowson, D., 1981. *Ball bearing lubrication: the elastohydrodynamics of elliptical contacts*. Wiley-Interscience.

[4] Aktürk, N., Uneeb, M., and Gohar, R., 1997. "The effects of number of balls and preload on vibrations associated with ball bearings". *Journal of tribology,* ***119***(4), pp. 747–753.

[5] Aktürk, N., 1999. "The effect of waviness on vibrations associated with ball bearings". *Journal of tribology,* ***121***(4), pp. 667–677.

[6] Jang, G., and Jeong, S.-W., 2002. "Nonlinear excitation model of ball bearing waviness in a rigid rotor supported by two or more ball bearings considering five degrees of freedom". *Transactions-American Society of Mechanical Engineers Journal of Tribology,* ***124***(1), pp. 82–90.

[7] Jang, G., and Jeong, S.-W., 2003. "Analysis of a ball bearing with waviness considering the centrifugal force and gyroscopic moment of the ball". *Transactions-American Society of Mechanical Engineers Journal of Tribology,* ***125***(3), pp. 487–498.

[8] Sopanen, J., and Mikkola, A., 2003. "Dynamic model of a deep-groove ball bearing including localized and distributed defects. part 1: Theory". *Proceedings of the Institution of Mechanical Engineers, Part K: Journal of Multi-body Dynamics,* ***217***(3), pp. 201–211.

[9] Sopanen, J., and Mikkola, A., 2003. "Dynamic model of a deep-groove ball bearing including localized and distributed defects. part 2: Implementation and results". *Proceedings of the Institution of Mechanical Engineers, Part K: Journal of Multi-body Dynamics,* ***217***(3), pp. 213–223.

[10] Changqing, B., and Qingyu, X., 2006. "Dynamic model of ball bearings with internal clearance and waviness". *Journal of Sound and Vibration,* ***294***(1), pp. 23–48.

[11] Pyrhönen, J., Nerg, J., Mikkola, A., Sopanen, J., and Aho, T., 2009. "Electromagnetic and mechanical design aspects of a high-speed solid-rotor induction machine with no separate copper electric circuit in the megawatt range". *Electrical engineering,* ***91***(1), pp. 35–49.

Publication III

Uzhegov N., Kurvinen E., Nerg J., Pyrhönen J., Sopanen J., and Shirinskii S.
Multidisciplinary Design Process of a 6-Slot 2-Pole High-Speed Permanent Magnet Synchronous Machine

Reprinted with permission from
Transactions on Industrial Electronics
In press.

Vol. 99, pp. 1–12, 2015.

This article has been accepted for publication in a future issue of this journal, but has not been fully edited. Content may change prior to final publication. Citation information: DOI 10.1109/TIE.2015.2477797, IEEE Transactions on Industrial Electronics

Multidisciplinary Design Process of a 6-Slot 2-Pole High-Speed Permanent Magnet Synchronous Machine

Nikita Uzhegov, *Member, IEEE,* Emil Kurvinen, Janne Nerg, *Senior Member, IEEE,* Juha Pyrhönen, *Member, IEEE,* Jussi Sopanen, *Member, IEEE*, and Sergey Shirinskii, *Member, IEEE*

***Abstract*—High-Speed Permanent Magnet Synchronous Machines (HS PMSM) are a popular topology among modern electrical machines. Suitable applications for such machines are low-power vacuum pumps, compressors and chillers. This paper describes a systematic design methodology for a HS PMSM using two case studies. The design process for such high-speed machines is multidisciplinary and highly iterative due to the complex interaction of the many design variables involved. Consequently, no single optimum solution exists and multiple possible solutions can meet the customer requirements. Practical solutions should be within acceptable thermal limits, energy-efficient and rigid enough to withstand the forces exerted during operation. The proposed design flow is divided into steps that are presented in the paper in the form of a flow chart with emphasis on mechanical aspects. Each step represents a task for a thermal, mechanical or electric engineer. The features of each step and the prerequisites for moving to the next step are discussed. The described methodology was implemented in the design of two HS PMSMs. The output performance results of the design flow are compared with measured results of the prototypes. The design process described in this paper provides a straightforward procedure for the multidisciplinary design of high-speed permanent magnet electrical machines.**

***Keywords*—AC machine, Electrical design, High-speed drive, Mechanical design, Permanent magnet machines, Rotating machines.**

I. Introduction

HIGH-SPEED (HS) electrical machines represent well-established technology and are used in a number of common industrial applications. HS machines provide benefits such as high power density, small footprint and high overall system efficiency. One reason for these advantages is that HS technology enables direct coupling between the HS electrical machine and the working machine, which makes it possible to avoid the requirement for a gearbox. The benefits inherent to such machines have attracted the attention of manufacturers producing, for example, gas compression appliances, turbines, air blowers, vacuum pumps, machine tools and spindle drives [1], [2], and the market for HS machinery has shown exceptional growth over the last decade. This active interest in HS machinery has led to a rise in the number of joint projects between academia and industry [3].

From the design point of view, high-speed technology is challenging, and a lot of research is ongoing regarding efficient and effective solutions development [4]. Successful design and operation of a HS machine requires that multiple design issues be reviewed simultaneously [5]. In many applications, mechanical stresses limit the performance of the HS electrical machine, and thus HS topologies are sometimes defined by the mechanical and thermal limitations.

It is not generally possible to use a standard structure and each machine needs to be designed according to the specific requirements of the application. Consequently, the design process of a HS machine involves several steps prior to construction of the first prototype. Arkkio *et al.* [6] proposed a design methodology for high-speed induction machines (HSIM) and high-speed permanent magnet synchronous machines (HS PMSM). However, the methodology did not include rotordynamics analysis. An improved design methodology was implemented in [7] to define the maximum power and speed limits for a HS PMSM. Ranft [8] proposed a design methodology chart for HSIM but did not include thermal analysis in the methodology. Cheng *et al.* [9] proposed a design flow chart for HS PMSM with the full cylindrical magnet in the rotor. However, the flow chart included only electrical and mechanical design, and the thermal analysis was done separately. Bernard *et al.* [10] proposed a design flow and analytical optimization for PMSM with a gearbox. The design flow was for a screwdriver application with infinite stiff supports, which limits its implementation for HS machinery. Although, several design methodologies are presented in the literature, none of them proposes a comprehensive multidisciplinary design process for HS applications that includes electrical, mechanical and thermal analyses.

To limit the number of possible options, the design methodology presented in this paper was developed for a specific type

Manuscript received April 16, 2015; revised June 16, 2015; accepted August 9, 2015.

N. Uzhegov, J. Nerg, and J. Pyrhönen are with the Department of Electrical Engineering, LUT Energy, School of Energy Systems, Lappeenranta University of Technology (LUT), 53851 Lappeenranta, Finland (e-mail: nikita.uzhegov@lut.fi; janne.nerg@lut.fi; juha.pyrhonen@lut.fi).

E. Kurvinen and J. Sopanen are with the Department of Mechanical Engineering, School of Energy Systems, Lappeenranta University of Technology (LUT), 53851 Lappeenranta, Finland (e-mail: emil.kurvinen@lut.fi; jussi.sopanen@lut.fi).

S. Shirinskii is with the Institute of Electrical Engineering, Moscow Power Engineering Institute, 111250 Moscow, Russia (e-mail: shirinskiisv@gmail.com).

This article has been accepted for publication in a future issue of this journal, but has not been fully edited. Content may change prior to final publication. Citation information: DOI 10.1109/TIE.2015.2477797, IEEE Transactions on Industrial Electronics

of HS electrical machine. The machines under consideration have 6 stator slots and 2 poles, which in a three phase machine result in the number of slots per pole and phase, $q = 1$. The machines utilize tooth-coil (TC) windings to have the shortest possible overall length of a 2-pole machine. This, naturally, leads to a shorter rotor total length, which, in turn, expands the mechanical boundaries with respect to critical speeds. With a shorter rotor, the lowest flexible natural frequencies of the rotor will be higher and, as a result, the machine operates below critical speed, enabling still higher operational speeds.

The design process is explained and applied to two machines. The developed prototypes use different approaches within the scope of the presented design methodology. The first machine under consideration is a 3.5 kW, 45000 rpm PMSM for a gas blower application. In this machine, expensive materials are selected to reduce losses and ensure mechanical rigidity and acceptable temperatures. The second machine is a permanent magnet (PM) generator with a rated operating point of 11 kW at 31200 rpm. The machine works as a generator in a micro Organic Rankine Cycle (ORC) power plant. The machine has the same topology as the first machine but utilizes inexpensive materials. To reduce high losses, alternative geometry optimization solutions are implemented in the second machine.

The developed prototypes are built and tested. The machines' performance calculation results are compared to test results and conclusions are drawn regarding the suitability of the design methodology for other types of HS electrical machines.

The main contribution of the paper is to propose a multi-disciplinary design process for a PMSM consisting of six stator slots and two poles as well as a diametrically magnetized permanent magnet and a tooth-coil wound stator in high-speed applications. Even though the proposed design procedure is intended for the aforementioned PMSM type, it can be applied, with slight modifications, to other electrical machine types.

II. Design Process

The design process of a HS machine involves several steps prior to construction of the first prototype. Fig. 1 shows a general design flow chart for a HS PMSM. The design process is divided into 9 steps. These steps are tasks for engineers and all have input and output design variables. Each of the steps should yield results that satisfy the design requirements (Step 1). The flow chart has six decision points where the fulfilment of the requirements list is verified. If the requirements are not met, then a new iteration round is required. Each step creates additional information and introduces further requirements, e.g. in Step 2 a maximum shaft diameter can be evaluated from the initial requirements. If all the requirements are fulfilled, the process can proceed to the next step, otherwise the design should be changed until satisfactory results are achieved. In Fig. 1 the proposed actions to satisfy the additional requirements are shown on the right side. When all of the steps are completed and the design requirements are fulfilled, the first prototype can be built.

The design process of an electric machine is thus a highly iterative process and, for that reason, many concepts need to

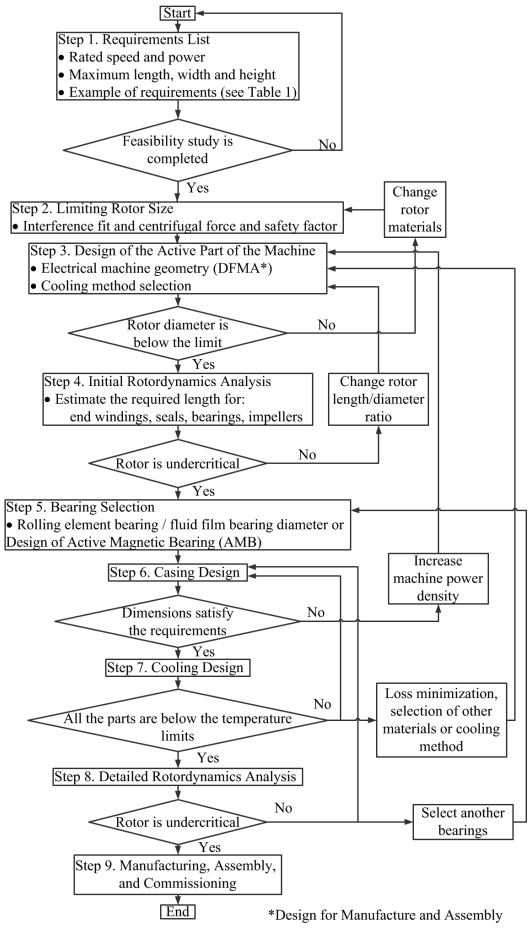

Fig. 1. Design flow chart for a high-speed permanent magnet synchronous machine

be analyzed before the final solution is found. The required calculations can first be done with analytical electromagnetic, thermal and structural analyses in order to constrain the dimensions. The constrained dimensions can then be used as a starting point in subsequent steps. Finite Element Method (FEM) analysis can be used in the verification or to study the structure in more detail.

The proposed design process is specially developed and tested for a HS PMSM having 6 slots and 2 poles. The decision to consider a specific type of machine was made in order to limit the machine topology design variations, simplify the initial design stage and concentrate on the special features of the proposed machine topology. The selected electrical

This article has been accepted for publication in a future issue of this journal, but has not been fully edited. Content may change prior to final publication. Citation information: DOI 10.1109/TIE.2015.2477797, IEEE Transactions on Industrial Electronics

machine topology is justified with the following reasons.

Firstly, one of the boundary conditions of the design was reasonable manufacturing costs. This was taken into account in the design flow. The topology with the lowest possible slot number allows, in principle, cost effectiveness in manufacturing. Noguchi *et al.* [11] compared a 3-slot motor to a 6-slot motor with TC windings for a HS application. According to their results, a 3-slot motor has high unbalanced forces and higher rotor losses compared to a 6-slot motor. Consequently, a 6-slot stator was selected for both high-speed machines developed in this work. Secondly, the machines have two poles and, thereby, the iron losses are lower compared to solutions with a higher number of poles at the considered operational frequencies. Finally, TC windings were selected to achieve a reasonable solution for short end windings axial protrusion length.

Tooth-coil windings may be criticized in this kind of application because the fundamental winding factor is greatly reduced by the very narrow winding step. Actually, the winding factor is only $k_{w1} = 0.5$, while in the case of a full pitch $q = 1$ winding it is $k_{w1} = 1$. However, in HS machines the number of winding turns is often so low that doubling them does not significantly harm machine performance. Indeed, the amount of copper can be about the same in TC windings and full pitch windings as the full pitch winding ends are so long compared to the compact end windings in the case of TC windings. However, even if copper losses increase due to the higher number of turns, their share in the total loss distribution is negligible compared to other losses, as will be shown later. Iron and rotor losses are increased with TC windings due to the higher air gap harmonic content compared to distributed windings. An alternative solution which enables short end windings axial protrusion length is Gramme ring windings [12].

The 9 design steps (Fig. 1) are explained in detail in the following subsections.

A. Step 1. Requirements List

The requirements list contains all the requirements and wishes that the final product should and could fulfill. At the beginning of the design process, several parameters and values need to be defined in order to achieve fluent design flow. The requirements list can be updated after each step, for example, when the maximum rotor diameter has been defined. Table I shows an example of a requirements list. In addition to electrical, mechanical and thermal information of the type shown in Table I, the requirements list should include other information such as sealing information and requirements originating from applicable industrial standards, for example, the required degree of protection against intrusions in the casing.

After the design engineers have studied the requirements list they have to prepare the specification. The specification must be based on a system feasibility study. In the specification, extra technical information regarding the system may be added. When the feasibility study has been completed, it is possible to move to Step 2.

TABLE I. EXAMPLE OF REQUIREMENTS LIST

Requirement/Wishes	Requirement	Wish
Rated speed	31 200 rpm	-
Nominal power	11 kW	-
Efficiency at nominal point	> 90 %	> 95 %
Axial length	< 150 mm	< 130 mm
Bearing type	Ball bearing	-
Mechanical safety factor	2.0	-
Thermal class	155	120
Cooling method	Liquid	-
Rotor material	Austenitic steel	-
Rotordynamics	Undercritical	-
IP class	IP55	-
Manufacturing price per unit	$< 25\,000$ EUR	$< 15\,000$ EUR
Maintenance period	2 years	-

It should be noted that the magnet material was not defined in the requirements list for the prototypes in this study. Information about the PM material is required to set the maximum shaft diameter in Step 2. If the magnet material is not defined in the requirements list, the next step could be evaluation with commonly used neodymium (NdFeB)- and samarium-cobalt (SmCo) magnets. Further, in Step 3 the required thermal class directly affects the magnet material selection.

B. Step 2. Limiting Rotor Size

The aim of the second step is to determine the limits on rotor size for rotation at the nominal speed with a required safety factor. As the rotation speed increases, the centrifugal force creates greater stresses on the structure and the maximum diameter can be determined based on the properties of the used material. In the proposed design process, a rotor structure with a full cylindrical magnet and a retaining sleeve is implemented. Fig. 2 illustrates the cross-section of the rotor structure.

In most cases, the sleeve material used should be austenitic steel or another non-magnetic material to avoid PM flux leakage and additional eddy-current losses. Contact between the magnet and sleeve should be maintained at all times. In practice, this means that the interference fit should be maintained for all operation conditions, while simultaneously ensuring a large enough safety margin relative to the yield strength of the material.

The permanent magnet material is affected by the expansion of the centrifugal forces and in the case of SmCo material the temperature increase. NdFeB permanent magnet material has a negative thermal expansion coefficient perpendicular to the magnetization direction, which causes magnet contraction

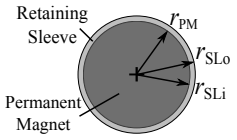

Fig. 2. Rotor structure with the dimensions used in the shrink fit calculation

This article has been accepted for publication in a future issue of this journal, but has not been fully edited. Content may change prior to final publication. Citation information: DOI 10.1109/TIE.2015.2477797, IEEE Transactions on Industrial Electronics

as the rotor temperature rises. The sleeve is affected by the expansion due to the centrifugal forces and increasing temperature [13].

The total expansion of the magnet and the sleeve ($\varepsilon_{\mathrm{PM}}$ and $\varepsilon_{\mathrm{SL}}$) can be calculated by considering the expansion due to rotation speed ($\varepsilon_{\mathrm{PM}\Omega}$ and $\varepsilon_{\mathrm{SL}\Omega}$) together with the expansion due to thermal expansion ($\varepsilon_{\mathrm{PMtemp}}$ and $\varepsilon_{\mathrm{SLtemp}}$) as:

$$\begin{aligned}\varepsilon_{\mathrm{PM}}(r) &= \varepsilon_{\mathrm{PM}\Omega}+\varepsilon_{\mathrm{PMtemp}}\\ &= \tfrac{3+\nu_{\mathrm{PM}}}{8}\rho_{\mathrm{PM}}\Omega^2\tfrac{1-\nu_{\mathrm{PM}}}{E_{\mathrm{PM}}}r\left[{r_{\mathrm{PM}}}^2-\tfrac{1+\nu_{\mathrm{PM}}}{3+\nu_{\mathrm{PM}}}r^2\right]+\ \alpha_{\mathrm{PM}}r\Delta T\ ,\\ \varepsilon_{\mathrm{SL}}(r)\ &= \varepsilon_{\mathrm{SL}\Omega}+\varepsilon_{\mathrm{SLtemp}}\\ &= \tfrac{3+\nu_{\mathrm{SL}}}{8}\rho_{\mathrm{SL}}\Omega^2\tfrac{1-\nu_{\mathrm{SL}}}{E_{\mathrm{SL}}}r\\ &\quad\left[r_{\mathrm{SLi}}^2+r_{\mathrm{SLo}}^2-\tfrac{1+\nu_{\mathrm{SL}}}{3+\nu_{\mathrm{SL}}}r^2+\tfrac{1+\nu_{\mathrm{SL}}}{1-\nu_{\mathrm{SL}}}\tfrac{r_{\mathrm{SLi}}^2r_{\mathrm{SLo}}^2}{r^2}\right]+\ \alpha_{\mathrm{SL}}r\Delta T\ ,\end{aligned} \tag{1}$$

where r is the radius from the center from which the expansion is calculated, subscripts PM and SL refer to the magnet and sleeve respectively, ν is the Poisson's ratio of the given material, ρ is the material density, Ω is the rotation speed, E is the modulus of elasticity, r_{PM} is the magnet radius, r_{SLi} is the sleeve inner radius and r_{SLo} is the sleeve outer radius, α is the thermal expansion coefficient, and ΔT is the temperature difference from room temperature. The temperature value is selected close to the permanent magnet material operation limit to ensure reliable operation at critical conditions. The temperature is updated after the detailed thermal analysis is performed in Step 7 and the next design iteration begins. The dimensions are shown in Fig. 2.

In a HS PMSM the magnet and sleeve should be fixed in a way that the produced torque is transmitted to the rotor shaft. This is usually done by manufacturing the sleeve smaller than the magnet outer diameter and utilizing the temperature difference to install the sleeve over the magnet, so-called shrink fit or interference fit. The interference fit between the magnet and sleeve should be selected so that neither the yield strength of the magnet nor the sleeve are exceeded, nor the maximum temperature of the permanent magnet. The dynamical interference fit, λ, can be calculated by considering the total expansion calculated in (1) and reducing that amount from the designed static interference fit, $\varepsilon_{\mathrm{sinterf}}$, amount as $\lambda=\varepsilon_{\mathrm{PM}}+\varepsilon_{\mathrm{SL}}-\varepsilon_{\mathrm{sinterf}}$. The dynamic contact pressure between the magnet and the sleeve, p_{c}, can be calculated as:

$$p_{\mathrm{c}}=\frac{\lambda r_{\mathrm{PM}}E_{\mathrm{PM}}E_{\mathrm{SL}}(r_{\mathrm{PM}}^2-r_{\mathrm{SLo}}^2)}{\left(\left(r_{\mathrm{PM}}^4-r_{\mathrm{PM}}^2r_{\mathrm{SLo}}^2\right)\nu_{\mathrm{SL}}-r_{\mathrm{PM}}^4-r_{\mathrm{PM}}^2r_{\mathrm{SLo}}^2\right)E_{\mathrm{PM}}+\left(\left(-r_{\mathrm{PM}}^4+r_{\mathrm{PM}}^2r_{\mathrm{SLo}}^2\right)\nu_{\mathrm{PM}}+r_{\mathrm{PM}}^4-r_{\mathrm{PM}}^2r_{\mathrm{SLo}}^2\right)E_{\mathrm{SL}}}. \tag{2}$$

The stresses due to the rotation speed, thermal effect and pressure from the interference fit are highest at the contact point between the magnet and sleeve. Tangential (t) and radial (r) stresses can be calculated as a function of r based on the contact pressure, rotation of the magnet and sleeve as:

$$\begin{aligned}\sigma_{\mathrm{rc}} &= \tfrac{r_{\mathrm{SLi}}^2p_{\mathrm{c}}-r_{\mathrm{SLo}}^2p_{\mathrm{o}}}{r_{\mathrm{SLo}}^2-r_{\mathrm{SLi}}^2}-\tfrac{r_{\mathrm{SLi}}^2r_{\mathrm{SLo}}^2(p_{\mathrm{s}}-p_{\mathrm{o}})}{r^2(r_{\mathrm{SLo}}^2-r_{\mathrm{SLi}}^2)},\\ \sigma_{\mathrm{tc}} &= \tfrac{r_{\mathrm{SLi}}^2p_{\mathrm{c}}-r_{\mathrm{SLo}}^2p_{\mathrm{o}}}{r_{\mathrm{SLo}}^2-r_{\mathrm{SLi}}^2}+\tfrac{r_{\mathrm{SLi}}^2r_{\mathrm{SLo}}^2(p_{\mathrm{s}}-p_{\mathrm{o}})}{r^2(r_{\mathrm{SLo}}^2-r_{\mathrm{SLi}}^2)},\\ \sigma_{\mathrm{rPM}\Omega} &= \tfrac{3+\nu_{\mathrm{PM}}}{8}\rho_{\mathrm{PM}}\Omega^2[r_{\mathrm{PM}}-r^2],\\ \sigma_{\mathrm{tPM}\Omega} &= \tfrac{3+\nu_{\mathrm{PM}}}{8}\rho_{\mathrm{PM}}\Omega^2[r_{\mathrm{PM}}-\tfrac{1+3\nu_{\mathrm{PM}}}{3+\nu_{\mathrm{PM}}}r^2],\\ \sigma_{\mathrm{rSL}\Omega} &= \tfrac{3+\nu_{\mathrm{SL}}}{8}\rho_{\mathrm{SL}}\Omega^2[r_{\mathrm{SLi}}^2+r_{\mathrm{SLo}}^2-r^2-\tfrac{r_{\mathrm{SLi}}^2r_{\mathrm{SLo}}^2}{r^2}],\\ \sigma_{\mathrm{tSL}\Omega} &= \tfrac{3+\nu_{\mathrm{SL}}}{8}\rho_{\mathrm{SL}}\Omega^2[r_{\mathrm{SLi}}^2+r_{\mathrm{SLo}}^2-\tfrac{1+3\nu_{\mathrm{SL}}}{3+\nu_{\mathrm{SL}}}r^2+\tfrac{r_{\mathrm{SLi}}^2r_{\mathrm{SLo}}^2}{r^2}],\end{aligned} \tag{3}$$

where p_{o} is the pressure in the electrical machine (air). Using the superposition theorem, the radial and tangential stresses in the sleeve can be summed into $\sigma_{\mathrm{rtot}}=\sigma_{\mathrm{rc}}+\sigma_{\mathrm{rSL}\Omega}$ and $\sigma_{\mathrm{ttot}}=\sigma_{\mathrm{tc}}+\sigma_{\mathrm{tSL}\Omega}$, and the VonMises stress can then be calculated as $\sigma_{\mathrm{vmises}}=\sqrt{\sigma_{\mathrm{ttot}}^2-\sigma_{\mathrm{ttot}}\sigma_{\mathrm{rtot}}+\sigma_{\mathrm{rtot}}^2}$ [14].

C. Step 3. Design of the Active Part of the Machine

Once the maximum rotor outer diameter has been defined, electromagnetic design can be commenced. Based on the requirements list and stress analysis information, the initial rotor diameter and length are calculated. The length/diameter ratio, χ, is a parameter that strongly affects the final machine design performance because the electrical machine rotor length influences the rotordynamics and the rotor diameter influences the mechanical losses [15].

It is important to remember at this stage that the actual rotor length in a PM machine must be selected such that it is longer than in a machine with winding-created current linkage. To utilize the armature optimally and to avoid performance drop, the PM length, l_{PM}, should be selected as $l_{\mathrm{PM}}\approx l+2\delta_{\mathrm{e}}$. Where l is the physical length of the stator stack and δ_{e} is the magnetic air gap length [16]. In other words, the PM rotor length must be at least two magnetic air gaps longer than the stator core length.

The analytical electromagnetic design process follows the procedure described in [13]. The different optimization techniques for PMSMs can be found in [17]. During the machine electromagnetic design, the stator and the rotor are calculated simultaneously. The stator part itself is not critical in the further rotordynamics analysis. However, the end windings axial protrusion length will affect the total rotor length and the rotordynamics.

The materials are defined at this stage. The selection of the materials is closely connected to the electrical machine design. The influence of the material selection on the design process is shown with the examples of the developed prototypes in Section III-A. The materials can be changed to meet the requirements, as shown in Fig. 1.

After the machine electromagnetic design has been verified by FEM, the machine parameters are grouped and are sent to the relevant steps for further design and analysis. The stator dimensions and materials selection are transferred to Step 6 for the casing design. The information about the rotor materials

This article has been accepted for publication in a future issue of this journal, but has not been fully edited. Content may change prior to final publication. Citation information: DOI 10.1109/TIE.2015.2477797, IEEE Transactions on Industrial Electronics

and dimensions is sent to the next step, Step 3, for simulation of the dynamic behaviour of the full rotor.

A preliminary decision about the cooling method is made during the electromagnetic design. The calculated machine losses are then sent to Step 7 for detailed cooling analysis.

Manufacturing and assembly limitations must be taken into account during the electromagnetic design to avoid extra iteration steps. These limitations are, for example, fixtures on the outer diameter of the stator.

Once the electromagnetic design of a HS machine is ready, it must be verified that the rotor diameter is below the given limit. If it is not possible to design the electrical machine within the limitation calculated in Step 2, other rotor materials must be selected. In this case, Steps 2 and 3 must be repeated.

D. Step 4. Initial Rotordynamics Analysis

The aim of the initial rotordynamics analysis is to determine the feasibility of the proposed structure. At this point, the maximum diameter and length of the rotor of the electrical machine are known. The length and diameter of the other parts of the rotor, such as end windings, seals, bearings and attachments to the rotor, e.g. impellers, should be approximated. The added mass and inertia of the impellers or couplings as well as the connection method should be known to enable accurate prediction of the dynamic behavior. When the conceptual rotor is known, the model can then be built and analyzed. The operational speed of the electrical machine is known from the requirements list, so rotor performance in that speed region can be evaluated. As a rule of thumb, the critical speeds should be ± 15 % from the operational speed to guarantee good performance [18]. If the results are unsatisfactory, for example, the rotor is above the first critical frequency at the operational point, the length/diameter ratio can be modified and Steps 2 and 3 repeated. It is also possible to operate above the critical frequencies, but greater demands are then placed on the bearings in order to pass the critical frequency.

The developed prototypes utilize a TC windings configuration. Fig. 3 shows the effect of TC windings and distributed windings (DW) on the rotor structure. The top part of Fig. 3 shows the original structure used in the critical speed map analysis shown in Fig. 4. This rotor design is possible when TC windings are implemented, due to the shorter end windings protrusion length in 2-pole machines.

The bottom part of Fig. 3 shows the 50% longer center part structure used in the critical speed map analysis shown in Fig. 4. This longer rotor structure is an excessive result of utilizing conventional DW. The end windings axial protrusion length is about 50% greater than with TC windings as shown in [19]. Moreover, with DW there is uncertainty in the final end windings protrusion length because of manufacturing aspects. The longer rotor represents the case where the end windings require more space than assumed in the initial analysis. Practically, the longer the rotor the lower are the critical speeds. A rotor that requires high critical speeds has to be short. Short design also leads to a smaller and lighter machine, which is usually a desired feature.

A critical speed map for the example structures in Fig. 3 is shown in Fig. 4. Use of a critical speed map is a clear way to see the relationship of the support stiffness to the critical speeds. The horizontal axis in the figure gives the support stiffness and the vertical axis shows the critical speeds. Supports in the rotors are usually bearings and selection of the bearing topology enables a specific stiffness to be achieved. The critical speed map is calculated without damping at zero rotation speed and thus it does not consider the gyroscopic effect. Knowledge of the approximated critical speed permits the general rotor-support behavior to be determined. The solid lines refer to the TC structure and the dashed lines to the structure in which the largest diameter part of the shaft is 50% longer. The vertical lines represent typical bearing stiffnesses with different bearing topologies. Magnetic bearings have a stiffness value of $1 \cdot 10^6$ N/m, journal bearings $5 \cdot 10^7$ N/m, and ball bearings $1 \cdot 10^8$ N/m. The bearing stiffness margin in Fig. 4 is $\pm$ 10% and the given values are in the radial direction.

Fig. 4 shows that increasing the length of the rotor leads to lower critical speeds. For example, with ball bearings the achievable stiffnesses are in range of $1 \cdot 10^8$ N/m. With TC windings, the first critical speed is 70 000 rpm, the second 72 000 rpm and the third 145 000 rpm. If the active part length is increased by 50% because of the distributed windings, the first critical speed drops to 35 000 rpm, the second to 71 000 rpm, and the third to 100 000 rpm. In this case, the first and the third critical speeds have the biggest change when the length is increased as the second critical speed is almost the same with both models. By extension of the active part length,

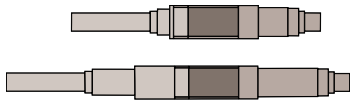

Fig. 3. Rotor structure for tooth-coil winding machine (top) and 50 % longer middle part for a full pitch distributed winding machine (bottom).

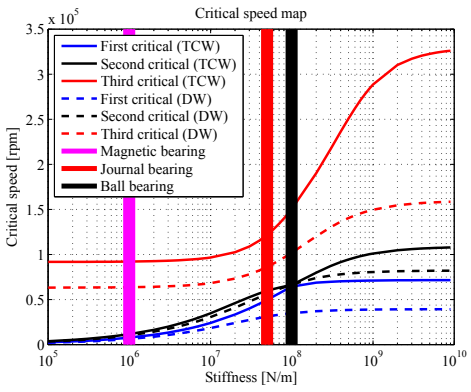

Fig. 4. Critical speeds with TC winding structure (solid lines) and with the 50% longer DW structure (dashed lines).

This article has been accepted for publication in a future issue of this journal, but has not been fully edited. Content may change prior to final publication. Citation information: DOI 10.1109/TIE.2015.2477797, IEEE Transactions on Industrial Electronics

the first critical speed is reduced to half that of the original structure. For undercritical operation with 20% safety margin the machine with TC windings could be driven at the rated speed of 56 000 rpm and the machine with DW at the rated speed of 28 000 rpm.

E. Step 5. Bearing Selection

The bearing selection step is related to the previous step in which the feasibility of the rotordynamics was determined. The most commonly used bearing types are explained here and special parameters related to such bearings are determined.

The most commonly used bearing type are rolling element bearings such as ball and spherical roller bearings. This type of bearing is used in low and medium speed rotating machines. These bearings have the highest stiffness, as can be seen in Fig. 4 (black vertical line). As the rotation speed increases the centrifugal forces push the rolling elements to the outer ring and the stiffness at the center of the bearing consequently decreases [20]. With high-speed operations, this topology requires special design, and lightweight rolling elements should be used, e.g., ceramic silicon nitride balls. Ceramic balls offer the additional benefit of prevention of bearing currents. Rolling element bearings are a passive type of bearing and variation in the bearing properties depends on the installation process.

Fluid film bearings are used when higher damping and higher rotation speed are required. Very high rotation speeds can be achieved with this type of bearing due to the discontinuity between the pads. Tilted bearing pads can be used to give better damping. The stiffness achieved with this type of bearing is lower than with ball bearings, which affects the operational range, as can be seen in Fig. 4 [21].

Active Magnetic Bearings (AMBs) generally have lower stiffness values than ball or journal bearings. However, they enable active control of the stiffness and damping values. Because there is no mechanical contact between the rotor and the bearing, this type of bearing can be used in high-speed applications. The maximum speed is limited by the stress on the electrical lamination sheets that are required on the shaft at the radial bearing location or by the bandwidth of the control system. Very-high-speed solutions with AMBs have been reported in [22], [23].

Despite the many advantages of AMBs, such as low friction, cleanliness, the possibility of actively controlling the rotordynamics, etc., these bearings bring also significant design challenges as they need extra length and add to the mass of the rotor causing, therefore, easily exacerbating problems with rotordynamics. AMBs may allow supercritical speeds but naturally the control challenges are then emphasized. AMBs, in principle, allow the highest speeds but require the longest rotor. Shorter rotors permit higher critical speeds and can be made with traditional ball bearings but do not allow high speeds. Fluid film bearings are widely used. The space needed for these bearings is fairly low but the bearings generate high losses and naturally the lubricating system needed increases the complexity of the fluid bearing systems.

F. Step 6. Casing Design

The casing provides support for the rotating part and protects the inner part of the machine from the environment. All the requirements given in Step 1, such as cooling concept, electrical connections and measurement connections (temperature, pressure etc.) should be met in the casing design step.

In Step 4, the initial rotordynamics analysis is performed with an assumption of rigid support as it has not been defined at that point. When the casing is known, its stiffness can be calculated with structural FEM software. Study by Nicholas and Barrett [24] shows that the casing stiffness influences the rotor's dynamical performance by lowering the critical speeds. Thus, a rotordynamic model that includes bearing support stiffness will predict the actual critical speeds more accurately.

The clearance required for the seals between the different parts should be considered for the operating temperature range. However, as the cooling is not yet fixed, a couple of design loops exist between the casing design (Step 6) and cooling design (Step 7).

The casing dimensions must be below the values specified in the requirements. If the outer dimensions exceed the limits, the power density of the machine must be increased in Step 3. Any power density increase must be taken into account from the cooling system design point of view.

G. Step 7. Cooling Design

The results from the previous steps are utilized in the cooling design to ensure that the machine operating temperature remains low enough for safe operation. The main input parameters of the cooling design are the dimensions of the machine and the materials used, including information about the shrink fits, rotation speed, losses (electromagnetic and mechanical losses) and allowed temperature rise. The most common cooling method in HS electrical machinery is forced air cooling, where an additional blower or a shaft mounted blower are utilized to create sufficient cooling air flow to remove heat from the interior parts of the machine. In addition to forced air cooling, liquid cooling solutions are also widely used in industrial applications. In its simplest form, liquid cooling involves the machining of cooling channels into the frame tube above the stator stack. The heat is transferred mostly by thermal conduction from the inner parts of the machine to the liquid cooled frame tube in the radial direction through the stator iron. Combinations of forced air and liquid cooling methods also exist [25]. A comprehensive state-of-the-art survey of cooling solutions for high-speed electrical machines can be found e.g. in [26].

In order to select the most cost efficient cooling method, thermal analysis of the electrical machine is needed. The result of the thermal analysis is the temperature distribution of the machine structure at a given volumetric cooling fluid flow rate. The volumetric cooling fluid flow rate needed and the total pressure drop in the cooling channel constitute the basis of the blower or pump selection.

Thermal analysis can be done utilizing lumped parameters, FEM or computation fluid dynamics (CFD). In most cases, lumped parameter based thermal analysis is accurate enough

This article has been accepted for publication in a future issue of this journal, but has not been fully edited. Content may change prior to final publication. Citation information: DOI 10.1109/TIE.2015.2477797, IEEE Transactions on Industrial Electronics

and in terms of required computational time is the best option for practical design purposes [27], [28]. The results of the lumped parameter based analysis are the maximum and average values of the temperature in the stator windings, stator core, PM and rotor sleeve, which will then be compared with the acceptable values. The pressure drop within the cooling fluid flow passages can be analytically calculated utilizing the calculated cooling fluid flow rate and the dimensions of the cooling fluid flow passages.

If at this step the calculated temperatures are higher than the selected materials can tolerate, changes are required at the electromagnetic design stage, Step 3. This problem can be approached in several ways: an alternative cooling method capable of dissipating more heat could be proposed or the machine type or topology changed. A less radical solution might be via loss minimization, which can usually be achieved through the use of different materials, by implementing structural changes, or via geometry optimization.

H. Step 8. Detailed Rotordynamics Analysis

The conceptual rotordynamics was calculated in Step 4 and the conceptual suitability determined. In Step 4 the support was assumed to be attached to rigid ground. At this point, more details can be implemented to the rotordynamic analysis, for example, more detailed casing stiffness (initially considered in Step 6) can be included in the analysis.

Cooling design requirements and tolerances for the seals can be included in the rotordynamics analysis. In Step 4 the seals were conceptual. Additional features that require modifications to the shaft should also be included in the detailed rotordynamics analysis, for example, shoulders for the sensors, fixture holes and shoulders for the seals (e.g. labyrinth seals). The dynamic behaviour of the rotor can be studied as it grows or shrink during operation (sensitivity analysis). This is essential if the rotor is very long, and also if seals are used.

I. Step 9. Manufacturing, Assembly, and Commissioning

At this point, many design constraints have already been set and the structure can be considered as fulfilling the requirements list. The design details now need to be transferred to the manufacturing drawings. In this step it would be beneficial to know what tools are available in the manufacturing workshop in order to avoid special machining (which is usually more costly). Some parts such as the casing should be separated into sections so that they can be manufactured and assembled easily [29]. The aim is to use as many stock sized parts as possible as they are reasonable priced and do not require long machining times.

At the manufacturing stage, the devices required are detailed and arrangements and reservations made for their use. Any special tools that might be required should be designed at this point. Examples of such tools are different kinds of jigs to temporarily hold parts in place until the final attachment is completed. The required sensors and controls can also be ordered (and designed) at the beginning of the prototype manufacturing process.

One of the first activities in the commissioning step is to check the requirements list in Step 1 for special tests that might be needed. In every case, however, the cooling method, rotor and electric machine should be tested to ensure that they fulfil the design requirements and have the required performance. The rotor can be tested before assembly with Experimental Modal Analysis (EMA). EMA reveals the free-free natural frequencies, which can be compared to the rotordynamics model used in the analyses. The model can then be modified to agree more accurately with the actual rotor performance. It should be noted that in high-speed rotors there is always variation in the natural frequencies of each rotor due to manufacturing imperfections and differences in fittings and tolerances of the complete rotor assembly.

III. CASE STUDIES

All the steps of the design flow (Fig. 1) were applied to two HS PMSMs. The features of the designed electrical machines that affect the design flow are described in this section.

The designed prototypes under examination have similar electrical machine topology. Fig. 5 illustrates the topology of the 3.5 kW and the 11 kW PMSM respectively. In both cases, the rotor consists of a full cylindrical magnet, which is diametrically magnetized.

The PM is inserted inside the retaining sleeve using a shrink fit method in which the sleeve is heated and the cold magnet inserted inside. The magnet is made of one piece and the retaining sleeve materials in both machines are non magnetic; therefore, no additional forces affect the PM during the installation into the sleeve.

Sintered PM materials are well suited for this kind of installation as they have high pressure tolerance. It must, however be borne in mind that the temperatures in the magnet material must remain low enough during the rotor assembly not to affect the material magnetization. Without special arrangements the magnet is, in principle, in air during this work and its flux density is, therefore, very low. This may be critical if the sleeve temperature is high and heat is transferred to the magnet material after sliding it into the sleeve. This installation phase must be studied by FEA and the stresses caused compared to

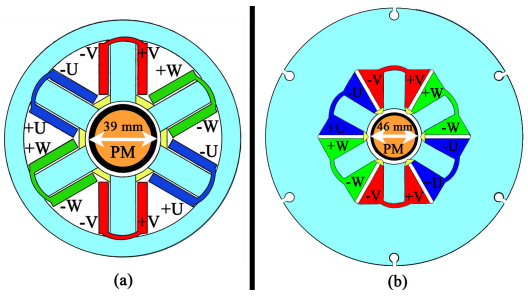

Fig. 5. (a) 3.5 kW High-Speed Permanent Magnet Synchronous Motor geometry, (b) 11 kW High-Speed Permanent Magnet Synchronous Generator geometry

This article has been accepted for publication in a future issue of this journal, but has not been fully edited. Content may change prior to final publication. Citation information: DOI 10.1109/TIE.2015.2477797, IEEE Transactions on Industrial Electronics

TABLE II. DESIGNED MACHINES MECHANICAL STRESSES

Machine parameter	3.5 kW PMSM	11 kW PMSM
Shrink fit λ, mm	0.014	0.017
Temperature T, °C	120	120
Maximum stresses at contact boundary		
Radial stress σ_r, MPa	-21	-4
Tangential σ_t, MPa	162	70
von Mises σ_{vmises}, MPa	174	72
Safety factor to yield strength	5.0 (880 MPa)	2.8 (205 MPa)

the J,H-chart of the PM material. As a remedy this phase can also be realized inside a ferromagnetic special steel tube tool to enable higher flux density before cooling the rotor.

A. Materials

Although the two machines under consideration have similar topology the parts are made of different materials. The material selection of the retaining sleeve affects the overall high-speed machine design, especially with a hollow shaft constructions. The sleeve has to tolerate stresses from the centrifugal forces, and boundary surface contact between the PM and the sleeve must exist throughout the machine operation [30]. In addition, in configurations with hollow shaft, the torque is transferred through the retaining sleeve only.

In both machines in this study, the magnet retaining sleeves are made of an electrically conductive material and rotor losses due to eddy-currents will therefore exist. With skillful design these losses do not usually lead to a significant efficiency drop [31]. Nevertheless, if heat dissipation from the rotor is poor, the sleeve eddy-current losses could cause irreversible demagnetization of the PM because of direct heating of the magnet. Thus, material electromagnetic properties place some restrictions on selection of the material of the magnet retaining sleeve. Study of different sleeve materials for HS applications can be found, for instance, in [32].

A titanium retaining sleeve was selected for the 3.5 kW PMSM. Titanium, for example Ti-6AL-4V, has exceptional mechanical properties and its conductivity is equal to $5.8 \cdot 10^5$ S/m, which is 70 % lower than stainless steel conductivity. Austenitic stainless steel AISI 316L was selected as the retaining sleeve material for the 11 kW generator. This material has higher conductivity and 77 % less yield strength than Ti-6AL-4V. However, the price of the material is lower and it is widely available.

The mechanical stresses exerted in the rotor at the magnet-sleeve area are presented in Table II. The highest stresses occur between the boundary of the magnet and sleeve. Maximum interference is utilized in the analysis. The sleeve is required to be under compression (negative value) to the magnet in order to transfer the produced torque. The stresses were studied at the rated speed.

The PM material is SmCo in both prototypes. The key reasons for selection of a SmCo PM were the eddy-current losses in the magnet retaining sleeve and the compact design of the whole system. The impeller works close to the PM and its working temperature is above 260°C. SmCo can tolerate higher temperatures than other PM materials and, as a consequence, the machine has a higher possible operating temperature without the risk of an irreversible demagnetization. The drawback of this material is the higher cost.

TABLE III. MAIN PARAMETERS OF THE DESIGNED MACHINES

Machine parameter	3.5 kW PMSM	11 kW PMSM
Rated speed n_n, min^{-1}	45000	31200
Number of poles p	2	2
Number of stator slots Q_s	6	6
Rated torque T_n, Nm	0.74	3.36
Rotor outer diameter D_o, m	0.039	0.046
Physical air-gap legth δ, m	0.002	0.003
External diameter D_e, m	0.140	0.242
Active length l, m	0.022	0.060
Permanent magnet material	SmCo	SmCo
Permanent magnet remanence B_r, T	1.10	1.12
Stator stack lamination material	NO10	M-270-35A
Retaining sleeve material	Titanium	Stainless steel
Magnetic wedges material	Spindurol	Magnoval 2067
Bearing type	Magnetic bearing	Ball bearing

The key parameters of the designed machines are given in Table III. The stack lamination material is NO10 for the 3.5 kW machine. This material has low per unit losses and its thickness is 0.1 mm. These factors reduce the iron losses, but the stack space factor is only 0.93. M-270-35A steel was selected for the 11 kW PMSM stator stack. Compared to NO10 it has higher per unit losses at high frequencies and the thickness is equal to 0.35 mm, which together increase the iron losses. The benefits of the material are its easy availability and low price with respect to the NO10. In both machines, the lamination sheets were laser cut.

Magnetic wedges were inserted between the tooth tips in both machines. Utilization of magnetic wedges decreases the slot harmonics in the air gap, which, in turn, reduces rotor eddy-current losses. Spindurol, which was used for the 3.5 kW machine, has a relative permeability of 2.4 at 0.7 T. The 11 kW generator has Magnoval 2067 wedges between the tooth tips. This material has a relative permeability of 2.9 at 0.7 T. Rotor loss reduction in the 11 kW PMSM due to the magnetic wedges is presented in [33].

B. Geometry

Geometry optimization is required to minimize losses. The designed machines have different loss minimization approaches and, therefore, $\chi = 0.55$ in the 3.5 kW machine and $\chi = 1.3$ in the 11 kW machine. The length/diameter ratio dictates the proportion of active (in slots) and passive (end windings) copper in the stator.

The increased magnetic air gap limits the flux density variations due to both slot and current linkage harmonics [34], [35]. With the non-magnetic sleeves used, the magnetic air gap lengths are 5 mm and 5.5 mm in the 3.5 kW and the 11 kW machines respectively.

The majority of the losses in the conductive sleeves occur on the outer diameter of the sleeve [31]; thus, to further reduce the rotor losses, the actual physical air gap length should be

This article has been accepted for publication in a future issue of this journal, but has not been fully edited. Content may change prior to final publication. Citation information: DOI 10.1109/TIE.2015.2477797, IEEE Transactions on Industrial Electronics

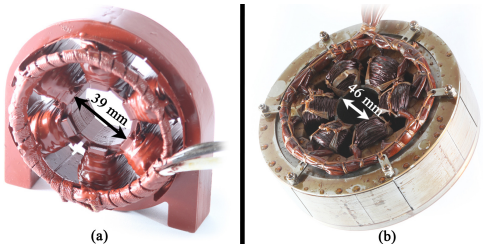

Fig. 6. (a) 3.5 kW High-Speed Permanent Magnet Synchronous Motor stator, (b) 11 kW High-Speed Permanent Magnet Synchronous Generator stator

increased [36]. Following the temperature analysis in Step 7 the stainless steel sleeve thickness in the 11 kW PMSM was consequently reduced. New rotor parameters were transferred to Step 2 for the structural analysis. New design iteration of the active part was done in Step 3 and the new loss values were used in Step 7 for the thermal analysis. Retaining sleeve thickness equal to 2.5 mm was found to be optimum from the mechanical and thermal points of view. This sleeve thickness is the minimum achievable without special machining.

Fig. 6 (a) shows a photo of the 3.5 kW PMSM stator prototype. The machine was made open slot to allow the tooth-coils to be inserted as prefabricated on the teeth. However, analysis of a similar HS machine with 6 slots and 2 poles has shown that the eddy-current distribution gets smaller with increasing tooth tip width [37]. In the 11 kW machine the teeth were made semi-closed. The winding work is more complicated and the copper space factor is lower with a semi-closed slot, and a segmented stator structure was therefore implemented.

The segmented stator structure makes it possible to capitalize on the TC windings. Because of the TC windings selection both machines under consideration have electrically and magnetically isolated phase windings and their fault tolerance is higher [38], [39]. For the 11 kW machine, the prefabricated segmented stator subassemblies enable low-cost high-volume manufacturing, despite the semi-closed slots.

Fig. 6 (b) shows a photo of the 11 kW HS PMSM stator prototype. Geometry optimization was done taking into consideration the selection of lamination with higher per unit losses and greater thickness. The stator yoke was made exceptionally thick to reduce flux density and, hence, decrease iron losses. The optimization procedure is described in detail in [19].

IV. Loss Analysis

The losses are calculated in Step 3 of the design flow. The loss distribution is of great importance in a HS PMSM. Due to the limited volume, the total losses and their particular components have to be calculated accurately to enable accurate cooling system design (Step 7) and ensure reliable machine operation.

The mechanical losses can be estimated from bearing friction torque with an empirical approach proposed by Palmgren [40]. The total friction torque consists of the viscous friction torque and the load-dependent friction torque. Depending on the application, axial load and rubbing seals might also require examination. The total friction can be estimated by summing the different torque components as:

$$T_{\text{friction}} = T_1 + T_2, \tag{4}$$

where T_1 is the viscous friction torque, and T_2 is the load dependent friction torque. Viscous friction torque can be calculated as:

$$T_1 = 10^{-7}\ f_0(\nu\ n)^{2/3}\ d_{\text{M}}^3, \tag{5}$$

where f_0 is an index for the bearing and lubrication type. For deep-groove ball bearings, the range is 0.7 (light series) to 2.0 (heavy series) when grease lubrication is used. Values can be found from literature, for example, Brändlein *et al.* [41]. ν is the operating viscosity (cSt), n is the bearing speed (rpm), and d_{M} is the mean diameter of the bearing inner- and outer diameter or the so-called pitch circle (mm). The load dependent friction torque can be calculated as:

$$T_2 = f_1 F_{\text{mean}}\ d_{\text{M}}^3, \tag{6}$$

where f_1 is a factor for the load. For a radial bearing with a cage the values range from 0.0002 (light series) to 0.0004 (heavy series) [41]. F_{mean} is the mean load acting on the bearings.

The power can then be calculated:

$$P_{\rho,\text{bearing}} = T_{\text{friction}}\Omega. \tag{7}$$

AST 7005 AC bearings were used in the experimental setup of the 11 kW machine. The power losses associated with the resisting drag torque of the rotating cylinder are:

$$P_{\rho,\text{w1}} = \frac{1}{32} k C_{\text{M}} \pi \rho \Omega^3 D_{\text{r}}^4 l_{\text{r}}, \tag{8}$$

where k is a roughness coefficient (for a smooth surface $k = 1$, usually $k = 1 - 1.4$), C_{M} the torque coefficient, ρ the density of the coolant, D_{r} the rotor diameter, and l_{r} the rotor length. The torque coefficient C_{M} depends on the Couette Reynolds number, Re_δ. Implementation of magnetic wedges makes the air gap homogeneous and reduces the roughness coefficient.

The end surface power losses are:

$$P_{\rho,\text{w2}} = \frac{1}{64} C_{\text{M}} \rho \Omega^3 (D_{\text{r}}^5 - D_{\text{ri}}^5), \tag{9}$$

where D_{ri} is the shaft outer diameter and the torque coefficient C_{M} depends now on the tip Reynolds number Re_{r} [13].

The total calculated mechanical losses, P_{mech}, consist of the windage and bearing losses and are the sum of Equations (7 – 9).

The iron, copper and rotor eddy-current losses were calculated using FEM in Step 3. The calculated loss distributions of both machines under consideration at the rated operational point are shown in Table IV.

This article has been accepted for publication in a future issue of this journal, but has not been fully edited. Content may change prior to final publication. Citation information: DOI 10.1109/TIE.2015.2477797, IEEE Transactions on Industrial Electronics

TABLE IV. LOSS DISTRIBUTION OF THE 3.5 KW AND THE 11 KW MACHINES

Losses Type	3.5 kW PMSM	11 kW PMSM
Copper losses, W	104	88
Stator Iron losses, W	121	100
Rotor Sleeve losses, W	25	34
Rotor Magnet losses, W	4	11
Additional losses, W	17	22
Mechanical losses, W	125	456
Total losses, W	396	711

In the 11 kW PMSM, the mechanical losses are the major component of the total losses. Even with copper loss increase due to the lower winding factor or iron and rotor losses increase due to the higher harmonic content of TC windings the mechanical losses are dominant. With the 3.5 kW PMSM the copper, iron, and mechanical loss shares are balanced. The reduction of the mechanical losses was possible due to implementation of AMBs.

The result of the loss calculations for the 11 kW PMSM at different speeds and loads is shown in the efficiency map in Fig. 7.

V. MEASUREMENTS

Test planning and execution during the commissioning (Step 9) vary depending on the customer's requirements, the machine's operating environment and the manufacturer's facilities.

Back-EMF measurements of the 3.5 kW PMSM showed very good agreement with FEM simulations. The difference between the simulated value 209.9 V and the measured value 211.7 V is below 1 %.

Efficiency measurements of this machine were limited by the converter performance and coupling problems between the AMB supported test machine and the eddy current brake. For the aforementioned reasons, the maximum operational speed during the tests was only 25 000 rpm. The measurement results are shown in Fig. 8. The calculated rated point efficiency at 45 000 rpm was 88 % whereas the measured efficiency at 25 000 rpm was 83 %.

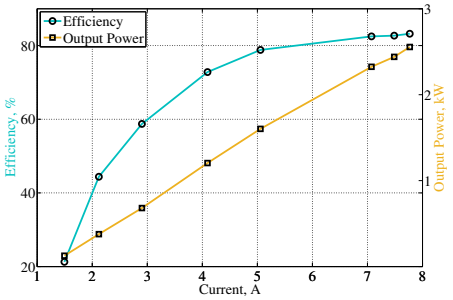

Fig. 8. Measured efficiency and output power of the 3.5 kW PMSM as a function of the phase current at 25 000 rpm

A special measurement installation was manufactured to test the developed 11 kW PMSM separately from the final product system. The installation comprised the electrical machine in a protective case with a forced air cooling system, an eddy-current brake with water cooling, and a joint coupling between them. The designed 11 kW PMSM worked in the motor mode and the input power from the frequency converter was measured with a Yokogawa PZ-4000 power analyzer. The output power was calculated by multiplication of the torque and speed measured by the eddy-current brake. More detailed information about the test setup can be found in [42]. No-load and load tests were conducted to verify the design methodology and loss calculations.

Fig. 9 shows the measured efficiency map of the 11 kW PMSM. A comparison with the calculated efficiency map, illustrated in Fig. 7, shows that in the low speed region the

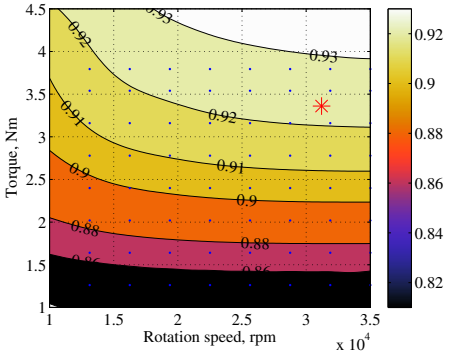

Fig. 7. Calculated efficiency map of the 11 kW High-Speed Permanent Magnet Synchronous Machine. Rated point is marked with an asterisk.

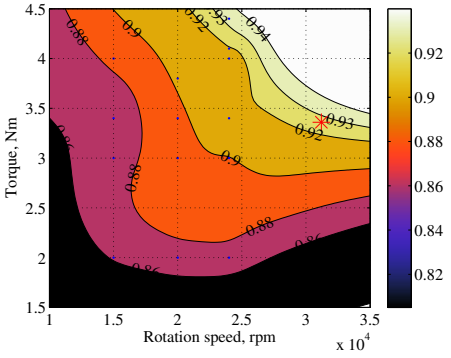

Fig. 9. Measured efficiency map of the 11 kW High-Speed Permanent Magnet Synchronous Machine. Rated operating point is marked with an asterisk.

actual losses are higher than the calculated ones. This may be partly explained by extra losses in the joint coupling, which were not included in calculation of the losses. This hypothesis is supported by the significant difference in the calculated and measured losses at no-load.

At high-speed, however, there is good agreement between the calculated and measured results. For instance, at the rated point $n = 31\ 200$ rpm and $T = 3.36$ Nm, the efficiency difference is below 1 %. This result indicates that the loss calculations discussed in Section IV are fairly reliable. Good agreement of the measured and calculated results indicates the high accuracy of the proposed design methodology for the studied HS PMSMs.

The overall efficiency of the designed machine at the rated point is about 92 %. The electrical efficiency of the machine is above 97 %, since the mechanical losses form about two thirds of the total machine losses. The selected machine topology is very well suitable for HS operation due to the rather high efficiency, robust mechanical design and reduced manufacturing costs.

VI. Conclusion

This paper presented a design methodology for high-speed permanent magnet synchronous machines. By following the proposed design flow, the design process becomes systematic and straightforward. The outcome leads to shorter design time due to a reduction in the number of iterations and mistakes. Additionally, unnecessary parallel working is avoided. The proposed design methodology divides the tasks between different engineering disciplines clearly. Every step of the design flow is described. Critical design issues regarding electromagnetics, mechanical stresses, rotordynamics, thermal analyze, manufacturing and assembly are highlighted.

The design methodology is applied to two HS PMSMs having the same electric machine topology. The designed machines have different loss minimization approaches. The influence of utilization of TC windings in a 2-pole machine on rotordynamics is demonstrated by showing the reduced winding space effect on the critical speeds.

The 11 kW machine measurements results are in good agreement with the results calculated using the presented design methodology, which verifies that the methodology is suitable for HS PMSM design and fairly accurate. The high measured electrical efficiency of the 6-slot 2-pole HS PMSM with TC windings confirms that this topology selection for a HS operation is well reasoned.

In future work, this design methodology can be refined so that it can be adapted to other HS electrical machine topologies, while following the same process at the conceptual level.

References

[1] A. Tenconi, S. Vaschetto, and A. Vigliani, "Electrical machines for high-speed applications: Design considerations and tradeoffs," *IEEE Trans. Ind. Electron.*, vol. 61, no. 6, pp. 3022–3029, June 2014.

[2] R. R. Moghaddam, "High speed operation of electrical machines, a review on technology, benefits and challenges," in *Proc. IEEE ECCE*, 2014, pp. 5539–5546.

[3] D. Gerada, A. Mebarki, N. Brown, C. Gerada, A. Cavagnino, and A. Boglietti, "High-speed electrical machines: Technologies, trends, and developments," *IEEE Trans. Ind. Electron.*, vol. 61, no. 6, pp. 2946–2959, June 2014.

[4] J. Pyrhönen, J. Nerg, P. Kurronen, and U. Lauber, "High-speed high-output solid-rotor induction-motor technology for gas compression," *IEEE Trans. Ind. Electron.*, vol. 57, no. 1, pp. 272–280, Jan 2010.

[5] S. Li, Y. Li, W. Choi, and B. Sarlioglu, "High speed electric machines - challenges and design considerations," in *Proc. XXIst ICEM*, Sept 2014, pp. 2549–2555.

[6] A. Arkkio, T. Jokinen, and E. Lantto, "Induction and permanent-magnet synchronous machines for high-speed applications," in *Proc. IEEE ICEMS*, vol. 2, 2005, pp. 871–876.

[7] Z. Kolondzovski, A. Arkkio, J. Larjola, and P. Sallinen, "Power limits of high-speed permanent-magnet electrical machines for compressor applications," *IEEE Trans. Energy Convers.*, vol. 26, no. 1, pp. 73–82, March 2011.

[8] C. J. G. Ranft, "Mechanical design and manufacturing of a high speed induction machine rotor," Ph.D. dissertation, North-West University, 2010.

[9] F. Cheng, H. Xu, and S. Xue, "Study on the design method of high speed permanent magnet synchronous machine," in *Proc. IEEE ICEMS*, 2011, pp. 1–6.

[10] N. Bernard, F. Martin, and M. El-Hadi Zaim, "Design methodology of a permanent magnet synchronous machine for a screwdriver application," *IEEE Trans. Energy Convers.*, vol. 27, no. 3, pp. 624–633, 2012.

[11] T. Noguchi, Y. Takata, Y. Yamashita, Y. Komatsu, and S. Ibaraki, "220,000-r/min 2-kW PM motor drive for turbocharger," *IEEJ Trans. Appl. Ind.*, vol. 125, no. 9, pp. 854–861, Sept 2005.

[12] J. Dong, Y. Huang, L. Jin, B. Guo, H. Lin, J. Dong, M. Cheng, and H. Yang, "Electromagnetic and thermal analysis of open-circuit air cooled high-speed permanent magnet machines with gramme ring windings," *IEEE Trans. Magn.*, vol. 50, no. 11, pp. 1–4, Nov 2014.

[13] J. Pyrhönen, T. Jokinen, and V. Hrabovcova, *Design of Rotating Electrical Machines*. Chichester, UK: John Wiley & Sons, 2008.

[14] A. Borisavljevic, *Limits, modeling and design of high-speed permanent magnet machines*. Berlin, Germany: Springer, 2012.

[15] B. Riemer, M. Lessmann, and K. Hameyer, "Rotor design of a high-speed permanent magnet synchronous machine rating 100,000 rpm at 10kw," in *Proc. IEEE ECCE*, Sept 2010, pp. 3978–3985.

[16] J. Pyrhönen, V. Ruuskanen, J. Nerg, J. Puranen, and H. Jussila, "Permanent-magnet length effects in AC machines," *IEEE Trans. Magn.*, vol. 46, no. 10, pp. 3783–3789, Oct 2010.

[17] Y. Duan and D. Ionel, "A review of recent developments in electrical machine design optimization methods with a permanent-magnet synchronous motor benchmark study," *IEEE Trans. Ind. Appl.*, vol. 49, no. 3, pp. 1268–1275, May 2013.

[18] S. Y. Yoon, Z. Lin, and P. E. Allaire, *Control of Surge in Centrifugal Compressors by Active Magnetic Bearings: Theory and Implementation*, 1st ed. London: Springer-Verlag, 2013.

[19] N. Uzhegov, J. Pyrhönen, and S. Shirinskii, "Loss minimization in high-speed permanent magnet synchronous machines with tooth-coil windings," in *Proc. IEEE IECON*, Nov 2013, pp. 2960–2965.

[20] E. Kurvinen, J. Sopanen, and A. Mikkola, "Ball bearing model performance on various sized rotors with and without centrifugal and gyroscopic forces," *Mech. Mach. Theory*, vol. 90, pp. 240–260, August 2015.

[21] E. Logan Jr, *Handbook of Turbomachinery*, 2nd ed. New York, USA: Marcel Dekker, 2003.

[22] S. Silber, J. Sloupensky, P. Dirnberger, M. Moravec, W. Amrhein, and M. Reisinger, "High-speed drive for textile rotor spinning applications," *IEEE Trans. Ind. Electron.*, vol. 61, no. 6, pp. 2990–2997, June 2014.

[23] T. Baumgartner, R. Burkart, and J. Kolar, "Analysis and design of a 300-W 500 000-r/min slotless self-bearing permanent-magnet motor," *IEEE Trans. Ind. Electron.*, vol. 61, no. 8, pp. 4326–4336, Aug 2014.

[24] J. Nicholas and L. Barrett, "The effect of bearing support flexibility on critical speed prediction," *Tribol. Trans.*, vol. 29, no. 3, pp. 329–338, 1986.

[25] W. Jiang and T. Jahns, "Coupled electromagnetic-thermal analysis of electric machines including transient operation based on finite-element

This article has been accepted for publication in a future issue of this journal, but has not been fully edited. Content may change prior to final publication. Citation information: DOI 10.1109/TIE.2015.2477797, IEEE Transactions on Industrial Electronics

techniques," *IEEE Trans. Ind. Appl.*, vol. 51, no. 2, pp. 1880–1889, March 2015.
[26] A. Boglietti, A. Cavagnino, D. Staton, M. Shanel, M. Mueller, and C. Mejuto, "Evolution and modern approaches for thermal analysis of electrical machines," *IEEE Trans. Ind. Electron.*, vol. 56, no. 3, pp. 871–882, March 2009.
[27] J. Nerg, M. Rilla, and J. Pyrhönen, "Thermal analysis of radial-flux electrical machines with a high power density," *IEEE Trans. Ind. Electron.*, vol. 55, no. 10, pp. 3543–3554, Oct 2008.
[28] J. Nerg and V. Ruuskanen, "Lumped-parameter-based thermal analysis of a doubly radial forced-air-cooled direct-driven permanent magnet wind generator," *Math. Comput. in Simul.*, vol. 90, pp. 218–229, 2013.
[29] G. Boothroyd, W. Knight, and P. Dewhurst, *Product Design for Manufacture & Assembly Revised & Expanded*. New York, USA: Taylor & Francis e-Library, 2009.
[30] A. Borisavljevic, H. Polinder, and J. Ferreira, "On the speed limits of permanent-magnet machines," *IEEE Trans. Ind. Electron.*, vol. 57, no. 1, pp. 220–227, Jan 2010.
[31] W. Li, H. Qiu, X. Zhang, J. Cao, and R. Yi, "Analyses on electromagnetic and temperature fields of superhigh-speed permanent-magnet generator with different sleeve materials," *IEEE Trans. Ind. Electron.*, vol. 61, no. 6, pp. 3056–3063, June 2014.
[32] W. Li, H. Qiu, X. Zhang, J. Cao, S. Zhang, and R. Yi, "Influence of rotor-sleeve electromagnetic characteristics on high-speed permanent-magnet generator," *IEEE Trans. Ind. Electron.*, vol. 61, no. 6, pp. 3030–3037, June 2014.
[33] N. Uzhegov, E. Kurvinen, and J. Pyrhönen, "Design limitations of 6-slot 2-pole high-speed permanent magnet synchronous machines with tooth-coil windings," in *Proc. IEEE ECCE*, 2014, pp. 1–7.
[34] N. Bianchi, S. Bolognani, and F. Luise, "High speed drive using a slotless PM motor," *IEEE Trans. Power Electron.*, vol. 21, no. 4, pp. 1083–1090, July 2006.
[35] P.-D. Pfister and Y. Perriard, "Very-high-speed slotless permanent-magnet motors: Analytical modeling, optimization, design, and torque measurement methods," *IEEE Trans. Ind. Electron.*, vol. 57, no. 1, pp. 296–303, Jan 2010.
[36] N. Bianchi, D. Durello, and A. Fasolo, "Relationship between rotor losses and size of permanent magnet machines," in *Proc. IEEE SDEMPED*, Sept 2011, pp. 251–257.
[37] K. Shigematsu, J. Oyama, T. Higuchi, T. Abe, and Y. Ueno, "The study of eddy current in rotor and circuit coupling analysis for small size and ultra-high speed motor," in *Proc. IEEE IPEMC*, vol. 1, 2004, pp. 275–279.
[38] F. Magnussen and H. Lendenmann, "Parasitic effects in PM machines with concentrated windings," *IEEE Trans. Ind. Appl.*, vol. 43, no. 5, pp. 1223–1232, Sept 2007.
[39] J. Ede, K. Atallah, G. Jewell, J. Wang, and D. Howe, "Effect of axial segmentation of permanent magnets on rotor loss in modular permanent-magnet brushless machines," *IEEE Trans. Ind. Appl.*, vol. 43, no. 5, pp. 1207–1213, Sept 2007.
[40] A. Palmgren, *Ball and roller bearing engineering*. Philadelphia, USA: SKF Industries Inc., 1959.
[41] J. Brändlein, P. Eschmann, L. Hasbargen, and K. Weigand, *Ball and Roller Bearings: Theory, design, and application*. Chichester, UK: Wiley, 1999.
[42] N. Uzhegov, J. Nerg, and J. Pyrhonen, "Design of 6-slot 2-pole high-speed permanent magnet synchronous machines with tooth-coil windings," in *Proc. XXIst ICEM*, Sept 2014, pp. 2537–2542.

Nikita Uzhegov (M'15) received the B.Sc. degree from Moscow Power Engineering Institute (MPEI), Moscow, Russia, in 2010 and the M.Sc. degree in electrical engineering from Lappeenranta University of Technology (LUT), Lappeenranta, Finland, in 2012.

He is currently a Doctoral Student in the Department of Electrical Engineering, LUT. His research mainly concerns electrical machines and drives, particularly high-speed machines.

Emil Kurvinen M.Sc. (Tech.), was born at Ristiina in Finland on 15th September 1988. He received the B.Sc. and M.Sc. degrees in Department of Mechanical Engineering, from Lappeenranta University of Technology (LUT) in 2011 and 2012, respectively.

He is currently a Doctoral Student at the same university. His current research interest includes rotordynamics and magnetic bearings in high-speed electric machines.

Janne Nerg (SM'12) received the M. Sc. Degree in electrical engineering, the Licentiate of Science (Technology) degree, and the D. Sc. (Technology) degree from Lappeenranta University of Technology (LUT), Lappeenranta, Finland, in 1996, 1998, and 2000, respectively.

He is currently an Associate Professor in the Department of Electrical Engineering at LUT. His research interests are in the field of electrical machines and drives, especially electromagnetic and thermal modeling and design of electromagnetic devices.

Juha Pyrhönen (M'06) born in 1957 in Kuusankoski, Finland, received the Doctor of Science (D.Sc.) degree from Lappeenranta University of Technology (LUT), Finland in 1991. He became an Associate Professor of Electrical Engineering at LUT in 1993 and a Professor of Electrical Machines and Drives in 1997.

He is engaged in research and development of electric motors and power-electronic-controlled drives. Prof. Pyrhönen has wide experience in the research and development of special electric drives for distributed power production, traction drives and high-speed applications. Permanent magnet materials and applying them in machines have an important role in his research. Currently he is also researching new carbon-based materials for electrical machines.

Jussi T. Sopanen (M'14) born in 1974 Enonkoski, Finland, received his M. Sc. Degree in mechanical engineering and D. Sc. (Technology) degree from Lappeenranta University of Technology (LUT), Lappeenranta, Finland, in 1999 and 2004, respectively. He has been a researcher in the Department of Mechanical Engineering at LUT in 1999-2006. He has also worked as a product development engineer in electric machine manufacturer Rotatek Finland Ltd. in 2004-2005. During 2006-12 he worked as Principal Lecturer in Mechanical Engineering and Research Manager in the Faculty of Technology in Saimaa University of Applied Sciences, Lappeenranta, Finland.

He is currently serving as a Professor in Machined Dynamics at LUT. His research interests are rotor dynamics, multi-body dynamics and mechanical design of electrical machines.

Sergey Shirinskii (M'12) received the Ph.D. degree from Moscow Power Engineering Institute, Moscow, Russia, in 1993. His Ph.D. thesis was devoted to simulation of motor generator of an autonomous flywheel power storage. After graduation, he worked at Moscow Power Engineering Institute.

He is currently an Associate Professor at the Department of Electromechanics. His research fields are numerical analysis of magnetic fields and development of tooth contour method for simulation of electric machines.

Publication IV

Uzhegov N., Kurvinen E. and Pyrhönen J.
Design limitations of 6-slot 2-pole high-speed permanent Magnet Synchronous machines with Tooth- Coil windings

Reprinted with permission from
EPE'14 ECCE Europe,
European Conference on Power Electronics and Applications.
Lappeenranta, Finland, 26.-28.09.2014,

Design Limitations of 6-slot 2-pole High-Speed Permanent Magnet Synchronous Machines with Tooth-Coil Windings

Nikita Uzhegov, Emil Kurvinen and Juha Pyrhönen
LAPPEENRANTA UNIVERSITY OF TECHNOLOGY
P.O. Box 20, FI-53851
Lappeenranta, Finland
Phone: +358 46 526-1394
Nikita.Uzhegov@lut.fi
URL: http://www.lut.fi

Keywords

<<AC machine>>, <<Permanent magnet motor>>, <<High-speed drive>>, <<Fault tolerance>>, <<Harmonics>>.

Abstract

Mechanical and electro-magnetic limitations of high-speed tooth-coil electrical machines having 6 slots and 2 poles are investigated. The paper analyses the performance of a designed high-speed Permanent Magnet Synchronous Generator with Tooth-Coil windings (TC-PMSM) with the topology mentioned. The generator nominal power is designed for 11 kW and nominal rotation speed is set to 31 200 rpm.

Introduction

High-speed electrical machines are today a mature and proven technology area. The development of such machines is constantly growing because of the need for the high-speed solution in turbochargers, mechanical turbo-compounding systems, aero engine spools, helicopter engines, racing engines and fuel pumps [1]. The reason for that is a number of advantages, for instance, high power and torque density, simplification of the system by removing a gearbox. Thereby, direct drives reduce weight, costs and improve a reliability of the system [2].

Tooth-coil (TC) windings are becoming popular in different applications. First of all, both single and double layer tooth-coil windings are cheap to manufacture and are therefore an interesting alternative also for low-power high-speed machines if the problems related to the high amount of harmonic current linkages can be solved. One of the main advantages of using TC windings in high-speed applications is the short end windings. Especially, in case of two-pole machines the traditional windings have extremely large end windings that force the rotor long and therefore easily supercritical. Using TC winding instead helps keeping the rotors short which results in higher critical speeds.

In this case the simplest possible permanent magnet (PM) rotor is used as a starting point. A diametrally magnetized cylindrical magnet forms the rotor excitation and a tubular housing around the permanent magnet creates the mechanical strength of the shaft. Such a design has its dimensional and thereby power limits that will be studied in this paper.

Losses of the electrical machine define the cooling needs and contribute the machine design limits. Since single layer TC windings create a higher amount of harmonics multilayer TC windings should be favored in higher speed applications. A comparison of different TC winding types is given in [3]. The air-gap length also has a significant impact on the harmonic content penetrating into the rotor surface. In a high-speed PMSM the air gap length should, therefore, be selected higher than in low speed machines as it is shown in [4]. Higher air gap length leads to greater cooling flow area and that decreases the temperatures in the electric machine active parts.

TC windings also provide the opportunity to pass the coolant directly through the slots between the windings and effectively cool them down. A photo of a stator prototype, using TC windings, is shown in Fig. 1.

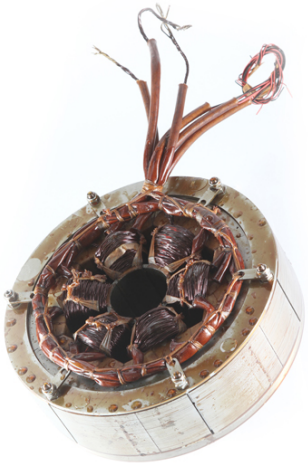

Figure 1: Six-slot two-pole prototype for a small high-speed PMSM

The electromagnetic design parameters define most of the design requirements. However, simultaneously the mechanical properties such as rotor dynamics, mechanical rigidness and manufacturability should be considered to produce a working generator. Selection of the mechanical structure has major impact for the final product lifetime, quality and price. In the following chapter permanent magnet rotor topologies are introduced and the most important mechanical phenomena are studied for the selected topology. The generator main parameters are represented in Table I.

Table I: Generator parameters

Rated speed n_{n}, min^{-1}	31 200
Rated power P_{n}, kW	11
Number of poles, p	2
Number of stator slots, Q_{s}	6
Rated torque, T_{n}, Nm	3.36
Synchronous inductance, L_{s}, pu	0.44
Rotor outer radius, R_{o}, m	0.023

The application where the developed high-speed PM generator is implemented is a micro-Organic Rankine Cycle (ORC) power plant. The target is to design an easily manufacturable and cheap construction for the active parts of the generator. Due to the manufacturability and the preferable TC winding segmented stator structure is selected.

Mechanical topologies and limitations

Several rotor topologies for permanent magnet machines are introduced. The different rotor topologies for PMSMs are shown in Fig. 2. Depending on the machine parameters correct topology should be selected. The rotor topology affects the mechanical rigidness of the machine and it should be selected not only from the machine performance point of view but should also take the mechanical limitations into account. The internal permanent magnet (IPM) rotor (Fig. 2a) has to be optimized carefully in case of the high-speed machines. The construction has to provide structural integrity and at the same time has to be thin enough and not shunt the magnet flux [5]. Nevertheless, a 2-pole electrical machine is difficult to implement with interior permanent magnet with a working design. The surface permanent magnet (SPM) construction (Fig. 2b) is a good option from the electromagnetic point of view, but it needs to have a retaining sleeve to tolerate high-speeds. The full cylinder magnet inside a retaining sleeve is the most convenient option from the mechanical rigidness point of view, however it could produce more

losses [6]. The stator of the designed high-speed Permanent Magnet Synchronous Generator (HSPMSG) is shown in Fig. 1 and the rotor of this machine has a topology illustrated in Fig. 2c.

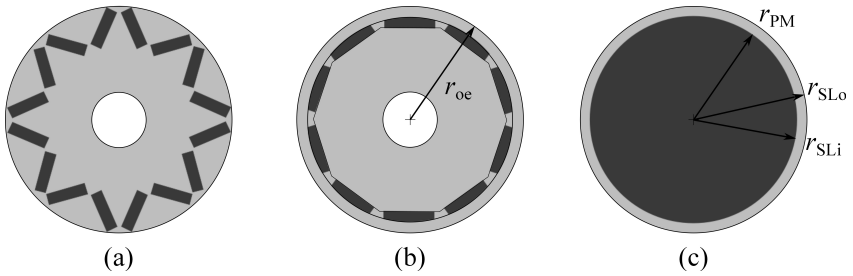

Figure 2: Permanent magnet rotor topologies. a) Multiple-pole internal permanent magnet; b) Two or multiple pole surface permanent magnet with retaining sleeve; c) Two-pole full cylindrical magnet with retaining sleeve

The high-speed machines require more complex computations compared to the low-speed machines due to the material limitations and dynamical behaviour. Mechanical limitations can be divided into three main categories. First is the maximum diameter that the rotor can have to withstand the high rotation speed and the centrifugal force caused by that. Second is the fitting to maintain the contact between the permanent magnet and sleeve during all conditions. Third is the rotor dynamics. The rotor dynamical performance varies as a function of rotation speed and due to that the rotor dynamics have a major effect to the rotor performance and durability.

The coating materials could be divided into conducting and non-conducting ones. The trade-off between these materials is explained in a way that a conducting material causes losses in the rotor, but usually can tolerate more mechanical loads. In high-speed machines with full cylindrical magnet it is necessary to use metallic sleeves, which are, therefore, conducting, to transfer the torque and to maintain rigidity [7].

The preliminary dimensions for the maximum shaft radius can be calculated as

$$r_{oe} = \sqrt{\frac{\sigma_{mec}}{C' \rho \Omega^2}}, \tag{1}$$

where σ_{mec} is the material yield strength, $C' = \frac{3+\nu}{8}$ - for the full cylindrical with retaining sleeve, ν is the Poisson's ratio, ρ is the material density, and Ω is the angular velocity of the rotor. Therefore, the maximum radius of the rotor at the desired speed is restricted by the allowed mechanical stress [4]. It should be noted that equation (1) only considers the centrifugal force and does not take into account any additional stresses such as thermal stresses due to differences in material thermal expansion coefficients, stresses due interference fit between magnet and the sleeve, stresses caused by dynamical conditions such as operating at critical speed. These additional stresses increase the total stress affecting the structure. However, the yield strength should not be exceeded in any condition. Due to that the yield strength value used in equation (1) should include the safety factor and due to that it should be below the actual yield strength. However, this gives an idea of the rotor size.

When the estimated value for the rotor radius is calculated then it is possible to calculate the length of the active part of the rotor for the particular machine to fulfill the required power and torque values. The optimization technique for the rotor volume, which also shows the high dependence on the thermal modeling is described in [8].

The next factor, that could cause the failure of PM and the rotor itself, is the elastic limitation. Magnet and sleeve should be in a contact during all possible operation conditions. In the case of SmCo magnet material and stainless steel the rotation and operation temperature cause magnet and sleeve to expand. The total expansion of the magnet and the sleeve, (u_{PM} and u_{SL}), can be calculated by considering the expansion due to the rotation speed, ($u_{PM\Omega}$ and $u_{SL\Omega}$), as well as the expansion of due to the thermal expansion, (u_{PMtemp} and u_{SLtemp}). The total expansion can be calculated as

$$\begin{aligned} u_{PM}(r) &= u_{PM\Omega} + u_{PMtemp} \\ &= \tfrac{3+\nu_{PM}}{8} \rho_{PM} \Omega^2 \tfrac{1-\nu_{PM}}{E_{PM}} r \left[{r_{PM}}^2 - \tfrac{1+\nu_{PM}}{3+\nu_{PM}} r^2 \right] + \alpha_{PM} r \Delta t \ , \\ u_{SL}(r) &= u_{SL\Omega} + u_{SLtemp} \\ &= \tfrac{3+\nu_{SL}}{8} \rho_{SL} \Omega^2 \tfrac{1-\nu_{SL}}{E_{SL}} r \left[r_{SLi}^2 + r_{SLo}^2 - \tfrac{1+\nu_{SL}}{3+\nu_{SL}} r^2 + \tfrac{1+\nu_{SL}}{1-\nu_{SL}} \tfrac{r_{SLi}^2 r_{SLo}^2}{r^2} \right] + \alpha_{SL} r \Delta t \ , \end{aligned} \tag{2}$$

where r is the radius from the center where the expansion is calculated, subscripts PM and SL refers to magnet and sleeve, ν is the Poisson's ratio of given material, ρ is the material density, Ω is the rotation speed, E is the modulus of elasticity, r_{PM} is the magnet radius, r_{SLi} is the sleeve inner radius and r_{SLo} is the sleeve outer radius, α is the thermal expansion coefficient and Δt is the temperature difference from the room temperature.

Magnet and sleeve should be fixed in a away that the produced torque is transmitted to the rotor shaft. Usually this is done by manufacturing the sleeve smaller than the magnet outer diameter and with the difference in the temperatures enables to install the sleeve over the magnet. This is called shrink fit or interference fit. The interference fit between the magnet and sleeve should be selected so that the yield strength of the magnet or the sleeve are not exceeded and the maximum temperature of the permanent magnet is not exceeded. The dynamical interference fit, λ, can be calculated by considering the total expansion calculated with equation (2) and reduce that amount from the designed static interference fit, u_{sinterf}, amount as $\lambda = u_{\mathrm{PM}} + u_{\mathrm{SL}} - u_{\mathrm{sinterf}}$. The dynamic contact pressure between the magnet and the sleeve can be calculated as

$$p_{\mathrm{c}} = \frac{\lambda r_{\mathrm{PM}} E_{\mathrm{PM}} E_{\mathrm{SL}} (r_{\mathrm{PM}}^2 - r_{\mathrm{SLo}}^2)}{\begin{array}{l}\left((r_{\mathrm{PM}}^4 - r_{\mathrm{PM}}^2 r_{\mathrm{SLo}}^2)\,\nu_{\mathrm{SL}} - r_{\mathrm{PM}}^4 - r_{\mathrm{PM}}^2 r_{\mathrm{SLo}}^2\right) E_{\mathrm{PM}} + \\ \left((-r_{\mathrm{PM}}^4 + r_{\mathrm{PM}}^2 r_{\mathrm{SLo}}^2)\,\nu_{\mathrm{PM}} + r_{\mathrm{PM}}^4 - r_{\mathrm{PM}}^2 r_{\mathrm{SLo}}^2\right) E_{\mathrm{SL}}\end{array}} \tag{3}$$

The stresses due to the rotation speed, thermal effect and pressure from the interference fit are highest in the contact point between magnet and sleeve. Tangential and radial stresses can be calculated as a function of r due to the contact pressure, rotation of the magnet and sleeve as

$$\begin{aligned}
\sigma_{\mathrm{rc}} &= \tfrac{r_{\mathrm{SLi}}^2 p_{\mathrm{c}} - r_{\mathrm{SLo}}^2 p_{\mathrm{o}}}{r_{\mathrm{SLo}}^2 - r_{\mathrm{SLi}}^2} - \tfrac{r_{\mathrm{SLi}}^2 r_{\mathrm{SLo}}^2 (p_{\mathrm{s}} - p_{\mathrm{o}})}{r^2 (r_{\mathrm{SLo}}^2 - r_{\mathrm{SLi}}^2)} \\
\sigma_{\mathrm{tc}} &= \tfrac{r_{\mathrm{SLi}}^2 p_{\mathrm{c}} - r_{\mathrm{SLo}}^2 p_{\mathrm{o}}}{r_{\mathrm{SLo}}^2 - r_{\mathrm{SLi}}^2} + \tfrac{r_{\mathrm{SLi}}^2 r_{\mathrm{SLo}}^2 (p_{\mathrm{s}} - p_{\mathrm{o}})}{r^2 (r_{\mathrm{SLo}}^2 - r_{\mathrm{SLi}}^2)} \\
\sigma_{\mathrm{rPM\Omega}} &= \tfrac{3+\nu_{\mathrm{PM}}}{8} \rho_{\mathrm{PM}} \Omega^2 [r_{\mathrm{PM}} - r^2] \\
\sigma_{\mathrm{tPM\Omega}} &= \tfrac{3+\nu_{\mathrm{PM}}}{8} \rho_{\mathrm{PM}} \Omega^2 [r_{\mathrm{PM}} - \tfrac{1+3\nu_{\mathrm{PM}}}{3+\nu_{\mathrm{PM}}} r^2] \\
\sigma_{\mathrm{rSL\Omega}} &= \tfrac{3+\nu_{\mathrm{SL}}}{8} \rho_{\mathrm{SL}} \Omega^2 [r_{\mathrm{SLi}}^2 + r_{\mathrm{SLo}}^2 - r^2 - \tfrac{r_{\mathrm{SLi}}^2 r_{\mathrm{SLo}}^2}{r^2}] \\
\sigma_{\mathrm{tSL\Omega}} &= \tfrac{3+\nu_{\mathrm{SL}}}{8} \rho_{\mathrm{SL}} \Omega^2 [r_{\mathrm{SLi}}^2 + r_{\mathrm{SLo}}^2 - \tfrac{1+3\nu_{\mathrm{SL}}}{3+\nu_{\mathrm{SL}}} r^2 + \tfrac{r_{\mathrm{SLi}}^2 r_{\mathrm{SLo}}^2}{r^2}]
\end{aligned} \tag{4}$$

where p_{c} contact pressure and p_{o} pressure in the electric machine (air). With the superposition theorem the radial and tangential stresses in the sleeve can be sum into one $\sigma_{\mathrm{rtot}} = \sigma_{\mathrm{rc}} + \sigma_{\mathrm{rSL\Omega}}$ and $\sigma_{\mathrm{ttot}} = \sigma_{\mathrm{tc}} + \sigma_{\mathrm{tSL\Omega}}$. The VonMises stress can be calculated then as $\sigma_{\mathrm{vmises}} = \sqrt{\sigma_{\mathrm{ttot}}^2 - \sigma_{\mathrm{ttot}}\sigma_{\mathrm{rtot}} + \sigma_{\mathrm{rtot}}^2}$. [9, 10]

Third step of the analysis is the rotor's dynamical behaviour over the operation speed. The rotor dynamics is the criterion of the reliable electrical machine operation. The rotor dynamics do not only limit the performance of the motor itself but also affects the bearings, shaft dimensioning and other environment of the installation. The natural frequencies of the rotor as well as the vibration responses caused by excitation forces, *e.g*, unbalance forces, should be determined. In order to determine the rotor dynamics accurately both analytical solution including the finite element method and experimental verification should be performed. The experimental test can be used to determine, *e.g*, the stiffness of the magnet and sleeve contact. First step is to determine the free-free vibration modes, *i.e*, non-supported modes. Three first free-free modes for the studied structure are shown in Fig. 3. The calculated results of the free-free modes are validated with a laser scanning vibrometer (LSV).

Second step is to determine the critical speeds of the rotor bearing system, *i.e*, supported structure. Stiffness of the support and gyroscopic effect varies as a function of rotation speed which affects the natural frequencies. The critical speeds occur when the natural frequencies coincides with the rotor rotation speed. The critical speeds can be determined by plotting a Campbell diagram where the natural frequencies are shown as a function of the rotation speed. Third step is to calculate steady state response where the force caused by residual unbalance shows the vibration amplitude in the critical speeds. The steady state response is used to determine the severity of the critical speeds to the rotor's dynamical behaviour. [11, 12]

Active Magnetic bearings (AMBs) are gaining popularity in high-speed applications because there is no mechanical contact between the bearings and the rotor, thereby mechanical friction losses are excluded from the system, and thus, it is possible to gain higher rotational speeds. An example of AMBs implementation in a high-speed electrical machine and its advantages are described in [13]. Thereby, the correct implementation of this technology could extend the mechanical limit of the high-speed electrical machines.

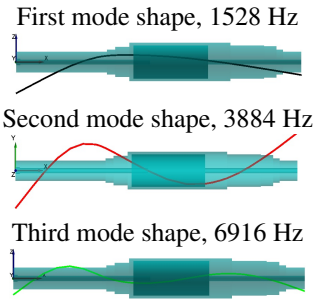

Figure 3: Free-free modes of the studied rotor structure.

Electromagnetic limitations

Losses in the electrical machine apply constraints up to the maximum possible power. The first limit is related to the maximum winding temperature rise and the second is associated to the irreversible demagnetization of the PM [6]. This chapter discusses these two aspects using as an example the design of a HSPMSG for a micro-ORC power plant project.

Copper losses are in a direct ratio to the current density in the windings. Double layer tooth-coil windings allow implementing a segmented structure of the stator. This, in turn, leads to a higher copper space factor and decreases current density. The micro-ORC installation construction together with TC windings also allows to directly remove heat from the windings surface. The micro-ORC working fluid is passing through the slots and cools the windings in an effective way.

The next way to extend the copper loss limit is by using multiphase windings. The increase of the phase number, for instance, up to six, is leading to increasing of the possible maximum machine power by dividing the energy flows in the winding into more channels and decreasing inverter power ratings per phase. This option has also drawbacks, for example, the number of components is increasing which leads to the reliability decrease. The analysis of different multiphase windings for aerospace machine has been studied, for instance, in [14]. However, this limit is a subject of a further investigation.

The rotor losses of the PM machine do not significantly decrease the overall efficiency, however, they could lead to the magnet demagnetization. In the implemented machine construction heat is removed directly from the rotor surface as in case of windings. The SmCo magnet is preferable as it can tolerate higher temperatures, however, its price is higher than NdFeB.

The rotor losses are caused by current linkage harmonics due to both slot opening and discrete current distribution. Since the rotor is moving with constant speed, these harmonics cause eddy-currents in the sleeve and PM [15].

Current linkage harmonics modelled using a finite-element model (FEA) analysis are illustrated in Fig. 4. The total harmonics are obtained by analysing the air gap flux density curve at the rated operating point of the generator. The slot harmonics are received by no-load machine analysis at the rated speed.

The first harmonic is the working harmonic of the three phase 2-pole 6-slot machines and therefore it is used as a base value for per unit representation. Since TC is implemented in HSPMSG the discrete

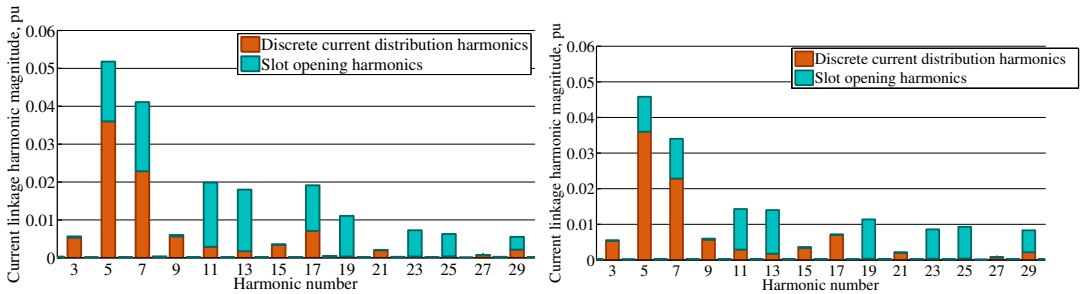

Figure 4: Current linkage harmonics of six-slot two-pole high-speed PMSM. a) Without slot wedges; b) With magnetic slot wedges

Table II: Rotor losses

	Retaining sleeve losses, W	Permanent magnet losses, W	Total rotor losses, W
Without slot wedges	49	12	61
With magnetic slot wedges	34	11	45

current distribution harmonics accounts for a sizable proportion of the total harmonic content. However, only part of these harmonics penetrate the rotor because of the increased air-gap of the electrical machine.

Tooth tips are designed in a way to decrease the harmonics due to slot openings. Nevertheless, further reduction of these harmonics is possible by installation magnetic slot wedge's between the tooth tips. The wedges relative permeability has a great impact on the slot opening harmonic content. Due to the availability limit wedges with a relative permeability equal to 3 were selected.

Fig. 4b shows the analysis of the generator with slot wedges. The total amount of slot opening harmonics is decreased by 25.5% and, for instance, 17^{th} harmonic is eliminated. Due to the air-gap harmonics reduction total rotor losses are decreased, too. Table II shows the amount of losses in the permanent magnet and conducting sleeve before and after the slot wedges installation. The total rotor losses decreased from 61 W to 45 W and therefore the magnet demagnetization risk is decreased.

The final machine configuration involves the reduction of the sleeve to the minimum allowed value, i.e. 2.5 mm, inclusion of magnetic wedges with a relative permeability of 3 between the tooth tips, and an increase in the air-gap by reducing the lamination by up to 3.4 mm.

The number of methods for reducing retaining sleeve losses could be found in [16]. The one way to decrease the magnet losses is to divide the magnet into smaller pieces, therefore, the PM eddy-current losses will reduce.

In case of the SPM with the retaining sleeve the rotor loss shares are similar. For instance, paper [17] describes a technique to estimate rotor magnets and sleeve eddy-current losses in HSPMSM. The final distribution of the rotor losses is 25% in the magnets and 75% is in the sleeve which is close to the results obtained with the 2D FEA for the HSPMSG for a micro-ORC installation.

Conclusion

The implemented machine structure could be used in high-speed applications due to the mechanical rigidness of the rotor and usage of tooth-coil windings. Rotor topology limits the maximum speed of the electrical machine. This limit could be extended by using Active Magnetic Bearings. In case of full cylindrical magnet usage of retaining sleeve leads to the trade offs between rigidness, price and losses. The optimum amount of shrinkage could be found for the existing geometry parameters of the rotor. Double layer TC windings could lead to the copper losses decrease due to the high copper space factor and shorter end windings in comparing with distributed windings. Air-gap length increase cuts the amount of harmonics, which reach the rotor. The installation of the slot wedges between tooth tips leads to the significant reduction of the slot opening harmonic content. Therefore, rotor losses decrease and together with correct selection of the magnet ensure the demagnetization risk absence. A number of ways to extend the design limits of the HSPMSM were proposed. Designing a high-speed electric generator has several requirements and the final solution has several compromises in order to have suitable manufacturing costs. The prototype is build and preliminary runs are made.

References

[1] D. Gerada, A. Mebarki, N. Brown, C. Gerada, A. Cavagnino, and A. Boglietti, "High speed electrical machines;technologies, trends and developments," pp. 1–1, 2013.

[2] A. Tenconi, S. Vaschetto, and A. Vigliani, "Electrical machines for high-speed applications: Design considerations and trade-offs," pp. 1–1, 2013.

[3] L. Alberti and N. Bianchi, "Theory and design of fractional-slot multilayer windings," *Industry Applications, IEEE Transactions on*, vol. 49, no. 2, pp. 841–849, 2013.

[4] J. Pyrhönen, T. Jokinen, and V. Hrabovcova, *Design of Rotating Electrical Machines*. Chichester, UK: John Wiley & Sons, 2008.

[5] A. EL-Refaie, R. Manzke, and T. Jahns, "Application of bi-state magnetic material to automotive offset-coupled ipm starter/alternator machine," *Industry Applications, IEEE Transactions on*, vol. 40, no. 3, pp. 717–725, 2004.

[6] N. Bianchi, S. Bolognani, and F. Luise, "Potentials and limits of high-speed pm motors," *Industry Applications, IEEE Transactions on*, vol. 40, no. 6, pp. 1570–1578, 2004.

[7] Z. Zhu, K. Ng, N. Schofield, and D. Howe, "Improved analytical modelling of rotor eddy current loss in brushless machines equipped with surface-mounted permanent magnets," *Electric Power Applications, IEE Proceedings* -, vol. 151, no. 6, pp. 641–650, 2004.

[8] N. Bernard, F. Martin, and M. El-Hadi Zaim, "Design methodology of a permanent magnet synchronous machine for a screwdriver application," *Energy Conversion, IEEE Transactions on*, vol. 27, no. 3, pp. 624–633, 2012.

[9] A. P. Boresi, R. J. Schmidt, and O. M. Sidebottom, *Advanced mechanics of materials*. Wiley New York, 1993, vol. 5.

[10] A. Borisavljevic, *Limits, modeling and design of high-speed permanent magnet machines*. Springer, 2012.

[11] A. Borisavljevic, H. Polinder, and B. Ferreira, "Overcoming limits of high-speed pm machines," in *Electrical Machines, 2008. ICEM 2008. 18th International Conference on*, 2008, pp. 1–6.

[12] E. H. Maslen and G. Schweitzer, *Magnetic Bearings: Theory, Design, and Application to Rotating Machinery*. Springer, 2009.

[13] A. Smirnov, R. Jastrzebski, K. Hynynen, and O. Pyrhönen, "Comparison of suboptimal control methods in magnetic levitation system," in *Power Electronics and Applications (EPE), 2013 15th European Conference on*, 2013, pp. 1–10.

[14] A. Thomas, Z. Zhu, R. Owen, G. Jewell, and D. Howe, "Multiphase flux-switching permanent-magnet brushless machine for aerospace application," *Industry Applications, IEEE Transactions on*, vol. 45, no. 6, pp. 1971–1981, 2009.

[15] E. Fornasiero, N. Bianchi, and S. Bolognani, "Slot harmonic impact on rotor losses in fractional-slot permanent-magnet machines," *Industrial Electronics, IEEE Transactions on*, vol. 59, no. 6, pp. 2557–2564, 2012.

[16] A. EL-Refaie, "Fractional-slot concentrated-windings synchronous permanent magnet machines: Opportunities and challenges," *Industrial Electronics, IEEE Transactions on*, vol. 57, no. 1, pp. 107–121, 2010.

[17] N. Boubaker, D. Matt, P. Enrici, T. Martire, and F. Nierlich, "Estimation of rotor eddy-current losses for high speed spmsm," in *Power Electronics and Applications (EPE), 2013 15th European Conference on*, 2013, pp. 1–6.

ACTA UNIVERSITATIS LAPPEENRANTAENSIS

650. ROOZBAHANI, HAMID. Novel control, haptic and calibration methods for teleoperated electrohydraulic servo systems. 2015. Diss.

651. SMIRNOVA, LIUDMILA. Electromagnetic and thermal design of a multilevel converter with high power density and reliability. 2015. Diss.

652. TALVITIE, JOONAS. Development of measurement systems in scientific research: Case study. 2015. Diss.

653. ZUBEDA, MUSSA. Variational ensemble kalman filtering in hydrology. 2015. Diss.

654. STEPANOV, ALEXANDER. Feasibility of industrial implementation of laser cutting into paper making machines. 2015. Diss.

655. SOKOLOV, MIKHAIL. Thick section laser beam welding of structural steels: methods for improving welding efficiency. 2015. Diss.

656. GORE, OLGA. Impacts of capacity remunerative mechanisms on cross-border trade. 2015. Diss.

657. AURINKO, HANNU. Risk assessment of modern landfill structures in Finland. 2015. Diss.

658. KAIJANEN, LAURA. Capillary electrophoresis: Applicability and method validation for biorefinery analytics. 2015. Diss.

659. KOLHINEN, JOHANNA. Yliopiston yrittäjämäisyyden sosiaalinen rakentuminen. Case: Aalto-yliopisto. 2015. Diss.

660. ANNALA, SALLA. Households' willingness to engage in demand response in the Finnish retail electricity market: an empirical study. 2015. Diss.

661. RIABCHENKO, EKATERINA. Generative part-based Gabor object detector. 2015. Diss.

662. ALKKIOMÄKI, VILLE. Role of service and data reuse in enterprises. 2015. Diss.

663. VÄNTSI, OLLI. Utilization of recycled mineral wool as filler in wood plastic composites. 2015. Diss.

664. KLEMOLA, KATJA. Tuottavuuden, vaikuttavuuden ja kustannusvaikuttavuuden arviointi alueellisesti integroiduissa sosiaali- ja terveyspalveluissa – palvelujen käyttöön perustuva malli ja esimerkkejä. 2015. Diss.

665. HEROLD, KRISTIINA. Impact of Word-of-Mouth on consumer decision-making: An information processing perspective in the context of a high-involvement service. 2015. Diss.

666. OLABODE, MUYIWA. Weldability of high strength aluminium alloys. 2015. Diss.

667. VANHALA, ERNO. The role of business model in computer game development organizations. 2015. Diss.

668. SALAMPASIS, DIMITRIOS. Trust-embedded open innovation: Towards a human-centric approach in the financial industry. 2015. Diss.

669. DE SMET, DIETER. Innovation ecosystem perspectives on financial services innovation. 2015. Diss.

670. PORRAS, PÄIVI. Utilising student profiles in mathematics course arrangements. 2015. Diss.

671. SALMINEN, JUHO. The role of collective intelligence in crowdsourcing innovations. 2015. Diss.

672. ROSAS, SAILA. Co-operative acquisitions – the contextual factors and challenges for co-operatives when acquiring an investor-owned firm. 2015. Diss.

673. SINKKONEN, TIINA. Item-level life-cycle model for maintenance networks – from cost to additional value. 2015. Diss.

674. TUUNANEN, JUSSI. Modelling of changes in electricity end-use and their impacts on electricity distribution. 2015. Diss.

675. MIELONEN, KATRIINA. The effect of cationic-anionic polyelectrolyte multilayer surface treatment on inkjet ink spreading and print quality. 2015. Diss.

676. OMAJENE, JOSHUA. Underwater remote welding technology for offshore structures. 2015. Diss.

677. NUUTINEN, PASI. Power electronic converters in low-voltage direct current distribution – analysis and implementation. 2015. Diss.

678. RUSATSI, DENIS. Bayesian analysis of SEIR epidemic models. 2015. Diss.

679. STRAND, ELSI. Enhancement of ultrafiltration process by pretreatment in recovery of hemicelluloses from wood extracts. 2016. Diss.

680. TANNINEN, PANU. Press forming of paperboard – advancement of converting tools and process control. 2015. Diss.

681. VALTONEN, PETRI. Distributed energy resources in an electricity retailer's short-term profit optimization. 2015. Diss.

682. FORSSTRÖM-TUOMINEN, HEIDI. Collectiveness within start up-teams – leading the way to initiating and managing collective pursuit of opportunities in organizational contexts. 2015. Diss.

683. MAGUYA, ALMASI. Use of airborne laser scanner data in demanding forest conditions. 2015. Diss.

684. PEIPPO, JUHA. A modified nominal stress method for fatigue assessment of steel plates with thermally cut edges. 2015. Diss.

685. MURASHKO, KIRILL. Thermal modelling of commercial lithium-ion batteries. 2016. Diss.

686. KÄRKKÄINEN, TOMMI. Observations of acoustic emission in power semiconductors. 2016. Diss.